Low Complexity Reconfigurable Physical Layer for the L-Band Digital Aeronautical Communications System

By

Niharika Agrawal

Under the supervision of **Dr. Sumit J. Darak**

Department of Electronics and Communication Engineering

Indraprastha Institute of Information Technology Delhi

New Delhi– 110020

May , 2022

Low Complexity Reconfigurable Physical Layer for the L-Band Digital Aeronautical Communications System

By

Niharika Agrawal

A Thesis

submitted in partial fulfillment of the requirements for the degree of

Doctor of Philosophy

Department of Electronics and Communication Engineering
Indraprastha Institute of Information Technology Delhi
New Delhi– 110020

May , 2022

Certificate

This is to certify that the thesis titled "***Low Complexity Reconfigurable Physical Layer for the L-Band Digital Aeronautical Communications System***" being submitted by ***Niharika Agrawal*** to the Indraprastha Institute of Information Technology Delhi, for the award of the degree of Doctor of Philosophy, is an original research work carried out by her under my supervision. In my opinion, the thesis has reached the standard fulfilling the requirements of the regulations relating to the degree.

The results contained in this thesis have not been submitted in part or full to any other university or institute for the award of any degree or diploma.

May , 2022

Dr. Sumit J. Darak
Assistant Professor,
Dept. of Electronics & Communication Engineering,
Indraprastha Institute of Information Technology Delhi-110020, India.

Declaration

This is certified that the thesis entitled "***Low Complexity Reconfigurable Physical Layer for the L-Band Digital Aeronautical Communications System***" being submitted by me to the Indraprastha Institute of Information Technology Delhi, for the award of degree of **Doctor of Philosophy**, is a bonafide work carried out by me. This research work has been carried out under the supervision of **Dr. Sumit J. Darak**. The study pertaining to this thesis has not been submitted in part or in full, to any other University or Institution for the award of any other degree.

May , 2022

Niharika

Niharika Agrawal
PhD Student,
Dept. of Electronics Communication Engineering,
Indraprastha Institute of Information Technology Delhi-110020, India.

Abstract

Exponential increase in global air traffic and demands to support heterogeneous services ranging from data to multimedia have compelled communication theorists and engineers to explore an alternative to existing very high frequency (VHF) band (118-137 MHz) based air-to-ground communication system. After various studies and experiments, one promising solution of utilizing multiple 1 MHz frequency bands between incumbent distance measuring equipment (DME) signals in L-band (960-1164 MHz) is proposed and it is referred as L-band Digital Aeronautical Communication System (LDACS). An efficient utilization of such narrowband non-contiguous spectrum is challenging and hence, various activities to invent breakthrough technologies that provide higher spectral efficiency are being encouraged. Given the history of more than a century of wireless innovation, redesign of physical layer (PHY) is critical to improve the vacant spectrum utilization.

Success of orthogonal frequency division multiplexing (OFDM) in cellular and WiFi networks makes it the popular choice for LDACS PHY. LDACS also applies a raised cosine slope with a roll-off factor of 0.107 within a window time of 12.8 µs for better spectrum containment and less out-of-band radiation. It is assumed that DME does not use narrow-band filters at their receiver input. With that, DME might be susceptible to interference even if the transmit spectrum of the potential interferer is strongly contained. Therefore, the existing LDACS PHY to utilizes a fixed transmission bandwidth of only 498 kHz kHz over in between the 1 MHz channel grid of DME.

Furthermore, fixed transmission bandwidth limits its usefulness to support heterogeneous services demanding distinct bandwidths and dynamic control over PHY parameters such as OOB emission, transmission bandwidth etc. The overall objective of this thesis is to study and develop spectrum efficient, reconfigurable and low complexity LDACS PHY, analyze its performance in real-radio environment and feasibility on system-on-chip (SoC). This thesis mainly

focuses on the FL transmission of the LDACS.

The first contribution of this thesis is to design the PHY frame structure for the LDACS comprising of data, null and reference signals to support tunable bandwidth. The proposed frame structure maintains the complete compatibility with existing LDACS and offers transmission bandwidth from 186 kHz to 732 kHz compared to 498 kHz in existing LDACS. The tunable bandwidth makes LDACS more flexible and allows to adjust to the local DME interference situation. To support such frame structure, we develop a reconfigurable filtered OFDM (Ref-OFDM) based LDACS PHY and it is the second contribution of this thesis. The Ref-OFDM augments conventional OFDM with dynamic scheduler to support tunable bandwidth and reconfigurable linear phase fixed-coefficient multi-band finite impulse response (FIR) filter to enable on-the-fly control over transmission bandwidth. It also supports multi-band filtering for simultaneous transmission in multiple narrow frequency bands. In addition to the mathematical and performance analysis using synthetic data, we demonstrate the functionality of the proposed Ref-OFDM PHY in a real radio environment on universal software radio peripherals (USRPs) based testbed. The results show that proposed approach offers higher throughput due to wider bandwidth, at least 32 dB reduction in interference to incumbent L-band users and improved BER due to appropriate filtering of legacy user OOB emission compared to existing LDACS.

Most of the ongoing works are focused on the theoretical analysis and multiple antenna extensions of LDACS PHY. From architecture perspective, the performance analysis of LDACS PHY on fixed-point hardware in the presence of various RF impairments and wireless channels/interference is critical and hence, the need to efficiently map LDACS PHY on SoC is the motivation behind the third contribution of this thesis. We design and implement existing as well as proposed LDACS PHY on heterogeneous Zynq SoC (ZSoC) platform, consisting of field programmable gate array (FPGA) as programming logic (PL) and Advanced RISC Machines (ARM) as processing system (PS). The PHY is integrated with the programmable analog front-end to validate its functionality in the presence of various RF impairments and wireless channels and interference specific to the LDACS environment. We propose a novel Hardware-Software co-design approach and explore various PHY configurations by dividing it into PL and PS. Such analysis offers the flexibility to choose the appropriate configuration, as well as the word-length (WL) for a given OOB emission, BER, chip area, delay, and power constraints. Though Ref-OFDM PHY offers superior performance with tunable bandwidth, it incurs significant penalty in terms of resource utilization (27 % higher DSP48 based embedded multiplier) and power consumption compared to OFDM and Windowed-OFDM based LDACS.

The use of filtering leads to increase in chip area, power and delay complexity and hence, design of low complexity reconfigurable filters is the focus of the forth contribution of this thesis. We propose the design of low complexity FIR filter based Ref-OFDM (LRef-OFDM) using a multi-stage filter. The proposed filter is carefully designed to meet the stringent non-uniform spectral attenuation requirements of LDACS using novel interpolation and masking approach. We show that the LRef-OFDM based LDACS offers identical OOB and BER performance to Ref-OFDM with 14.14 % less power and fewer resources (12.78 % DSP48). The L-band spectrum is a scarce resource and, thus spectrum sensing is important for future communication systems. In our fifth and final contribution, we propose a sub-Nyquist Sampling (SNS) sensing based L-band spectrum characterization. The proposed approach replaces high-speed wide bandwidth analog-to-digital converter (ADC) with multiple low-speed narrow bandwidth ADCs. We consider two SNS approaches: 1) modulated wideband converter (MWC) and 2) finite rate of innovation (FRI). SNS is followed by spectrum reconstruction via orthogonal matching pursuit (OMP). To the best of our knowledge, this is the first work exploring SNS for LDACS. We shows that the FRI offers better probability of detection, higher throughput (at lower number of ADCs) and fewer number of sensing failures than MWC and requires lower number of ADCs due to non-contiguous sensing.

In this thesis, we propose a low complexity reconfigurable LDACS FL PHY augmented with SNS based wideband sensing. The proposed work improves the spectrum utilization efficiency of existing LDACS and extend it to support heterogeneous services. In-depth performance analysis, feasibility on SoC and backward compatibility with existing LDACS makes it an attractive alternative for next generation LDACS system.

To my parents, husband and teachers

Acknowledgements

I would like to take this opportunity to express my sincere gratitude and appreciation to a number of incredible people in my life. Without their tremendous guidance, mentoring, help, care, and love, I could not have been what I am today.

First and foremost, I would like to thank my advisor, **Dr. Sumit J. Darak** for his consistent support, guidance, motivation, and encouragement over these years. He chose me as his Ph.D student when I knew nothing about research. He has been phenomenal in nurturing my research capabilities. I remember how he pushed me at the right times and guided me in all technical matters like improving my communication, and technical writing skills. On countless occasions, he boosted my confidence and have never failed to keep my optimism alive. I can't thank him enough for the belief he showed in the moments of disappointments. He is probably one of the most energetic and passionate person I have ever seen. I admire many of his qualities, and no words can suffice my feelings of gratefulness towards him. I am fortunate to have him as my advisor.

I would also like to thank my supervisory committee members: Dr. Anand Srivastava and Dr. Vivek Bohra for their valuable advice, support and constructive feedback through these years. I have benefited from their knowledge and wisdom. The thesis has also benefited from comments and suggestions made by Prof. Faouzi Bader, at Research at Institut Supérieur d'Électronique de Paris (ISEP), in Paris-France.. I take this opportunity to thank him.

I would like to give a special thanks to my lab mates and friends: Rohit Singh, Neelam, Himani, Conducting research with them have been full of fun and excitement. They have helped me broaden my horizons too. I very much appreciate Khagendra Joshi for the help and support in providing the resources required that has made an invaluable contribution towards my PhD.

I must also express gratitude to all of my friends: Mitali Sinha, Mansi Peer,

Ankita Srivastava, Aakash Sharma for giving me the motivation at low times and making my journey memorable. I have never felt time passing faster than when I am talking with them. Finally, I would like to thank Indraprastha Institute of Information Technology-Delhi for providing excellent infrastructure and research environment. I would also like to thank Vivesvaraya PhD scheme for sponsoring my research.

Publications

Journals

J1. **N. Agrawal**, A. Ambede, S. J. Darak, A. P. Vinod and A. S. Madhukumar, "Design and Implementation of Low Complexity Reconfigurable Filtered-OFDM Based LDACS,"in *IEEE Transactions on Circuits and Systems II: Express Briefs,* vol. 68, no. 7, pp. 2399-2403, July 2021, doi: 10.1109/TCSII.2021.3053367.

J2. **N. Agrawal,** S. J. Darak and F. Bader, "Spectral Coexistence of LDACS and DME: Analysis via Hardware Software Co-Design in Presence of Real Channels and RF Impairments,"in *IEEE Transactions on Vehicular Technology,* vol. 69, no. 9, pp. 9837-9848, Sept. 2020, doi: 10.1109/TVT.2020.3002978.

J3. S. Dhabu, A. Ambede, **N. Agrawal** et al., "Variable cutoff frequency FIR filters: a survey." *SN Appl. Sci. 2*, 343 (2020) doi: 10.1007/s42452-020-2140-6

J4. **N. Agrawal,** S. J. Darak and F. Bader, "New Spectrum Efficient Reconfigurable Filtered-OFDM Based L-Band Digital Aeronautical Communication System,"in *IEEE Transactions on Aerospace and Electronic Systems,* vol. 55, no. 3, pp. 1108-1122, June 2019, doi: 10.1109/TAES.2019.2891092.

Conferences

C1. **N. Agrawal,** H. Joshi, S. J. Darak and F. Bader, "USRP Testbed and Performance Analysis of New Reconfigurable LDACS In Presence of DME Interference," *2019 16th International Symposium on Wireless Communication Systems (ISWCS),* Oulu, Finland, 2019, pp. 400-405, doi: 10.1109/ISWCS.2019.8877224.

C2. **N. Agrawal** and S. J. Darak, “Performance Analysis of Reconfigurable Filtered OFDM for LDACS,” *2019 11th International Conference on Communication Systems & Networks (COMSNETS),* Bengaluru, India, 2019, pp. 500-503, doi: 10.1109/COMSNETS.2019.8711421.

C3. **N. Agrawal,** S. J. Darak and F. Bader, “Reconfigurable Filtered OFDM Waveform for Next Generation Air-to-ground Communications,” *2017 IEEE/AIAA 36th Digital Avionics Systems Conference (DASC),* St. Petersburg, FL, 2017, pp. 1-7, doi: 10.1109/DASC.2017.8102025. (Second Best Paper Award)

C4. S. Garg, **N. Agrawal,** S. J. Darak and P. Sikka, “Spectral Coexistence of Candidate Waveforms and DME in Air-to-ground Communications: Analysis via Hardware Software Co-design on Zynq SoC,” *2017 IEEE/AIAA 36th Digital Avionics Systems Conference (DASC),* St. Petersburg, FL, 2017, pp. 1-6, doi: 10.1109/DASC.2017.8102024.

Achievements

A1. NI academic research travel grant 2018 for the paper entitled as “USRP Testbed and Performance Analysis of New Reconfigurable LDACS In Presence of DME Interference”.

A2. 2^{nd} Best paper award in DASC’2017, St. Petersburg, FL for the paper entitled as “Reconfigurable filtered OFDM waveform for next generation air-to-ground communications”.

Contents

List of Figures

List of Tables

List of Abbreviations

A2GC Aircraft to Ground Communication

A2AC Aircraft to Aircraft Communication

AAF Anti Aliasing Filter

ACAS Airborne Collision Avoidance System

ADC Analog-to-Digital Converter

AFE Analog Front End

AMACS All-Purpose Multi-Channel Aviation Communication System

ATC Air Traffic Control

ATM Air Traffic Management

ARM Advanced RISC Machines

ASIC Application Specific Integrated Circuits

ASSP Application-Specific Standard Parts

BAMC Broadband Aeronautical Multi-Carrier Communications

BER Bit Error Rate

BPF band-pass filter

CDM Coefficient Decimation Method

CFO Carrier Frequency Offset

CNS Communications, Navigation, and Surveillance

CP-OFDM cyclic prefix- OFDM

CR Cognitive Radio

CRASH Cognitive Radio Accelerated with Software and Hardware

DAC Digital-to-Analog Converter

DC Direct Current

DDC Digital Down Converter

DME Distance Measuring Equipment

DSB-AM Double Side Band Amplitude Modulation

DTFT Discrete-time Fourier transform

DPD Digital Pre-Distortion

FOFDM Filtered-OFDM

FBMC Filter Bank Multi-Carrier

FCI Future Communication Infrastructure

FDD Frequency Division Duplex

FF Flip Flop

FFT Fast Fourier Transform

FIR Finite Impulse Response

FL Forward Link

FPGA Field Programmable Gate Array

FRM Frequency Response Masking

FRI Finite Rate of Innovation

G2GC Ground to Ground Communication

GFDM Generalized Frequency Division Multiplexing

GSM Global System for Mobile Communication

HDL Hardware Description Language

ICAO International Civil Aviation Organization

IF Intermediate Frequency

IFFT Inverse Fast Fourier Transform

IFIR Interpolated FIR

JTIDS Joint Tactical Information Distribution System

kHz Kilohertz

LDACS L-band Digital Aeronautical Communications System

LDL L-band Digital Link

LNA Low Noise Amplifier

LO Local Oscillator

LRef-OFDM Low Complexity Ref-OFDM

LPP LTE Positioning Protocol

LS Least squares

LSS Lband Spectrum Sensing

LTE Long Term Evolution

MCDM Modified Coefficient Decimation Method

MCS Multi-Coset Sampling

MHz Megahertz

MIMO Multiple-Input and Multiple-Output

MWC Modulated Wideband Converter

NextGen Next Generation Air Transportation System

OFDM Orthogonal Frequency Division Multiplexing

OMP Orthogonal Matching Pursuit

OOB Out-of-Band

OTFS Orthogonal Time Frequency Space

PA Power Amplifier

PAPR Peak to Average Power Ratio

PHY Physical Layer

PL Programming Logic

PM Parks-McClellan

PS Processing System

RCP Required Communication Performance

RD Random Demodulator

Ref-OFDM Reconfigurable Filtered OFDM

RF Radio Frequency

RFADC Radio Frequency Analog to Digital Converter

RL Reverse Link

SDR Software Defined Radio

SESAR Single European Sky ATM Research

SNR Signal-to-Noise Ratio

SNS Sub-Nyquist Sampling

SoA Synchronous or Asynchronous

SoC System-on-Chip

SSR Secondary Surveillance Radar

TDD Time Division Duplex

TF Time-Frequency

UAT Universal Access Transceiver

UFMC Universal Filtered Multicarrier

USRP Universal Software Radio Peripheral

VDL VHF Data Link

VDF Variable Digital Filter

VGA Variable Gain Amplifier

VHF	Very High Frequency
WL	Word-Length
WOLA-OFDM	Windowed Overlap and Add OFDM
WSS	Wideband Spectrum Sensing
ZSoC	Zynq Soc

Chapter 1

Introduction

1.1 Background

The air traffic management (ATM) system ensures the operational procedures and safety of flights and enables reliable communication between the aircraft and ground terminals (air-to-ground communication (A2GC)) as well as between aircrafts (air-to-air communication (A2AC)). Current ATM supports voice communications via analog voice applying the DSB-AM technology. In addition, in the late 1990s, very high frequency (VHF) band (118-137 MHz) digital link (VDL) Mode 2 has been introduced as a low-rate data service to enable first CPDLC (Controller-Pilot Data Link Communications) services. An exponential increase in global air traffic, demands to support heterogeneous services ranging from data to high-speed multimedia, and the need to improve flight safety during flight landing and take-off have compelled communication theorists and engineers to explore further developments of the existing ATM system. In this direction, various research initiatives [1, 2] such as Next Generation Air Transportation System (NextGen) and Single European Sky ATM Research (SESAR) were initiated to modernize the ATM system. Their mandate covers the whole ATM and explores an efficient and reliable future communication infrastructure (FCI) capable of supporting various services ranging from data to multimedia [3, 4]. An envisioned FCI system, shown in Figure 1.1, consists of several communication data links such as satellite communication, ground to ground communication (G2GC), A2GC, and A2AC. The communication link between aircraft and ground terminal via satellite is useful when the aircraft is in oceanic and remote areas. The air-to-air data link supports ad-hoc networks for multi-hop communication as well as direct communication between aircrafts. The air-to-ground link within the FCI handles the two-way communication between an aircraft and the ground for transferring voice and data, such as clearance and instruction messages. In this thesis, we mainly focus on A2GC, which is one of the crucial data links of the FCI system.

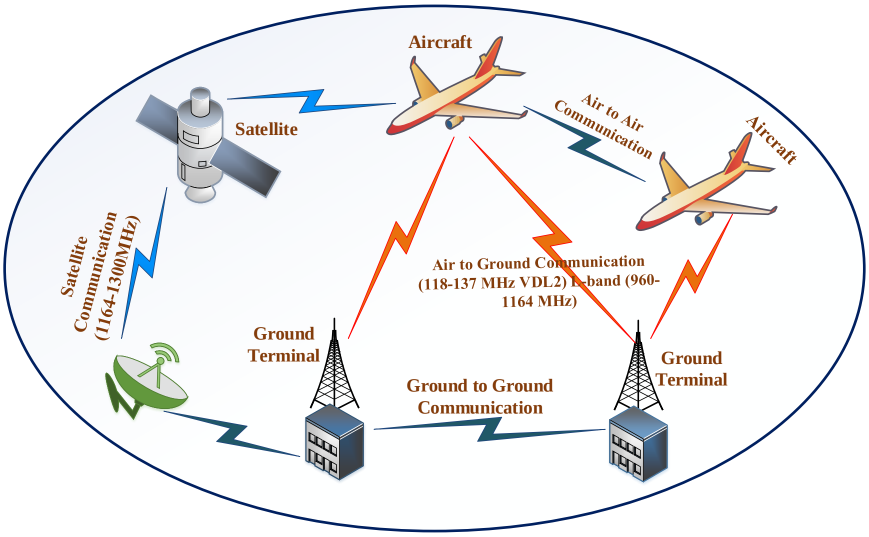

Figure 1.1: FCI system for ATM.

A brief history of the evolution of the A2GC system is depicted in Figure 1.2. In the 1940s, the first A2GC voice link was deployed using the double-sideband amplitude modulation (DSB-AM) in the VHF band (118 - 137 MHz). To improve the robustness and throughout, the International Civil Aviation Organization (ICAO) standardized the first digital data link in the VHF band in 1990, and it is referred to as VHF data link (VDL) standard [4]. It is widely being used in existing ATM systems for A2GC data links, as shown in Figure 1.1. Today, the VDL-based ATM system suffers from severe congestion due to limited bandwidth and low data rate, which limits the number of offered services. Various research studies and spectrum availability analysis aim to overcome these limitations. In 2007, EUROCONTROL launched investigations of a technology similar to B-VHF, but operating in the aeronautical L-band (960–1164 MHz). and which resulted in the *L*-band Digital Aeronautical Communications System (LDACS). In 2009, LDACS specifications were finalized, and the first lab setup for LDACS was demonstrated in 2014. Thereafter, implementation and performance analysis in a real radio environment is being carried out to bring LDACS closer to deployment by 2024.

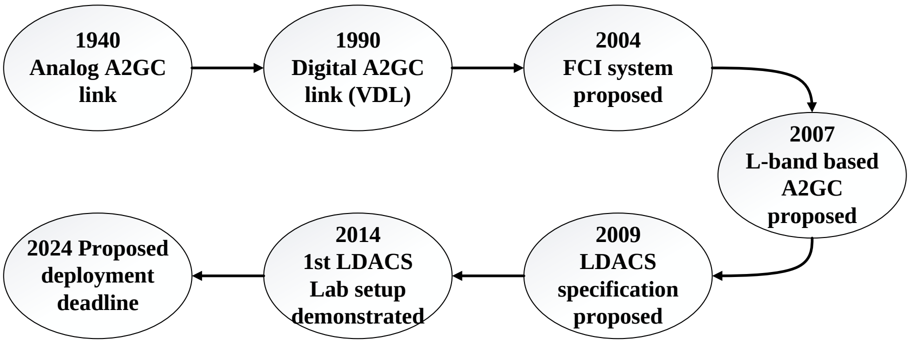

Figure 1.2: Evolution of A2GC system.

The spectrum occupancy of L-band, is shown in Figure 1.3 and it is mostly licensed to existing communication and navigation systems. This includes a distance measuring equipment (DME) signal-based transponder system used for radio navigation. Other legacy or incumbent users are: joint tactical information distribution system (JTIDS), universal access transceiver systems (UAT at 978 MHz), secondary surveillance radar (SSR) at 1030 MHz and 1090 MHz [5].

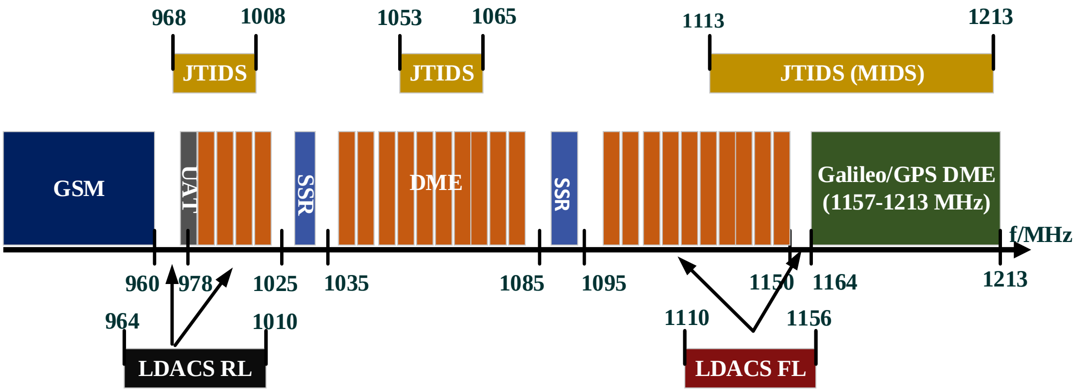

Figure 1.3: L-band spectrum occupancy and incumbent users.

To efficiently exploit the available spectrum in L-band, overlay and inlay approaches [2, 6] are considered. The system is deployed in the vacant spectrum in the overlay approach where no other legacy system is present. In contrast, in the inlay approach, the system is deployed by identifying the spectrum not being used by legacy users. Adjacent DME signals in L-band have a channel spacing of around 1 MHz. The spectrum in between the DME channels can be exploited using a multi-carrier based system via inlay approach and it is referred to as LDACS1. The LDACS1 Broadband multi-carrier system uses the orthogonal frequency division multiplexing (OFDM) as modulation, and its specifications are summarized in Table 1.1. It is designed as a frequency division duplex (FDD) system and a combination of P34 (TIA 902 standard) [7] and the Broadband Aeronautical Multi-carrier Communications (BAMC) system [8, 9] having the overall data rate ranging from 561 kbps - 2.59 Mbps. On the other hand, in 960–975 MHz band, overlay approach using a single carrier based system has been proposed and it is referred to as LDACS2. The LDACS2 is designed as a narrowband single carrier system based on the time division duplex (TDD) approach and the combination of L-band Digital Link (LDL) and the All-purpose Multi-channel Aviation Communication System (AMACS) having the data rate ranging from 70-115 kbps. It is similar to the global system for mobile communication (GSM) and uses a Gaussian minimum shift keying modulation scheme [10]. For the next-generation A2GC system, LDACS1 has been chosen due to the capability to support high-speed delay-sensitive multimedia services and compatibility with the cellular communication standards. The work presented in this thesis is focused on FL transmission of LDACS1 and we will refer to it as LDACS hereafter.

Parameter	**Value**
Effective bandwidth	498.05 kHz
FFT length	64
Used subcarriers	50
Subcarrier spacing	9.765625 kHz
OFDM symbol duration	102.4 μs
Total OFDM symbol duration (includes cyclic prefix)	120 μs

Table 1.1: LDACS1 specifications

1.2 Motivation

Success of orthogonal frequency division multiplexing (OFDM) in cellular and WiFi networks makes it the popular choice for LDACS PHY. LDACS also applies a raised cosine slope with a roll-off factor of 0.107 within a window time of 12.8 μs for better spectrum containment and less out-of-band radiation. It is assumed that DME does not use narrow-band filters at their receiver input. With that, DME might be susceptible to interference even if the transmit spectrum of the potential interferer is strongly contained. Therefore, the existing LDACS PHY to utilizes a fixed transmission bandwidth of only 498 kHz over in between the 1 MHz spectrum grid of DME as shown in Figure 1.4.

An efficient utilization of non-contiguous narrowband spectrum between DME signals is challenging, and hence, various activities to invent breakthrough technologies that provide higher spectral efficiency are being encouraged. Given the history of more than a century of wireless innovation, redesign of the PHY is critical to improving the vacant spectrum utilization.

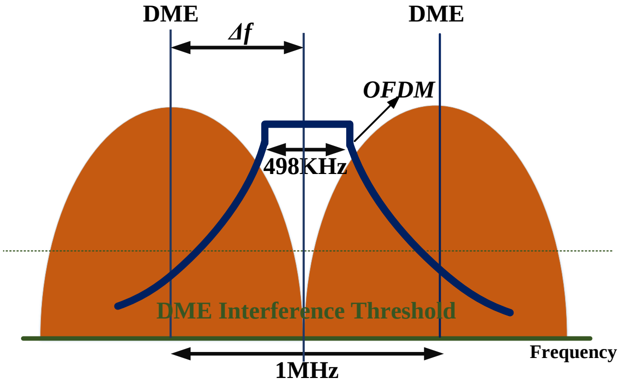

Figure 1.4: LDACS1 deployment scenario.

Most of the existing works focused on the theoretical analysis [11, 12] and multiple antenna extensions [13, 14] of windowed OFDM-based LDACS PHY. One possible approach to improve the spectrum utilization of existing PHY is additional filtering, which reduces the OOB emission further and allows wider transmission bandwidth without compromising the interference to legacy DME users as shown in Figure 1.5. However, the use of filtering may lead to a higher chip area, delay and power consumption hence, the design of low complexity LDACS PHY is desired. The fixed transmission bandwidth of existing LDACS has limited capability to support heterogeneous services demanding different bandwidths and dynamic control over PHY parameters such as OOB emission, transmission bandwidth, etc. Thus, reconfigurable LDACS PHY is desired.

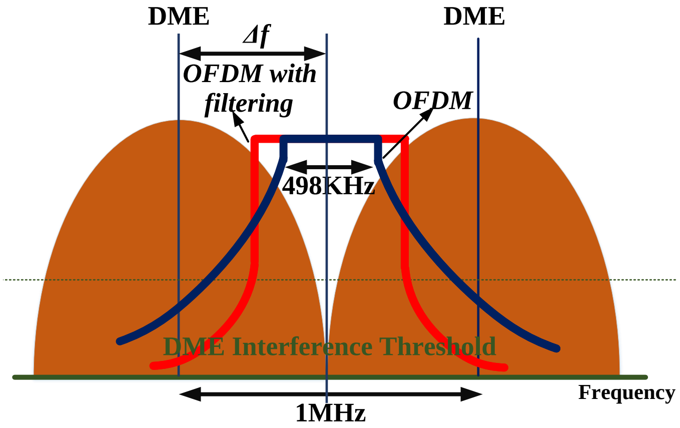

Figure 1.5: Windowed/ Filtered LDACS deployment scenario for a given DME interference threshold.

Additionally, the reconfigurable LDACS PHY needs to satisfy the spectral mask as shown in Figure 1.6 to establish a non-interfering LDACS-DME co-existence scenario. In the spectral mask, the relative attenuation is specified at particular frequencies away from the center frequency of an LDACS channel. The 0 dB level in the mask is the average LDACS transmitter in-band power density. The different attenuation values on the frequency axis are computed considering the LDACS channel bandwidth as 498 kHz. The frequencies away from the center frequency of a LDACS channel and the corresponding attenuation values are: (250 kHz, 0 dB), (337.5 kHz, -34 dB), (625 kHz, -53 dB), (775 kHz, -59 dB), (1250 kHz, -69 dB), (2000 kHz, -76 dB), (4000 kHz, -90 dB).

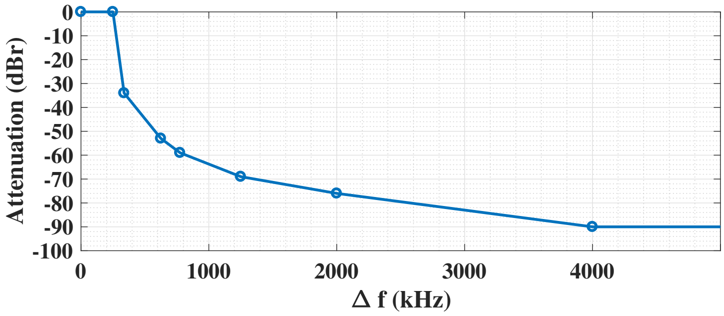

Figure 1.6: LDACS1 spectral mask.

From an architecture perspective, the performance analysis of existing and proposed LDACS PHY on fixed-point hardware in the presence of various radio frequency (RF) impairments and wireless channels/interference is critical to analyze its feasibility on hardware. Furthermore, in a dynamic spectrum environment, the capability to sense the entire L-band as efficiently as possible is desired. Motivated by these open research directions, the work presented in this thesis focus on the design of low complexity reconfigurable LDACS PHY augmented with computationally efficient wideband sensing and in-depth performance analysis on system-on-chip (SoC).

1.3 Research Objectives and Major Contributions

The work presented in this thesis aims to address the research challenges related to the design of reconfigurable and low complexity LDACS PHY and efficient implementation on SoC. These challenges will be addressed via the following research objectives:

- Study existing LDACS and modify it to support new frame structure to enable tunable transmission bandwidth without compromising on backward compatibility.

- Design a reconfigurable LDACS PHY using tunable digital filtering to support tunable transmission bandwidth and investigate its performance via synthetic as well as real radio signals.
- Explore various low complexity tunable digital filters to optimize the hardware complexity without compromising on PHY performance.
- Explore hardware-software co-design to map the proposed LDACS PHY on heterogeneous Zynq SoC from Xilinx consisting on processing systems (PS) i.e. ARM processor, programmable logic (PL) i.e. field programmable gate array (FPGA) and RF front end, AD9361 from Analog Devices.
- In-depth performance analysis on fixed-point hardware in the presence of RF impairments and wireless channels/interference.
- Design low complexity wideband sensing to identify spectrum opportunities in a frequency range of 204 MHz in L-band.

Various contributions of this thesis to meet the above research objectives are summarised as follows:

A1. Our first contribution is to propose a new LDACS PHY frame structure comprising of data, null, and reference signals to support tunable bandwidth ranging from 186 kHz to 732 kHz. The proposed frame structure is backward compatible with the existing LDACS frame structure when the transmission bandwidth is 498 kHz. The frame structure is designed with the standard sub-carrier spacing and symbol duration of 9.76 kHz and 102.4 μs, respectively.

A2. Using the new frame structure, we proposed a reconfigurable filtered OFDM (Ref-OFDM) based LDACS PHY which is the second contribution of this thesis. The Ref-OFDM uses a reconfigurable linear phase fixed-coefficient multi-band finite impulse response (FIR) filter to enable on-the-fly control over transmission bandwidth. Filtering results in lower interference to incumbent L-band legacy users and wider tunable transmission bandwidth (186 kHz - 732 kHz). The reconfigurable filter also supports multiple narrowband transmissions leading to significant improvement in the vacant spectrum utilization. Along with theoretical and performance analysis using synthetic data, we also demonstrate the functionality of the proposed Ref-OFDM PHY in a real radio environment on universal software radio peripherals (USRPs) based testbed. The simulation and experimental results show the proposed PHY significantly improves the BER, throughput, and achieves at least 32 dB lower interference to incumbent L-band users than existing LDACS.

A3. From an architecture perspective, the performance analysis of LDACS PHY on fixed-point hardware is critical. Hence, mapping of PHY on SoC is the main motivation behind the third contribution of this thesis. We design and implement existing and proposed LDACS PHY on heterogeneous Zynq System on Chip (ZSoC) platform using the hardware-software co-design workflow of MATLAB and Simulink. Such a co-design approach gives the flexibility to choose which part of the PHY to implement on PL and which on PS to meet the given area, delay and power constraints. The various PHY architectures are then integrated with analog front-end to endorse its performance in the presence of various RF impairments, DME interference, and wireless channels. Though Ref-OFDM PHY offers superior BER, OOB emission and throughput performance, it incurs a higher penalty in resource utilization (27 % higher DSP48 based embedded multiplier) and power consumption.

A4. The fourth contribution of the thesis focused on improving the resource and power consumption of Ref-OFDM. The proposed low complexity reconfigurable filtered OFDM (LRef-OFDM) based LDACS is designed using novel interpolation and masking-based multi-stage FIR filter. The proposed filter offers tunable bandwidth, satisfies the stringent spectral attenuation requirements of LDACS and offers significantly lower complexity. We show that the LRef-OFDM based LDACS offers identical OOB and BER performance to Ref-OFDM with 14.14 % less power and fewer resources (12.78 % DSP48).

A5. The spectrum is a scarce resource and, thus spectrum sensing is important for future communication systems. A sub-Nyquist Sampling (SNS) based L-band spectrum characterization is proposed in the fifth and final contribution. The proposed approach replaces high-speed wide bandwidth analog-to-digital converter (ADC) with multiple low-speed narrow bandwidth ADCs. We consider two SNS approaches: 1) Modulated wideband converter (MWC) and 2) Finite rate of innovation (FRI). SNS is followed by spectrum reconstruction via orthogonal matching pursuit (OMP). To the best of our knowledge, this is the first work exploring SNS for LDACS. We show that the FRI offers a better probability of detection, higher throughput (at lower number of ADCs), and fewer sensing failures than MWC and requires a lower number of ADCs due to non-contiguous sensing.

1.4 Outline of Thesis

The rest of the thesis is organized as follows. Chapter 2 gives an overview of the existing LDACS and its extensions. A literature review of numerous LDACS PHY waveforms, digital filter design and hardware platforms is provided. Chapter 3 demonstrates the functionality of the proposed Ref-OFDM based LDACS PHY, and it's performance analysis uses synthetic data and real radio signals. In Chapter 4, the architecture of the proposed LDACS-PHY is designed and implemented on the ZSoC platform. Its performance is evaluated on fixed-point hardware in the presence of various RF impairments and wireless channels/interference. Chapter 5 presents a power-efficient and LRef-OFDM based LDACS using a multi-stage FIR filter. The work described in Chapter 3- Chapter 5, concentrates on the design of reconfigurable and low complexity LDACS PHY and its performance analysis in a real-radio environment and feasibility on SoC. In Chapter 6, a SNS based L-band spectrum characterization is presented to identify vacant spectrum opportunities in L-band for better spectrum utilization.

Chapter 7 concludes the thesis with some possible future directions.

Chapter 2

Literature Review

In this chapter, we review the various state-of-the-art works related to air-to-ground communication in FCI. We begin with the existing LDACS and its extensions, LDACS PHY waveforms, and digital filter design. In the end, we discuss the various hardware platforms available for the LDACS prototype and existing LDACS testbeds.

2.1 LDACS Specifications and Extensions

As discussed in Chapter 1, the LDACS system can be deployed in the L-band using two overlay and inlay approaches. In the overlay approach, it is deployed in the vacant spectrum where no other legacy system is present. This approach is straightforward and chosen for GSM like LDACS2 in the 960-975 MHz vacant band. On the other hand, LDACS1 is deployed using an inlay approach in between the 1 MHz frequency grid of DME signals. The LDACS1 Broadband multicarrier system uses the OFDM due to the capability to support high-speed delay-sensitive multimedia services and compatibility with the cellular communication standards. LDACS1 also applies a raised cosine slope with a roll-off factor of 0.107 within a window time of 12.8 μs.

The LDACS physical layer specifications and their usefulness for CNS applications are summarized in [10, 15, 16]. In [10, 15], the channel bandwidth of LDACS1 is specified as 498.05 kHz, used by an OFDM system with 50 sub-carriers, resulting in a sub-carrier spacing of 9.765625 kHz. The existing LDACS is used for data or voice communication between aircraft and ATC, recording and controlling aircraft movement, determining aircraft position, etc.

In [16], LDACS system performance has been analyzed for both inlay and overlay approaches. The authors have applied additional methods such as pilot boosting and pilot erasure, leading to a system performance close to that achievable with perfect channel knowledge. The results in [16] show the compatibility of LDACS with the DME signal in the critical inlay approach.

The theoretical results presented in [6, 17] confirm the inlay approach's feasibility in the L-band. The authors have analyzed the DME power and pulse rate effect on the BER of inlay approach-based LDACS. Also, the analysis is limited to the DME interference specific to European aerospace. The result obtained during compatibility measurements of LDACS carried out at labs of the German Air Navigation Service Provider are presented in [18]. The authors have considered various possible interference scenarios for the inlay deployment. The experimental results show that the LDACS DME co-existence is feasible in the most strict inlay environment and claimed that additional device under tests (DUTs) could be included to prove the compatibility in other interference scenarios. In [19], a new model has been proposed to evaluate and compare the performance of various FCI links as per the required communication performance (RCP) metric introduced by the ICAO. The analysis has also identified the desired characteristics for any data link to meet RCP requirements.

In [20–22], interference analysis is done via characterizing various incumbent users in the L-band in terms of their spectral characteristics, transmit power, and the duty cycle. The simulation results in [20] show a slight degradation in the BER performance of LDACS for higher DME power. Two algorithms have been proposed to mitigate the DME interference, in [21] and [22]. In [21], the pulse blanking technique has been proposed for interference mitigation by reconstructing and subtracting ICI. The required shape of the subcarrier spectra is derived from the pulse blanking window. The authors have also proposed an iterative receiver design to estimate the transmitted data symbols and the channel coefficients of each subcarrier. Supervised learning-based DME multipath mitigation technique, performance, and sensitivity analysis are presented in [22].

The works in [23, 24] validate the performance of LDACS in the presence of incumbent L-band users on the hardware testbed at intermediate frequency level. These tests validate the fixed-point implementation of LDACS. Experiments in real radio environments are being carried out to analyze the effect of nonlinearities in the power amplifier and analog-front-end on the performance of LDACS.

Apart from the transmitter, the design of the L-DACS1 receiver is introduced using methods for mitigating interference from other L-band systems in [16]. On the receiver side, reconfigurable low complexity filter and filter bank architectures for channelization and spectrum sensing applications have been proposed in [25,26]. Such architectures are based on the frequency response masking approach, and they allow the LDACS receiver to receive or sense single and multiple frequency bands simultaneously.

Most of the existing works deal with improving the performance of the existing LDACS system. Windowed OFDM still has high out-of-band emission. To design an FCI system for various CNS applications, it must offer large transmission capacity, low latency, and high elasticity, along with the capability to support a wide variety of services. For this, OFDM alone may not be sufficient, and hence, a reconfigurable transceiver that can support multiple waveforms needs to be developed. A brief review of the candidate waveforms for such transceivers is presented in the next section.

2.2 LDACS PHY Waveforms

Here, we briefly review the candidate waveforms that can replace OFDM to improve the transceiver system according to today's requirements. Various work has been done on improvising these waveforms in terms of complexity, PAPR, PSD, BER, etc. Please refer to Table 2.1 for a comparison of these waveforms.

Figure of Merit	**OFDM**	**FOFDM**	**WOFDM**	**FBMC**	**GFDM**
PAPR	High	High	High	High	Moderate
OOB Emission	High	Low	Low	Low	moderate
Spectral Efficiency	Low	Low	Low	High	High
Complexity	Low	Moderate	Moderate	High	High
MIMO Support	Yes	Yes	Yes	Challenging	Challenging

Table 2.1: Comparison of candidate waveforms

2.2.1 Orthogonal Frequency Division Multiplexing (OFDM)

At present, OFDM is a widely adopted waveform for wireless physical layer due to its robustness against multipath channels and Fast Fourier Transform (FFT) based computationally efficient architecture. The basic OFDM transceiver architecture is shown in Figure 2.1. In OFDM, the randomly generated input bitstream is encoded via a channel encoder. The encoded data is modulated by an appropriate modulation scheme such as BPSK, QPSK, 16 QAM, and 64 QAM, followed by the symbol to frame mapping for given transmission bandwidth. These complex symbols are then mapped to orthogonal subcarriers using N point IFFT. A CP of length N_{CP} is added to the OFDM symbol to avoid inter-symbol interference. In the end, the signal is transmitted over the wireless channel via an RF transmitter. The receiver performs similar operations in reverse order. To further improve the transceiver performance, various waveforms such as generalized frequency division multiplexing (GFDM) [11,27,28], windowed overlap and add OFDM (WOLA-OFDM) [29], universal filtered multicarrier (UFMC) [30], filter bank multicarrier (FBMC) [11, 31] and filtered-OFDM (FOFDM) [27,32–35] are being studied. Also, in the past, OFDM has been successfully deployed in 4G LPP and Wi-Fi standards [11,27], and similar work on waveforms is being done for these cellular networks [11,27–35].

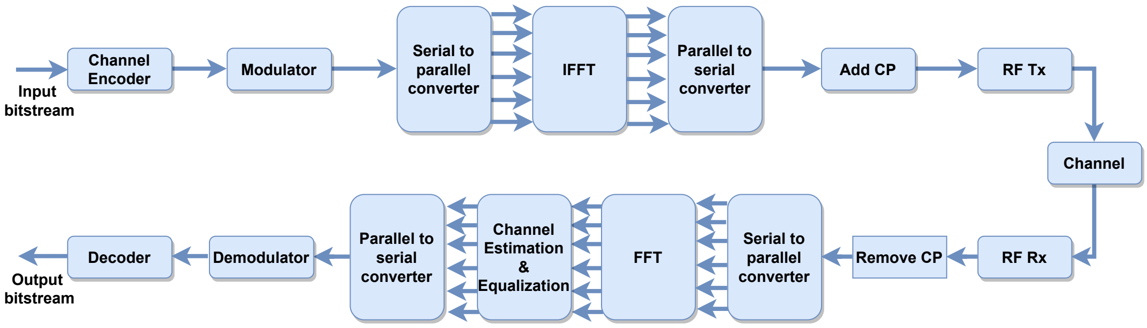

Figure 2.1: Transceiver architecture of OFDM [36].

The time-frequency lattice structures of these waveforms for a transmission bandwidth B are shown in Figure 2.2. Here, $d_{k,m}$ is the data transmitted on the k^{th} subcarrier and in the m^{th} sub-symbol of the block. Therefore, the total number of symbols is $N = KM$. In OFDM, there are N sub-carriers, and one symbol is transmitted on each sub-carrier, whereas the GFDM is a block-based approach that spread the data across a two-dimensional (time and frequency) block structure (multi-symbols per multicarriers) as shown in Figure 2.2a and 2.2b respectively. Other waveforms such as FOFDM, WOLA-OFDM, UFMC, FBMC follow the similar time-frequency (TF) lattice structure as OFDM.

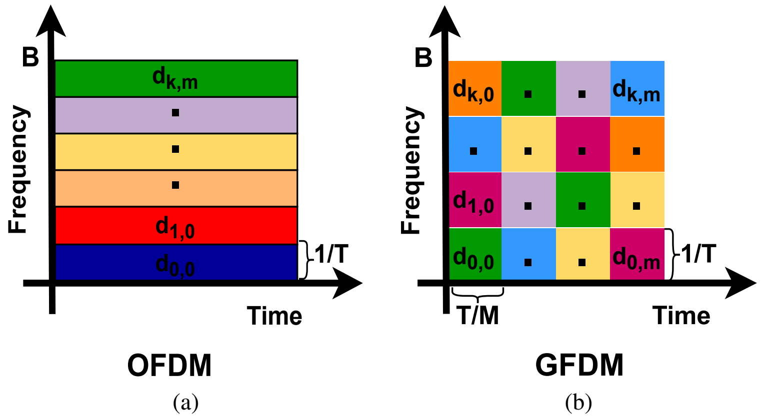

(a) (b)

Figure 2.2: TF lattice structure [37] of (a) OFDM (b) GFDM.

2.2.2 Generalized Frequency Division Multiplexing (GFDM)

A flexible multicarrier modulation scheme, named GFDM, has been proposed in [28] for the air interface of 5G networks. GFDM is a block-based, non-orthogonal multicarrier transmission scheme. It spread the data across a two-dimensional (time and frequency) block structure (multi-symbols per multicarriers) and employs circular pulse shaping. The subcarriers are filtered with a prototype filter that is circularly shifted in the time and frequency domain. A data block is composed of K carriers and M time slots and transmits $N = KM$ complex modulated data as shown in Figure 2.2b. The GFDM transceiver architecture is shown in Figure 2.3. Subcarrier filtering offers a trade-off between spectral efficiency and complexity. Also, The architectural difference of GFDM with the existing OFDM does not provide backward compatibility, making it less suitable for future A2GC.

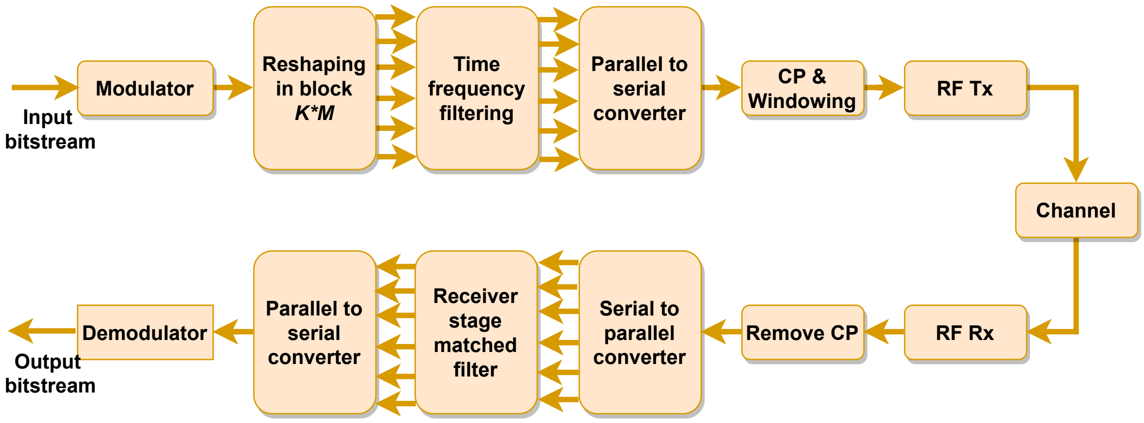

Figure 2.3: Transceiver architecture of GFDM [36].

2.2.3 Universal Filtered Multicarrier (UFMC)

In [30], UFMC has been proposed to overcome the drawbacks of OFDM. [30] presents the UFMC where a group of subcarriers is filtered to reduce the OOB emission. The block diagram of UFMC is shown in Figure 2.4. UFMC does not require a CP, and it is possible to design the filters to obtain a total block length (L) equivalent to the CP-OFDM. However, because there is no CP, UFMC is more sensitive to small-time misalignment than cyclic prefix- OFDM (CP-OFDM) and FOFDM.

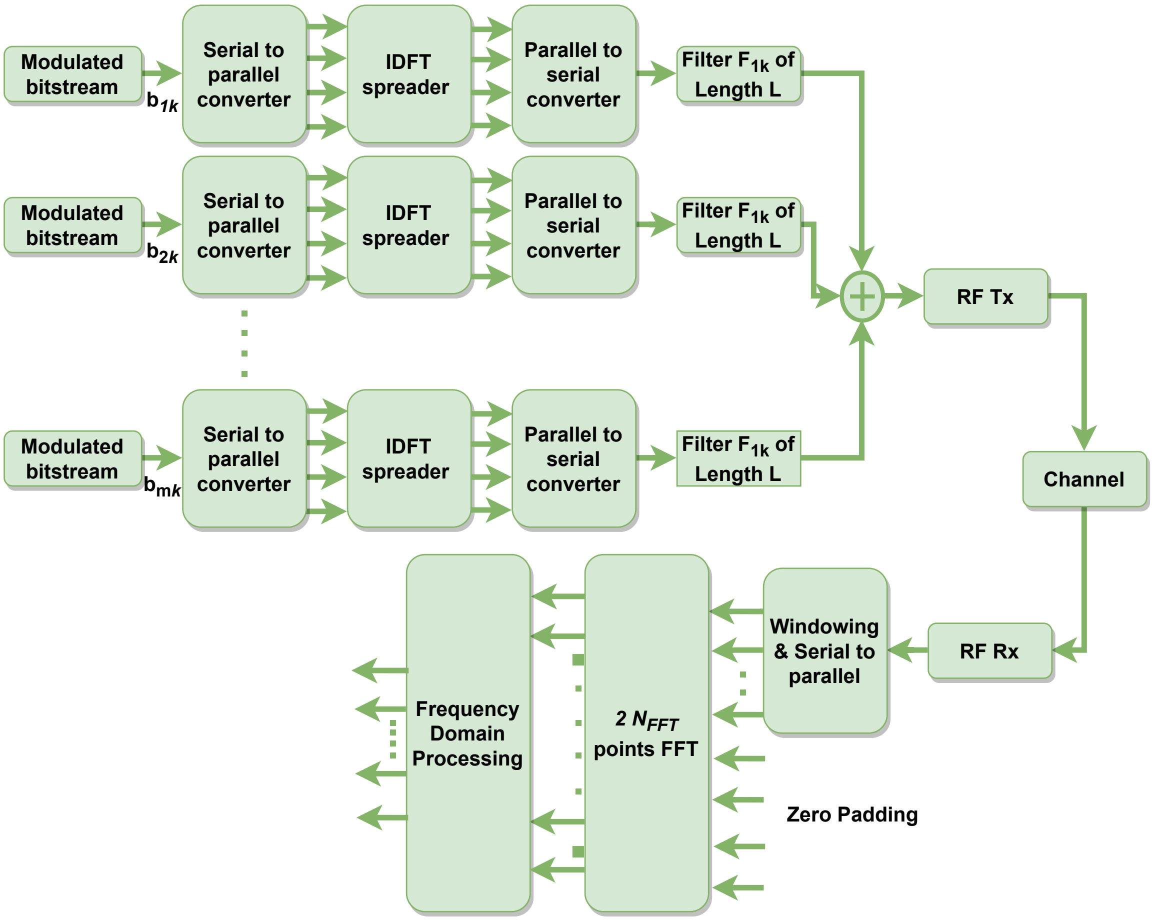

Figure 2.4: Transceiver architecture of UFMC [36].

2.2.4 Filter Bank Multicarrier (FBMC)

The replacement of OFDM-based LDACS transceivers using FBMC is presented in [31]. The FBMC consists of a set of parallel data which are transmitted through a bank of modulated filters. The basic transceiver architecture of FBMC is shown in Figure 2.5. From the architecture perspective, the complexity of FBMC is high, and receiver design is challenging due to complex synchronization and channel equalization techniques. Since the architecture of FBMC is significantly different from that of OFDM, the single transceiver can not support both waveforms unless they are stacked in parallel. FBMC cannot be easily extended to multiple antenna configurations from the future perspective, which is now a default configuration offering high data rates and improved performance in the deep fading environment.

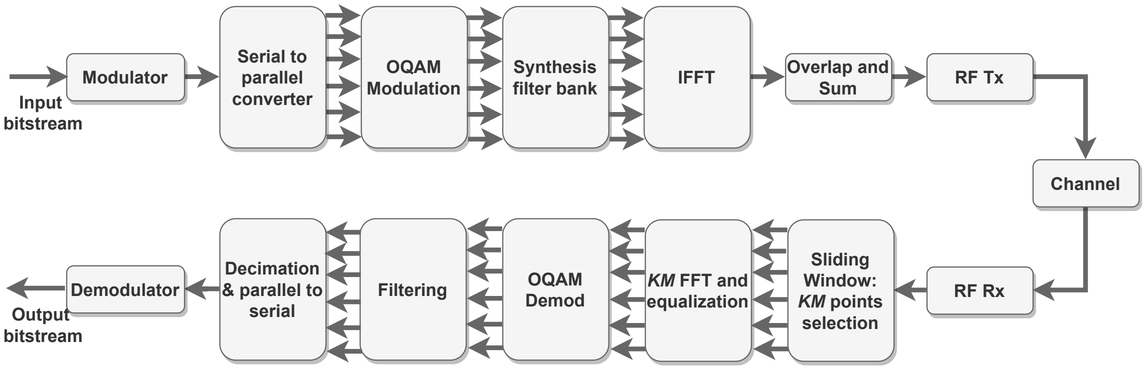

Figure 2.5: Transceiver architecture of FBMC [36].

2.2.5 Windowed Overlap-Add OFDM (WOLA-OFDM)

In WOLA-OFDM, the conventional rectangular window is replaced by a windowing pulse with soft edges to improve the out-of-band emission of CP-OFDM. This smooth edge windowing is applied in the time domain via point-to-point multiplication between the CP block and window function output. It has recently been adopted in 4G and aeronautical communication systems [29]. Such windowing at the transmitter demands additional signal processing at the receiver to suppress the asynchronous inter-user interference. The basic architecture of WOLA-OFDM is shown in Figure 2.6, which is very similar to OFDM except for the additional time-domain windowing at the transmitter and overlap-add processing at the receiver.

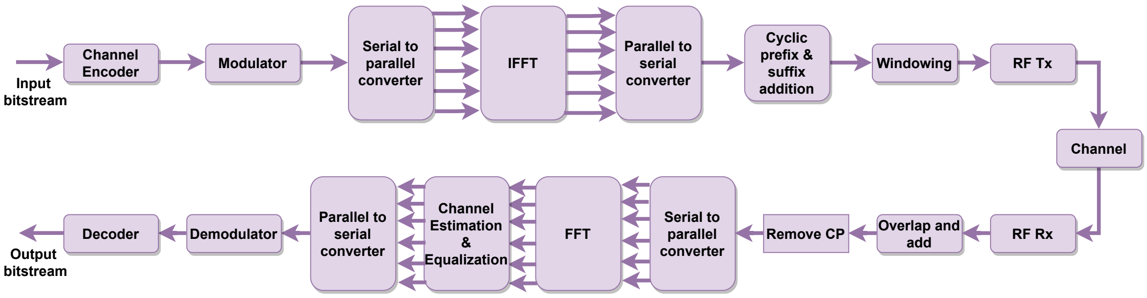

Figure 2.6: Transceiver architecture of WOLA-OFDM [36].

2.2.6 Filtered OFDM (FOFDM)

The FOFDM uses a linear phase finite impulse response filter instead of time-domain windowing to further improve the out-of-band emission. In [27], the broadband aeronautical communication with the waveform designed based on L-DACS1 and FOFDM is proposed and evaluated. The transceiver architecture of FOFDM is shown in Figure 2.7. However, the filter needs to be carefully designed and implemented as it may lead to higher inter-symbol and inter-carrier interference. The FOFDM based LDACS in [31] has the fixed transmission bandwidth and can not adapt the dynamic transmission bandwidth on the fly. Additional filtering increases the complexity very high in multi-band or multi-user transmission at different bandwidths as this will require other filters for each bandwidth. The complexity can be further reduced by introducing bandwidth reconfigurable filtering, which requires a single filter for different transmission bandwidths.

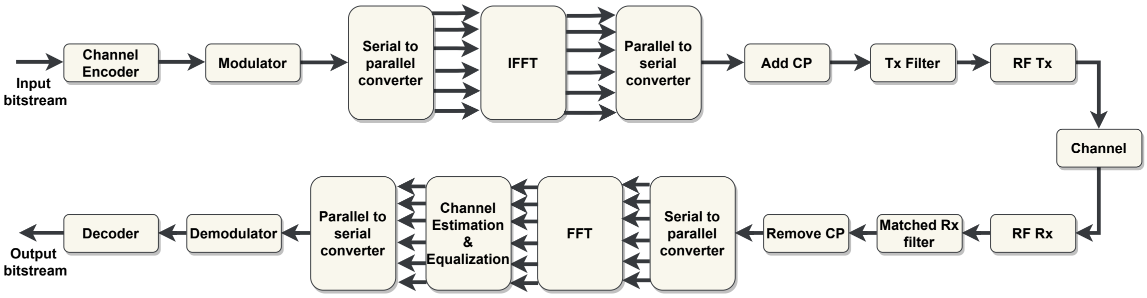

Figure 2.7: Transceiver architecture of FOFDM [36].

Here, we reviewed various candidate waveforms for future A2GC. The waveforms presented in [27,28,30,31], are efficient in their own terms but are not suitable for LDACS transceivers as the architectures of FBMC [31] and GFDM [28] are significantly different from that of OFDM. It cannot be easily extended to multiple antenna configurations from the future perspective, which is now a default configuration offering high data rates and better performance in deep fading. Time misalignment of UFMC discussed in [30] makes it inappropriate for A2GC. Since WOLA-OFDM and FOFDM have OFDM as their core waveform, switching between three waveforms on the fly is possible. However, FOFDM complexity is higher than OFDM due to the filtering. The design of a low complexity filter and making it reconfigurable for tunable transmission bandwidth poses a real challenge. Further, reducing the LDACS PHY complexity is essential to extend the battery life. The following section will discuss numerous filter design methods for the future generation of low complexity reconfigurable LDACS PHY.

2.3 Filter Design

Numerous filter design approaches employing the interpolation technique have been proposed to obtain low complexity FIR filters. For example, a computationally efficient digital filter based on interpolation and frequency-response-masking (FRM) technique is presented in [38]. In this paper, the designed filter is optimized in a mini-max sense by jointly optimizing the sub-filters involved using a convex-concave procedure. The authors also extend the work to the design of FRM filters that simultaneously promotes the filter coefficients' sparsity to reduce implementation complexity. Reconfigurable low complexity filter and filter bank architectures for channelization and spectrum sensing applications have been proposed in [25, 26]. Such architectures are based on the FRM approach [39, 40], and they allow the LDACS receiver to receive and sense single as well as multiple frequency bands simultaneously. The block diagram of FRM technique and corresponding frequency responses at various stages are shown in Figure 2.8 and 2.9 respectively. In the interpolated FRM filter approach, firstly a prototype lowpass filter $H_l(z)$ is designed of odd length N, then the corresponding complementary filter $H_c(z)$ is obtained by subtracting the output of the prototype filter from the delayed version of the input. Later both the filters are interpolated by the interpolation factor M to get multiband responses $H_l(z^M)$, $H_c(z^M)$ presented in Figure 2.9 (b) and the undesired bands are masked with the two cascaded lower-order masking filters $H_{ml}(z)$ and $H_{mc}(z)$ respectively as shown in Figure 2.9 (c). The final low pass response using the FRM approach is shown in Figure 2.9 (d).

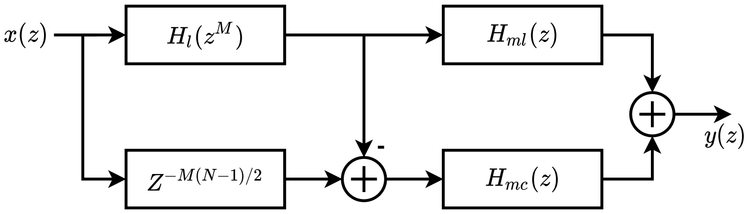

Figure 2.8: Sharp transition bandwidth digital filter based on the FRM technique [38].

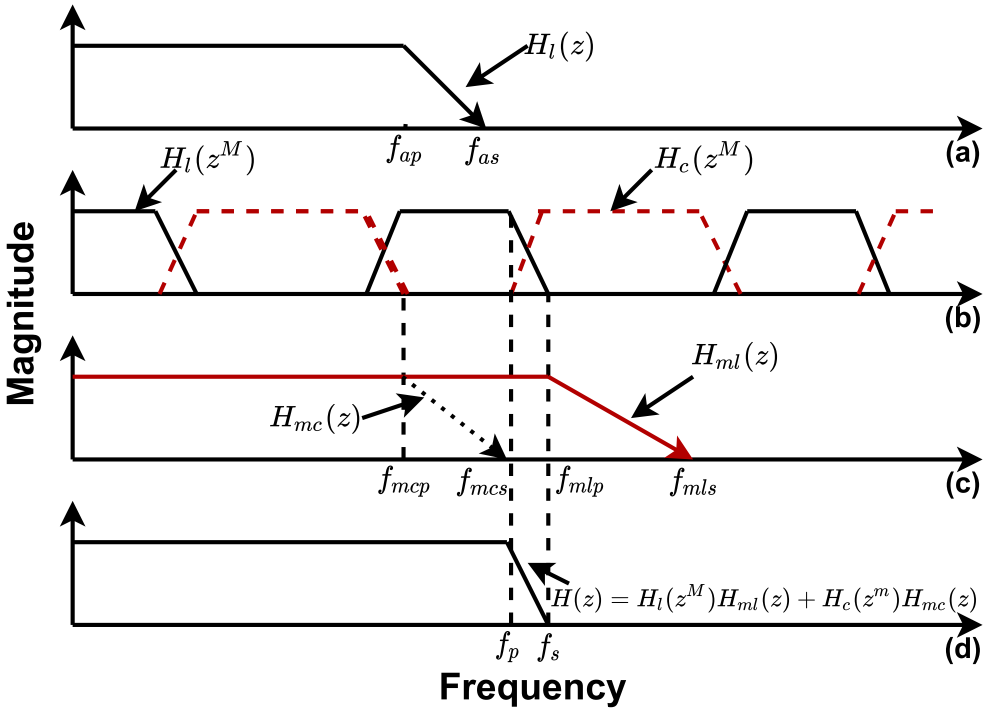

Figure 2.9: Frequency response illustration of the FRM technique.

Similarly, interpolation-based narrow-band sparse FIR filters and centrosymmetric bandpass filters are designed in [41]. The design method is realized by cascading a model filter with a sparse masking filter. The model filter is first designed and then interpolated to generate the desired impulse response replica in this technique. A sparse masking filter is used to mask the extra unwanted passbands. A low complexity 17-band non-uniform Interpolated FIR (IFIR) filter bank for digital hearing aid applications are designed in [42]. In this paper, a low complex 17-band non-uniform IFIR filter bank is proposed for digital

	Cutoff frequency range	**Transition bandwidth** t_{bw}	**Flexibility**	**Complexity**	**Group delay**	**Narrow** t_{bw} **suitability**	**Center frequency resolution for bandpass responses**
Coefficient decimation - type I (CDM-I, MCDM-I)	Nyquist band	Fixed	Medium	Medium	$> N/2$	Yes	$2/D_{max}$ for CDM and $1/D_{max}$ for MCDM
Coefficient decimation - type II (CDM-II, MCDM-II)	Nyquist band	Variable	Low	High	$> N/2$	No	
Interpolation - FRM	Nyquist band	Variable	Low	Very low	$>> N/2$	Yes	$2/M_{max}$
Coefficient decimation + interpolation	Nyquist band	Variable	High	Low	$> N/2$	Yes	$2/M_{max}$
Improved coefficient decimation + interpolation	Nyquist band	Variable	Very high	High	$> N/2$	Yes	$1/M_{max}$
Interpolation + Farrow structure [44]	Nyquist band	Variable	Very high	Very High	$>> N/2$	Yes	$1/M_{max}$

Table 2.2: Qualitative comparison of digital filters with *discrete* control over cutoff frequency

hearing aid applications. The band filters are generated using different levels of interpolations on a linear phase prototype lowpass filter.

An interpolated band-pass method based narrow-band finite impulse response (FIR) filter for 5G cellular network is proposed in [43]. The proposed filter consists of different sub-filters such as prototype filter, $H_a(e^{j\omega})$, complementary prototype filter $H_c(e^{j\omega})$. The approach considers a band-pass filter (BPF), $H_{bp}(e^{j\omega})$ placed in between prototype and complementary prototype filter pair.

The FRM and interpolation-based filters are not suitable when multiple responses, each with different cut-off frequencies, are required. To fulfill the requirement, authors in [45–48], proposed a bandwidth reconfigurable filter and filter banks using the CDM and MCDM. These methods involve the selective usage of filter coefficients by performing operations such as replacing them with zeros and retaining/discarding them appropriately to get variable lowpass, highpass, bandpass, and bandstop responses. Various digital filters having discrete control over cut-off frequency are compared in Table 2.2.

The$L$-band spectrum is a scarce resource and, thus spectrum sensing is important for future communication systems. Some of the sensing techniques to sense the L-band spectrum are reviewed in the next section.

2.4 L-Band Spectrum Sensing

The OFDM-based LDACS system is deployed in between the DME channels having 1 MHz channel spacing. In this inlay approach, identifying the available spectrum resources in L-band is necessary to improve further the transmission capacity and the systematic use of the spectrum. Using the spectrum sensing technique, we can sense the presence of DME signals. The LDACS can be further deployed in a wider bandwidth along with the multi-band and multi-user transmission channels where the DME signal is not present. Authors in [49], designed a cognitive radio (CR) approach based on spectrum sensing and spectrum management technique for detecting idle L-band in DME and allocate them to an L-DACS. In [50], a novel sensing method for detecting the active LDACS transmissions via a multiplier-less correlation-based method has been proposed. An energy-difference detection-based spectrum sensing scheme for CR-enabled LDACS system is proposed in [51].

Authors in [51] also present a power-efficient wideband spectrum sensing (WSS) based on SNS, providing the best accuracy-complexity trade-off. The characterization of L-band via SNS is not handled in the literature yet. Still, there are numerous techniques present to sense a wide band spectrum such as random demodulator (RD) [52], Multi-Coset Sampling (MCS) [53], MWC [54], FRI [55]. The RD [52] is used to sense only multi-tone signal, and the wideband signal is an infinite tone signal which makes the computation very expensive. Unlike RD, which generates samples via a single low rate ADC, the MCS [53] uses p synchronized ADCs for the digitization. MCS requires picoseconds time delay, which makes the synchronization very hard between ADCs. The MWC [54] has p branches in which each branch follows the same architecture as RD. MWC digitized all the frequency sub-bands present in the wideband. FRI [55] follows the same architecture as MWC except that it digitizes only the frequency bands of interest.

To recover the frequency bands several compressive sensing recovery algorithms like l_1-norm minimization [56,57], OMP [58,59], iterative threshold [60] etc. are discussed in the literature. A joint spectrum sensing and interference mitigation scheme is also developed in [49] to detect and mitigate the effect of DME interference on the LDACS system.

A brief review about the existing sensing techniques is presented above to sense a wide band spectrum such as RRD [52], MCS [53], MWC [54], FRI [55]. To recover the frequency bands several compressive sensing recovery algorithms like l_1-norm minimization [56, 57], OMP [58, 59], iterative threshold [60] etc. are discussed here.

2.5 Hardware Implementation

In this section, we review and compare the available hardware platforms and discussed numerous works done using these platforms and the work done to analyze the performance of existing LDACS.

The implementation of various blocks in the conventional OFDM-based LDACS on homogeneous platforms such as field-programmable gate arrays (FPGA) or application-specific integrated circuits (ASIC) have been discussed in [62–64]. A comparison of various hardware platforms [65, 66] is presented in Table 3.4. As shown in Table 3.4, the homogeneous platforms are application-specific [66] and have limitations of flexibility and scalability, and may not be suitable for var-

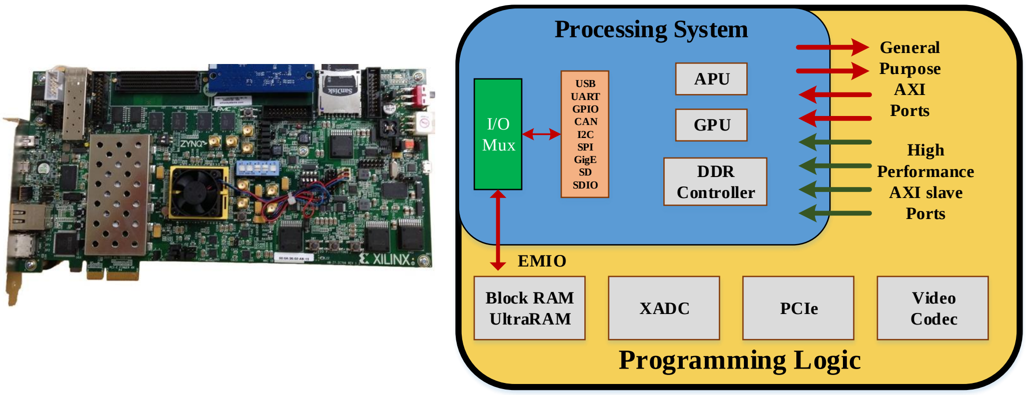

Figure 2.10: Xilinx ZC706 evaluation board along with its important architectural features [61].

ious real-time decision-making tasks. Though they lack in hardware (hw) - software (sw) integration, these platforms are power efficient and offer good performance. Two-chip solutions with a separate chip for hardware and software allow hardware - software reconfigurability but are not power and cost-efficient. With the new applications coming up, higher degrees of flexibility, reconfigurability, and scalability are required. Hence, recently, heterogeneous platforms consisting of processors and hardware such as FPGA or ASIC on a single chip are being explored. Thus, Xilinx introduced Zynq-7000 all programmable system-on-chip/software-defined radios. The Zynq System on Chip platform consists of FPGA as PL and Advanced RISC Machines (ARM) as PS as shown in the architecture Figure 2.10. PS makes easy and faster decision-making operations; conversely, PL reduces power consumption and increases speed. Different variants of zynq can have different sizes but have same software stack provides scalability to the application design. Also, the reconfigurability of ZSoC allows the functionality to be customized according to the application at run time. Comparison of various platforms such as ASIC, application-specific standard parts (ASSP), 2-chip solution, and ZSoC is shown in the Table 3.4.

	ASIC	ASSP	2-Chip Soln	ZSoC
HW Reconfigurability	-	-	+	+
SW Reconfigurability	-	-	+	+
Power	+	+	-	+
Scalability	-	Avg	+	+
Performance	+	+	Avg	+
HW-SW integration	-	-	+	+

Table 2.3: Comparison of various platforms

To design and simulate the transceiver models, the hardware-software co-design approach is essential as it utilizes PS and PL heterogeneity. The hardware-software co-design approach for the IEEE 802.11a transceiver system is discussed in [67]. In this approach, the transceiver is divided into two subsystems, one to be implemented on PS and another on PL, as shown in Figure 4.3. Details about the approach are presented in Chapter 4.

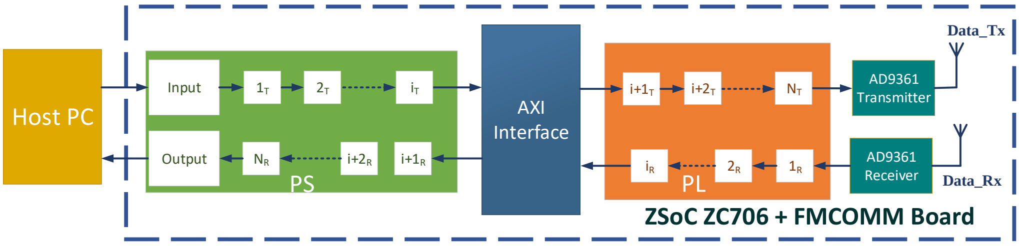

Figure 2.11: Hardware-Software co-design approach for algorithm implementation.

The authors in [68] describe and analyze the Zynq7000 SoC from an evolvable hardware perspective. In FPGA-based evolvable hardware, the evolutionary algorithm (EA) generates candidate configurations used to configure chosen reconfigurable blocks of the FPGA. Their experiments confirmed the platform's superiority for evolving hardware design in the context of area overhead, execution time, reconfiguration time, and throughput. A cognitive radio accelerated with software and hardware (CRASH) is introduced in [69]. CRASH is a versatile heterogeneous computing framework for the Xilinx Zynq SoC. They have implemented spectrum sensing and the spectrum decision in three configurations: 1. both algorithms in the FPGA, 2. both in software only, and the last is spectrum sensing on the FPGA and spectrum decision on the CPU. Their experiments show that CRASH can successfully segment two cognitive radio algorithms, spectrum sensing and the spectrum decision, between the Zynq's

FPGA fabric and ARM processors.

In [70], authors have implemented a CR framework called Iris on Zynq SoC. Iris uses XML description to form a complete radio by linking the components together and run them on PS and PL. In this paper, a setup is an OFDM setup is evaluated for the Video transmission. A Zynq capable version of GNU Radio is presented in [71]. They have also demonstrated the feasibility and usability of FPGA-based SDR integrated with GNU Radio. In [72], Digital pre-distortion (DPD) required by 3G/4G base stations is implemented on Xilinx's Zynq All Programmable SoC. DPD is an advanced digital signal-processing technique that mitigates the effects of power amplifier (PA) nonlinearity in wireless transmitters. The flexible design flow of ZSoC facilitates the generation of effective DPD solutions for modern wideband and multi-antenna transmitters. A complete DPD feedback path on the Zynq SoC achieves up to 7x speed-up from hardware acceleration using this design flow. Recently, few works dealing with the design and implementation of OFDM-based LDACS transceivers have been proposed in [25, 26, 62–64, 73]. Hardware architecture of a novel synchronization method for LDACS in [62]. This method is designed to achieve synchronization accuracy and to be much robust to large CFO than the SoA method. Their implementation results show that the proposed synchronizer has reduced hardware usage and very low dynamic power consumption. In [73], the design of the LDACS transceiver via partial reconfiguration approach of the FPGA has been proposed. It offers significant improvement in the power consumption of the transceiver without compromising on performance. Authors in [25, 26] introduces reconfigurable low complexity filter and filter bank architectures for channelization and spectrum sensing applications on the receiver side. These architectures are based on the frequency response masking approach and allow the LDACS receiver to receive and/or sense single as well as multiple frequency bands simultaneously. In [64], partial reconfiguration capability of the FPGA is used to design a flexible LDACS transceiver.

From the architecture perspective, most of the LDACS transceivers are analyzed via simulations, and their performance analysis on fixed-point hardware in the presence of various RF impairments and wireless channels/interference has not been done yet. In this section, works done on various hardware platforms to analyze the performance of existing LDACS were reviewed. For the new-age applications, ZSoC is the most suitable platform to implement the transceivers in real-time. Few works dealing with the design and hardware implementation of OFDM-based LDACS transceivers are presented in [25, 26, 62, 73].

2.6 Summary

This chapter presents a brief review of the existing LDACS and its extensions, along with the LDACS PHY waveforms and digital filter design. We also discussed the various hardware platforms available for the LDACS prototype and existing LDACS testbeds.

In the next chapter, we discuss the proposed reconfigurable LDACS PHY framework and analyze its performance on USRP.

Chapter 3

Revised LDACS Protocol for LDACS-DME Coexistence

Exponential increase in global air traffic and demands to support heterogeneous services ranging from data to multimedia have compelled communication theorists and engineers to explore an alternative to existing very high frequency (VHF) band (118-137 MHz) based A2GC system. One possible alternative is to exploit multiple 1 MHz vacant frequency bands between incumbent distance measuring equipment (DME) signals in L-band (960-1164 MHz) and led to proposal of LDACS. An efficient utilization of such narrowband non-contiguous spectrum is challenging and hence, various activities to invent breakthrough technologies that provide higher spectral efficiency are being encouraged. Given the history of more than a century of wireless innovation, redesign of physical layer (PHY) is critical to improve the vacant spectrum utilization.

Success of OFDM in cellular and WiFi networks makes it the popular choice for LDACS PHY. However, initial research shows that OFDM based LDACS

PHY offers a fixed transmission bandwidth of only 498 kHz over 1 MHz spectrum resulting in less than 50% spectrum utilization. This is due to the high OOB emission and hence, interference to legacy DME signals. Furthermore, fixed transmission bandwidth limits its usefulness to support heterogeneous services demanding distinct bandwidths and dynamic control over PHY parameters such as OOB emission, transmission bandwidth etc.

This chapter presents the design of the proposed PHY frame structure /signals to support tunable bandwidth. The proposed frame structure maintains the complete compatibility with existing LDACS and offers transmission bandwidth from 186 kHz to 732 kHz compared to 498 kHz in existing LDACS. To support such frame structure, we develop a reconfigurable filtered OFDM (Ref-OFDM) based LDACS PHY and it is the second contribution of this thesis. The Ref-OFDM augments conventional OFDM with dynamic scheduler to support tunable bandwidth and reconfigurable linear phase fixed-coefficient multi-band finite impulse response (FIR) filter to enable on-the-fly control over transmission bandwidth. It also supports multi-band filtering for simultaneous transmission in multiple narrow frequency bands. In addition to the performance analysis using synthetic data, we demonstrate the functionality of the proposed Ref-OFDM PHY in real radio environment on universal software radio peripherals (USRPs) based testbed.

3.1 LDACS Deployment Environment

In this section, we discuss LDACS deployment environment which is useful for better understanding of the proposed work.

3.1.1 L-Band for A2GC

The spectrum occupancy of L-band is shown in Figure 1.3. Various legacy or incumbent users in L-band are DME signals (960-1215 MHz), joint tactical information distribution system (JTIDS), universal access transceiver systems (UAT at 978 MHz), secondary surveillance radar (SSR) at 1030 MHz and 1090 MHz [5]. The LDACS system can be deployed in the L band using two approaches: overlay and inlay approach. In overlay approach, it is deployed in the vacant spectrum where no other legacy system is present. This approach is easy and chosen for GSM like LDACS2 in 960-975 MHz vacant band. On the other hand, overlay approach is not suitable for OFDM based LDACS due to limited vacant spectrum in the L-band. Hence, an inlay approach is envisioned exploiting the multiple 1 MHz frequency bands between DME signals.

The DME is a transponder-based navigation system used to measure the slant range distance [17]. It is composed of Gaussian shaped pulse pairs. The time and frequency domain representations of the DME signal, shown in Figure 3.1 (a) and (b) respectively, can be evaluated as:

$$S(t) = e^{\frac{-\alpha t^2}{2}} + e^{\frac{-\alpha(t-\Delta t)^2}{2}} \tag{3.1}$$

$$S(f) = A\sqrt{\frac{8\pi}{\alpha}}e^{\frac{-2\pi^2 f^2}{\alpha}}e^{j\pi f\Delta t}cos(\pi f\Delta t) \tag{3.2}$$

where, α is pulse width of $4.5 \times 10^{-11}\ s^{-2}$, Δt represents the spacing of the pulses (=12 μs) and A is constant depending on the power of DME signal.

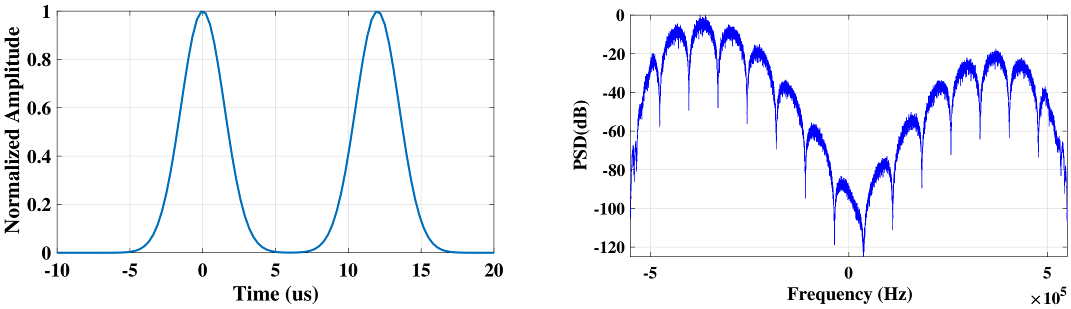

(a) (b)

Figure 3.1: Legacy L-band DME signal (a) Time domain response (b) Power spectral density.

Based on the existing spectrum allocation and occupancy measurements conducted worldwide, the identified spectrum for LDACS deployment are: 1) Forward link: 1110 - 1156 MHz and 2) Reverse link: 964 MHz - 1010 MHz. Due to stringent interference specifications of DME signals, the design of reconfigurable transceiver for improving the spectrum utilization of existing LDACS is a challenging task and aim of the work presented in this chapter.

3.1.2 Wireless Channel Models

For LDACS environment, three channels are modeled: Airport (APT), Terminal Maneuvering Area (TMA), En-routing (ENR). They are modeled as wide sense stationary uncorrelated scattering channels and characterized using three properties: fading, delay paths, and Doppler frequency [74].

The A2GC link encounters APT channel during the arrival and departure phases of the aircraft i.e. when the aircraft is on the ground and moving slowly. In this case, the line-of-sight (LOS) path is assumed to be blocked resulting in Rayleigh fading [8,74].

The TMA channel is modeled for the communication during the landing/take-off of the aircraft. Since the aircraft is at a low height, strongly scattered paths are observed in addition to LOS path. It experiences Rician fading with 10 dB Rician K factor which is the ratio of LOS component power to the power of scattered paths. For the worst case scenario, when the scatters from buildings are uniformly distributed, the Doppler spectrum follows Jakes distribution [8,74].

The ENR Channel is modeled for the communication during the flying mode. This channel typically consists of a strong path as well as other reflected and delayed paths. Therefore, the fading for this model is considered as Rician fading with the Rician k factor of 15 dB [8, 74]. It is higher than the TMA channel due to strong LOS path. The Doppler power spectrum of the reflected path follows a Gaussian distribution.

The channel parameters are given in Table 3.1. Note that the Doppler frequency is obtained as $F_D = F_c \frac{v}{c}$. Here, the F_c is the carrier frequency and is at most 1215 MHz, v is the velocity of the aircraft is m/s (1 Knots True Airspeed (KTAS)= 0.5144 m/s) and $c = 3 \times 10^8 m/s$.

scenario	**Max Delay (μs)**	**Acceleration ((m/s^2))**	**Harmonics**	**Velocity (KTAS)**	**Doppler Frequency (Hz)**
APT	3	5	8	200	$(1215e6)\frac{200\times.5144}{3e8}$ = 413
TMA	20	50	8	300	$(1215e6)\frac{300\times.5144}{3e8}$ = 624
ENR	15	50	25	600	$(1215e6)\frac{600\times.5144}{3e8}$ = 1250

Table 3.1: Channel parameters

3.2 Proposed Reconfigurable LDACS Protocol: Frame Structure

In this section, we present the frame structure of the proposed reconfigurable LDACS protocol that supports multiple transmission bandwidths. The requirements of the frame structure are:

- It should be identical to the existing LDACS frame structure when the transmission bandwidth is 498 kHz.
- The sub-carrier spacing should be fixed and equal to 9.76 kHz as it depends on the LDACS deployment environment and hence, can not be chosen arbitrarily.
- The number of symbols per frame should be fixed and independent of the transmission bandwidth.
- It is preferable to use identical synchronization and pilot symbol patterns as in existing LDACS protocol.

Based on an experimental study of channel conditions between aircraft and ground terminals at different phases of the flight, the sub-carrier bandwidth is limited to 9.76 kHz, and hence, the symbol duration is 120 μs [10, 15, 16]. For these specifications and to support different bandwidths ranging from 100 kHz to 1 MHz, the FFT size in the proposed protocol is chosen as 128 compared to 64 in the existing protocol. The proposed frame structure for the revised LDACS protocol depicting the data, pilot, and synchronization symbol patterns and their locations for 732 kHz transmission bandwidth is shown in Figure 3.2.

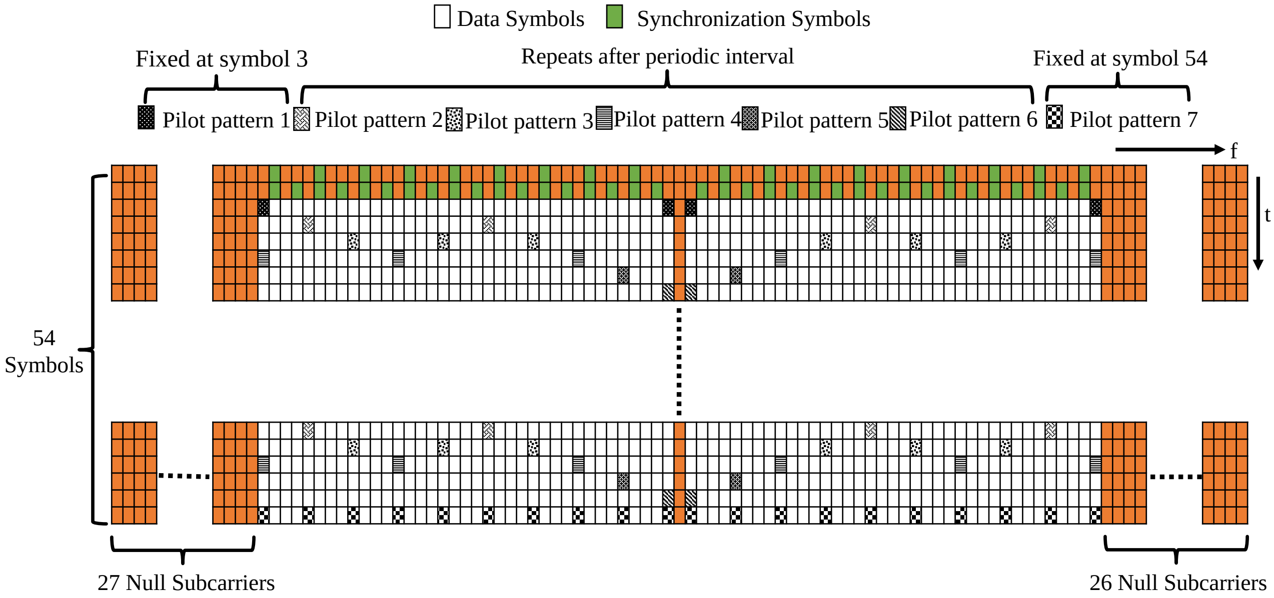

Figure 3.2: Proposed frame structure for the revised LDACS protocol depicting the data, pilot and synchronization symbol patterns and locations for 732 kHz transmission bandwidth.

The frame consists of 128 sub-carriers with the middle sub-carrier being the DC null sub-carrier. The first two symbols of each sub-carrier are reserved for synchronization. The frame comprises of at the most seven different pilot patterns which are critical for accurate channel estimation and equalization at the receiver. Similar to the existing protocol, we use fixed pilot patterns, pattern 1 ($P1$) and pattern 7 ($P7$), at the third and last symbols, respectively. Since four sub-carriers separate the pilot symbols in $P7$ on either side of the DC sub-carrier and the frequency resolution between adjacent sub-carrier is 9.76 kHz, the bandwidth can be incremented by 78 kHz only. Based on empirical observations, the bandwidth above 732 kHz is not feasible due to high interference to the DME signal. Also, the bandwidth below 186 kHz may not be suitable for the multi-carrier waveform. Thus, the proposed frame structure supports eight discrete bandwidths which are 732 kHz, 654 kHz, 576 kHz, 498 kHz, 420 kHz, 342 kHz, 264 kHz, and 186 kHz. For these bandwidths, the number of symbols should be fixed and multiple of the number of repeating pilot patterns, $P2-P6$. For instance, for 732 kHz-342 kHz, all five patterns ($P2 - P6$) are used while for the 264 kHz and 186 kHz bandwidth, the patterns used are $P2 - P5$ and $P2 - P4$, respectively. Hence, the number of symbols per frame is fixed to 54 out of which 2 are synchronization symbols, and 2 are pilot patterns, $P1$ and $P7$. The number of null-sub-carriers on each side depends on the transmission bandwidth as shown in Figure 3.3.

3.3 Theoretical Analysis of the Proposed Reconfigurable OFDM Based LDACS Protocol

In this section, we present the design and analysis of the proposed Ref-OFDM waveform based transceiver for the proposed frame structure as discussed in Section 3.3.

The motivation behind the proposed transceiver is to support various ser-

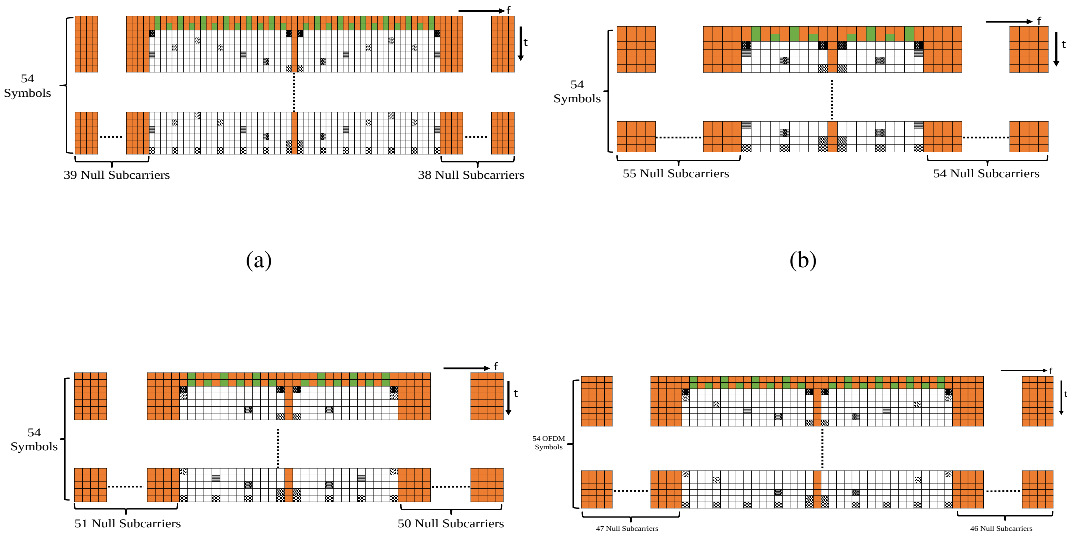

(a) (b)

(c) (d)

Figure 3.3: Proposed frame structure for the revised LDACS protocol depicting the data, pilot and synchronization symbol patterns and locations for the transmission bandwidth of (a) 498 kHz and (b) 186 kHz (c) 264 kHz (d) 342 kHz.

vices that demand distinct bandwidths. For example, consider the scenario in Figure 3.4 (a) where the existing LDACS can support at the most 498 kHz bandwidth due to the high out-of-band emission of OFDM. Similarly, it does not allow the multiple users to share the frequency band especially when transmitting over a narrow bandwidth as shown in Figure 3.4 (b).

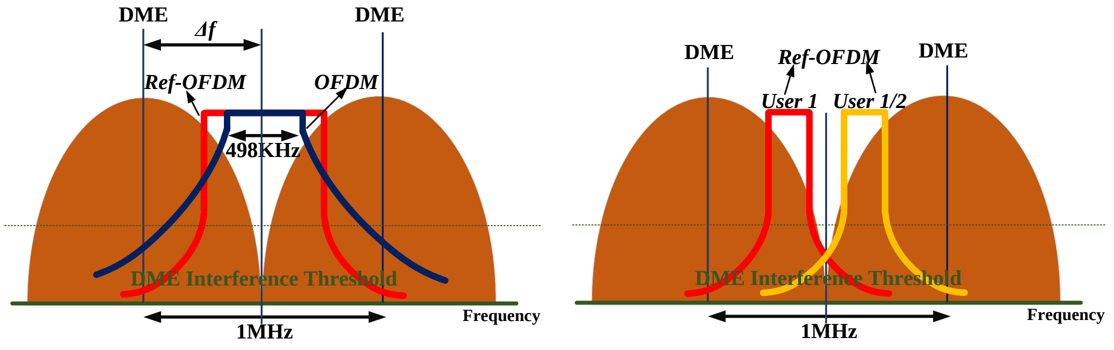

(a) (b)

Figure 3.4: (a) Single user, and (b) Multi-user LDACS deployment scenarios for a given DME interference threshold.

The proposed waveform aims to overcome these drawbacks. The requirements of the new waveform are:

- It should allow transceivers to adapt the transmission bandwidth over a wide range without compromising on the interference constraints of the incumbent L-band users (e.g., DME).
- The implementation complexity of the transmitter and receiver should be as low as possible.
- It should be compatible with existing OFDM based LDACS transceivers. Ideally, transceivers should be capable of dynamically switching between existing and new waveform on-the-fly.

To begin with, we present the design details of the transmitter along with the USRP setup followed by the receiver.

3.3.1 Ref-OFDM Transmitter

The block diagram of the Ref-OFDM transmitter is shown in Figure 3.5. As per the LDACS specifications, it consists of randomizer block which randomizes the input data to be transmitted by XORing with the LDACS randomizer stream. The data is then encoded via Reed Solomen (RS) and Convolutional (CC) encoder with the coding rate as 0.9 and 0.5, respectively. A helical block interleaver is used to minimize the probability of burst errors. The output of the interleaver is modulated by an appropriate modulation scheme such as QPSK, 16 QAM, and 64 QAM followed by the symbol to frame mapping for given transmission bandwidth. After conventional N point Inverse Fast Fourier Transform (IFFT) and Cyclic Prefix (CP) addition, the discrete time domain signal corresponding to the k^{th} sub-carrier can be given as,

$$x[n] = \frac{1}{K} \sum_{k=0}^{K-1} X_k e^{\frac{j2\pi kn}{K}} \tag{3.3}$$

where, K is the IFFT size, n is the discrete time index and X_k is frequency domain response of the transmitted signal at the k^{th} sub-carrier. It is given by

$$X_k = \sum_{n=0}^{K-1} x[n] e^{\frac{-j2\pi kn}{K}} \tag{3.4}$$

The $x[n]$ is then filtered using the proposed reconfigurable digital filter $f[n]$. Hence, the proposed waveform is referred to as Ref-OFDM waveform. The output of the filter $x'[n]$ is appropriately up-sampled and transmitted over the channel via analog front-end and antenna. The transmitted signal $x'[n]$ is the convolution ($*$) of $x[n]$ and the filter $f[n]$ and can be expressed as,

$$x'[n] = f[n] * x[n] \tag{3.5}$$

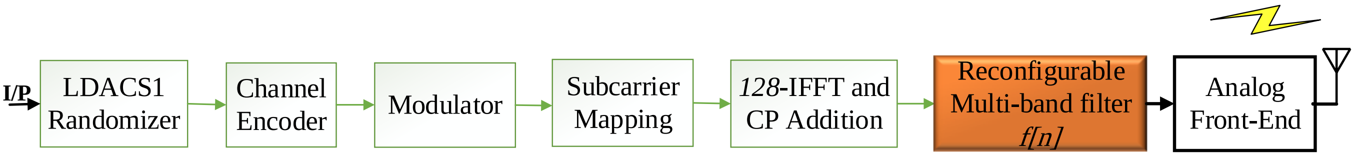

Figure 3.5: Block diagram of the Ref-OFDM based LDACS transmitter.

Next, we present the design details of the reconfigurable filter.

3.3.1.1 Filter Design for Single Band Transmission

For the proposed LDACS specifications discussed in Section 3.3, we need a filter which can support eight different bandwidths. One way to design such a filter is the Velcro approach where eight distinct filters are stacked in parallel [75]. Such approach incurs vast area and power complexity and still offers limited flexibility. In a programmable filter, filter coefficients corresponding to different frequency responses are stored in the memory and retrieved when required [76]. Though less complicated than Velcro approach, reconfiguration time of the programmable filters is high, and it can not take advantage of the methods which significantly reduce the complexity of fixed coefficient filter by replacing the computationally intensive coefficient multiplication operation with the hardware-friendly shift and add operations.

The proposed reconfigurable fixed coefficient filter offers variable bandwidth baseband bandpass responses and is based on the coefficient decimation method (CDM) and its extensions [45,77]. To begin with, we discuss CDM using a suitable example. Consider the prototype baseband bandpass filter, $F(e^{j\omega_c})$, where $2\omega_c$ is the bandwidth of the filter. The prototype filter is designed of length L_f. The filter coefficients are obtained using Parks-McClellan optimal FIR filter design method and the filter response for $\omega_c = 0.12\pi$ is shown in the Figure 3.6(a). Note that all frequency specifications in this subsection are normalized for half the sampling frequency. The CDM can provide the frequency responses with the bandwidth integral multiple of the original bandwidth, $2\omega_c$ using fixed-coefficient prototype filter. Let us consider this integer factor as $D \in \{1, 2, 3..\}$. In CDM with factor D, every D^{th} coefficient of the prototype filter is kept unchanged and remaining coefficients are truncated to zero [45]. This results in the multi-band frequency response, $F^{cdm}(e^{j\omega_c})$, which is given as

$$F^{cdm}(e^{j\omega_c}) = \frac{1}{D}\sum_{i=0}^{D-1} F(e^{j(\omega_c - \frac{2\pi i}{D})}) \tag{3.6}$$

Next, every D^{th} coefficient of the filter is grouped by removing the zero-valued coefficients to obtain the baseband bandpass response with the bandwidth $2D\omega_c$. For example, the frequency responses obtained using the prototype filter in Figure 3.6(a) and the CDM with $D = 2$ and $D = 6$ are shown in Figure 3.6(b). Note that, the filter coefficients are fixed and independent of D. However, the transition bandwidth and stop-band attenuation deteriorate by factor D. One way to overcome this deterioration is to over-design the prototype filter with higher order. An extension of CDM referred to as modified CDM (MCDM) [77], offers decimated bandpass response with large bandwidth using a smaller value of D than that required in the CDM. In MCDM, all coefficients except every D^{th} coefficient of the prototype filter, $F(e^{j\omega_c})$ are discarded followed by sign reversal of every alternate retained coefficient. The filter response is then given by

$$F^{mcdm}(e^{j\omega_c}) = \frac{1}{D}\sum_{i=0}^{D-1} F(e^{j(\omega_c - \frac{\pi(2i+1)}{D})}) \tag{3.7}$$

For instance, MCDM [77] with factor D results in a bandstop response and the corresponding bandpass response, with bandwidth $1 - D\omega_c$, can be obtained by subtracting it from an appropriately delayed version of the input signal. For example, the MCDM with $D = 2$, offers the bandpass response with the bandwidth of 0.76π as shown in Figure 3.6(c). It has narrower transition bandwidth and better stopband attenuation than the bandpass response with bandwidth 0.72π obtained using the CDM in Figure 3.6(b).

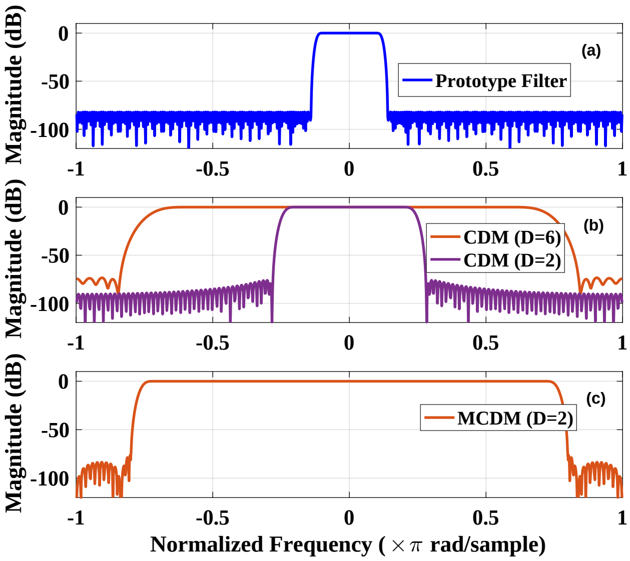

Figure 3.6: Reconfigurable filter design using CDM and MCDM. (a) Prototype baseband bandpass filter with $\omega_c = 0.12\pi$ (b) Baseband bandpass filter responses with the bandwidth 0.24π and 0.72π obtained using the CDM approach with $D = 2$ and $D = 6$, respectively, (c) Baseband bandpass filter responses with the bandwidth 0.76π obtained using the MCDM with $D = 2$.

The proposed filter is designed using a combination of CDM and MCDM. For easier understanding, we mention normalized bandwidths corresponding to actual transmission bandwidths in Table 3.2. The maximum input frequency is 1.25 MHz (=128 * 9.76 kHz) which corresponds to the sampling frequency of 2.5 MHz. For the desired values of bandwidths, we obtain the bandwidth of the prototype filter as 0.24π (i.e., $\omega_c = 0.12\pi$) and range of D as $\{2, 3, 4, 5, 6, 7\}$ via dynamic programming. For instance, the MCDM with $D = 7$ and prototype filter with $\omega_c = 0.12\pi$ give bandpass response with bandwidth 0.32π (i.e., $\omega_{cd} = 0.16\pi$). Since the CDM and MCDM result in deterioration of the filter response, the prototype filter needs to be over-designed such that the passband ripple, stopband attenuation and transition bandwidth of the prototype filter are $D_{max}(= 7)$ times better than the respective desired values of these parameters. Based on these parameters, order and coefficients of the prototype filter are obtained. For example, for the desired stop-band attenuation, pass-band ripple and transition bandwidth of 70 dB, 0.1 dB and 0.1π, respectively, the prototype filter order is 240 and bandwidth is 0.24π, i.e., $\omega_c = 0.12\pi$. Please refer to Table 3.2 for mapping between the desired bandwidth and corresponding D. The baseband bandpass responses for these bandwidths are shown in Figure 3.7.

Bandwidth (kHz)	Desired cut-off frequency (ω_{cd})	Decimation Factor (D)	Filter Method
186	0.16 π	7	MCDM
264	0.22 π	2	CDM
342	0.28 π	6	MCDM
420	0.34 π	3	CDM
498	0.40 π	5	MCDM
576	0.46 π	4	CDM
654	0.52 π	4	MCDM
732	0.58 π	5	CDM

Table 3.2: Reconfigurable filter design

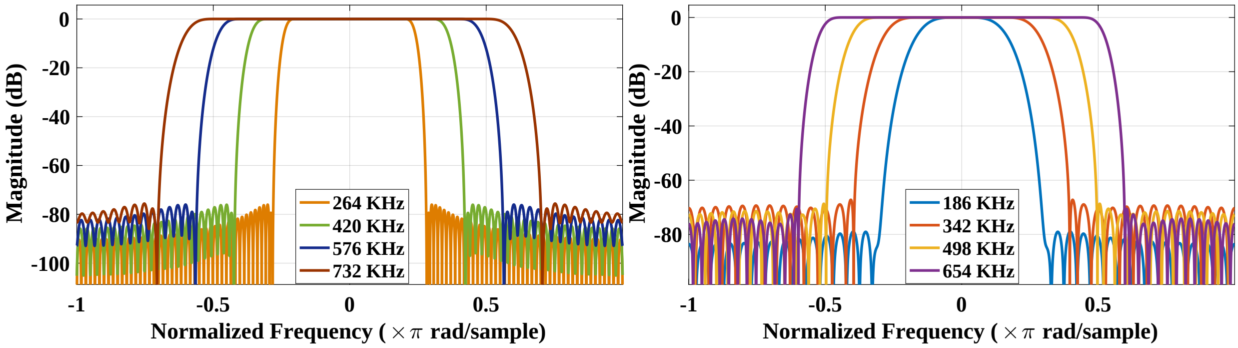

(a) (b)

Figure 3.7: Variable baseband bandpass frequency responses obtained using fixed-coefficient baseband bandpass prototype filter with $\omega_c = 0.12\pi$ and, (a) CDM , and (b) MCDM approach.

3.3.1.2 Filter Design for Simultaneous Transmission in Multiple Bands

In this subsection, we extend the above reconfigurable filter for the case where user simultaneously transmits in the multiple bands as shown in Figure 3.4 (b). It is possible only when the filter provides multi-band frequency response with no image on the other side of the DC frequency. Though CDM offers multi-band responses, the response is symmetrical with respect to the DC frequency for real prototype filter. In case of complex prototype filter (i.e., the prototype filter with complex-valued coefficients), the CDM cannot offer variable bandwidth responses for a given center frequency. To obtain an asymmetrical frequency response with variable bandwidth and center frequency, we use conventional modulation based discrete Fourier Transform (DFT) filter bank (DFTFB) approach [78]. In DFTFB, the prototype filter is realized in the polyphase form, and the resultant filter response is modulated using the DFT to obtain bandpass responses at the regular interval between -1 and 1 with no image on the other side of the DC frequency. For example, the DFTFB of order 4 needs 4-point DFT and offers four bandpass responses at the center frequencies of -1 π, -0.5π,

0π and 0.5π (rad/sample). Note that the bandwidth of all responses is same and equal to the bandwidth of the prototype filter. To obtain the control over the bandwidth, we replace the prototype filter of the DFTFB with the reconfigurable filter discussed in the previous subsection. Thus, the bandwidth of all the sub-bands is the same and can be tuned to one of the eight supported bandwidths on-the-fly. The control over the center frequency of the bandpass responses can be obtained by choosing the appropriate order of the DFT. For example, the DFTFB of order K offers K bandpass responses located uniformly between -1 and 1 at an interval of $2/K$ on the normalized frequency scale.

3.3.1.3 Filter Architecture

The architecture of a K- band reconfigurable filter is shown in Figure 3.8. It consists of N^{th} order prototype filter with real and fixed valued coefficients as $\{f_0, f_1, ..f_N\}$. It is implemented in the polyphase form with K parallel branches. The sum of the output of all the polyphase branches provides the baseband bandpass response. The output of the polyphase filter is given to the K-point DFT as shown in Figure 3.8 to obtain the multi-band response. Each adder in the conventional FIR filter is replaced with coefficient decimation (CD) block to obtain the bandpass response with variable bandwidth. The CD block either bypass the new coefficient, f_C or perform addition operation in case of CDM. In the case of MCDM, CD block needs to perform subtraction operation for alternate retained coefficients. The select signals are used to perform the desired operation on each of the coefficients. The output logic unit is used to obtain the bandpass response by subtracting the bandstop response obtained from the prototype filter and MCDM from the appropriately delayed version of the input signal.

3.3.2 Receiver

The signal at the input of receiver, $r[n]$, consists of three components: 1) The transmitted signal after passed through the channel with impulse response $h^L[n]$, 2) DME interference signal after passed through the wireless channel with impulse response $h^D[n]$, and 3) Zero-mean additive white Gaussian noise $\tilde{n}_0[n]$. The $r[n]$ is given as,

$$r[n] = h^L[n] * x'[n] + h^D[n] * s[n] + \tilde{n}_0[n] \tag{3.8}$$

In LDACS environment, both channels $h^L[n]$ and $h^D[n]$ assumed to have

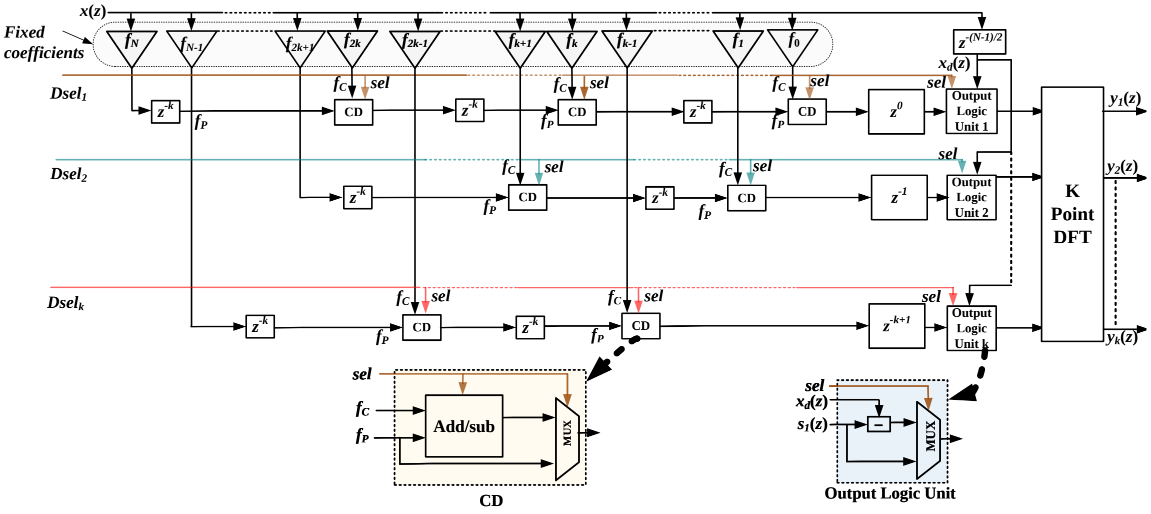

Figure 3.8: Architecture of the proposed reconfigurable K-band filter.

identical statistics such that

$$h^L[n] = \sum_{l=1}^{L} h_l^L \delta[n-l] \; and \; h^D[n] = \sum_{l=1}^{L} h_l^D \delta[n-l] \tag{3.9}$$

Where L is the total number of channel taps, h_l^L and h_l^D are the impulse responses of the channel faced by LDACS and DME signal of the l^th path, respectively. The channels are assumed to be time-invariant for each transmitted OFDM symbol.

The receiver performs all the functions similar to the transmitter in the reverse order as shown in the Figure 3.9.

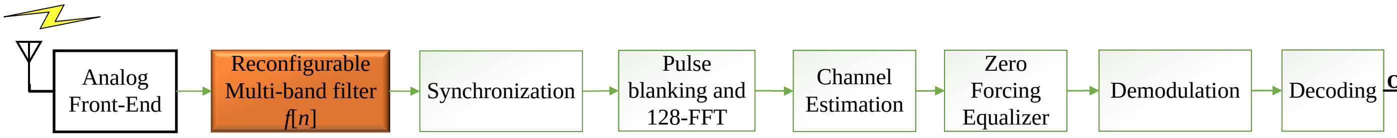

Figure 3.9: Block diagram of Ref-OFDM based LDACS receiver.

In the beginning, the received digitized baseband signal is filtered using the same reconfigurable filter $f[n]$ which is the same as the transmitter. The filtered received signal is given by

$$r'[n] = f[n] * h^L[n] * f[n] * x[n] + f[n] * h^D[n] * s[n] + f[n] * \tilde{n}_0[n] \tag{3.10}$$

The filtered signal is then passed through the synchronization block to estimate time and frequency offsets. The coarse synchronization is based on correlation of synchronization symbols at the beginning of the forward link frame, and fine synchronization is based on correlation of cyclic prefix of each OFDM symbol. Pulse Blanking technique used to remove the non-linearities and interference. After FFT, channel coefficients and impulse response are estimated using pilots followed by channel equalization via zero forcing approach. In the end, the symbols are demodulated and decoded to obtain the transmitted data. The received signal R_k at k^{th} subcarrier is as follows:

$$R'_k = F_k H_k F_k X_k + F_k H_{d_k} S_k + F_k \tilde{N}_0 k \tag{3.11}$$

where, H_k , H_{d_k} are the LDACS and DME channel frequency responses at the k^{th} subcarrier respectively can be given as

$$H_k = \sum_{l=1}^{L} h_l^L e^{\frac{-j2\pi kl}{N}} \; and \; H_{d_k} = \sum_{l=1}^{L} h_l^D e^{\frac{-j2\pi kl}{N}} \tag{3.12}$$

Next, we obtain the frequency response of the filter $f[n]$ at the k^{th} subcarrier F_k. Here, the length of the filter, $f[n]$, is $\left\lceil \frac{(L_f+1)}{D} \right\rceil$ and it is always less than the FFT size, K. Thus, the impulse response of the filter is zero padded by $\left(K - \left\lceil \frac{L_f+1)}{D} \right\rceil\right)$ to have the filter length same as FFT length. Then, we obtain F_k by taking K-point FFT of the zero padded filter impulse response where

$$F_k = W^H . \left[f[n], \mathbf{0}_{1\times\left(K - \left\lceil \frac{(L_f+1)}{D} \right\rceil\right)} \right] \tag{3.13}$$

Here, W is the K-point FFT matrix.

In the proposed reconfigurable filter, prototype filter coefficients are fixed, and various responses are obtained using CDM and MCDM approaches. The impulse response of the proposed filter $f[n]$ with CDM factor D is given by

$$f[n] = f^P[n].b[n] \tag{3.14}$$

where, $f^P[n]$ be the impulse response of the prototype filter and $b[n]$ can be given as

$$b[n] = \begin{cases} 1 \;\; \forall\, n = mD; \; m = 0, 1, 2... \\ 0 \qquad\qquad \text{otherwise} \end{cases} \tag{3.15}$$

The function $b[n]$ is periodic with period M, and hence the Fourier series expansion is given by

$$b[n] = \frac{1}{D} \sum_{i=0}^{D-1} B(i) e^{\frac{j2\pi in}{D}} \tag{3.16}$$

where $B(i)$ are complex-valued Fourier series coefficients defined by,

$$B(i) = \sum_{n=0}^{D-1} b[n] e^{\frac{-j2\pi in}{D}} \tag{3.17}$$

By substituting the Eq. (3.15) into (3.17) we will get,

$$B(i) = \begin{cases} 1 \qquad \forall\, k \\ 0 \;\; \text{otherwise} \end{cases} \tag{3.18}$$

Hence, from Eq. (3.18) and . (3.16), $b[n]$ can be expressed as,

$$b[n] = \frac{1}{D} \sum_{i=0}^{D-1} e^{\frac{j2\pi in}{D}} \tag{3.19}$$

By substituting Eq. (3.19) into Eq. (3.14), we compute $f[n]$. Similar approach can be used for MCDM. Next, we will analyze the BER performance of the

Ref-OFDM based LDACS system for the received filtered signal represented by Eq. (3.11).

3.3.3 BER Analysis

To take the noise effects in calculation of the BER analysis, an additive white Gaussian noise is added. The signal to interference plus noise ratio is the ratio of signal power and the sum of interference and noise power. For the received signal in Eq. (3.11), the SINR for k^{th} subcarrier is given as

$$SINR(k) = \frac{{F_k}^4 \lambda_k P}{{F_k}^2 P_{\tilde{N_0}} + {F_k}^2 \lambda_{d_k} P_{DME}} \tag{3.20}$$

By rewriting the equation (3.20) we get,

$$SINR(k) = \frac{{F_k}^2 \lambda_k P}{P_{\tilde{N_0}} + \lambda_{d_k} P_{DME}} \tag{3.21}$$

where, P is the transmitted signal power, $P_{\tilde{N_0}}$ is the gaussian noise power, F_k is given by Eq. (3.13) and $\lambda_k = |H_k|^2$, $\lambda_{d_k} = |H_{d_k}|^2$ are the power associated with the channel frequency responses $|H_k|$ and $|H_{d_k}|$ respectively and can be acquired using (3.12),

$$\lambda_k = \left| \sum_{l=1}^{L} h_l^L e^{\frac{-j2\pi kl}{N}} \right|^2 \; and \; \lambda_{d_k} = \left| \sum_{l=1}^{L} h_l^D e^{\frac{-j2\pi kl}{N}} \right|^2 \tag{3.22}$$

Here, we are considering that the multipath channel is modelled as the Rayleigh fading channel whose probability density function can be represented as

$$p_\lambda(\lambda) = \frac{1}{\bar{\lambda}} e^{\frac{-\lambda}{\bar{\lambda}}} \tag{3.23}$$

where, $\bar{\lambda}$ is the mean of the variable λ and is equal to variance of H_k. The DME channel λ_{d_k} also follows the same exponential distribution as it is assumed to have the same distribution as the LDACS channel.

Next, we obtain the expression for DME interference power, P_{DME}. The DME is a transponder-based navigation system used to measure the slant range distance [17]. It is composed of Gaussian shaped pulse pairs. The time and frequency domain representations of the DME signal is given by Eq. (5.1) and Eq. (5.2) respectively.

$$s(t) = e^{\frac{-\alpha t^2}{2}} + e^{\frac{-\alpha (t-\Delta t)^2}{2}} \tag{3.24}$$

$$S(f) = A\sqrt{\frac{8\pi}{\alpha}} e^{\frac{-2\pi^2 f^2}{\alpha}} e^{j\pi f \Delta t} cos(\pi f \Delta t) \tag{3.25}$$

where, α is pulse width of $4.5*10^{-11}\ s^{-2}$, Δt represents the spacing of the pulses (=12 μs) and A is constant depending on the power of DME signal. Then, we have

$$P_{DME} = \int_{f_1}^{f_2} |S(f)|^2 df \tag{3.26}$$

Substituting Eq. (5.2) substituting $cos(\theta) = \frac{e^{j\theta}+e^{-j\theta}}{2}$ in Eq. (3.27), we get

$$P_{DME} = A^2 \left(\frac{8\pi}{\alpha}\right) \int_{f_1}^{f_2} \left|e^{\frac{-2\pi^2 f^2}{\alpha}}\right|^2 \left|e^{j2\pi f\Delta t}\right|^2 \times \left|\frac{e^{j\pi f\Delta t} + e^{-j\pi f\Delta t}}{2}\right|^2 df \quad (3.27)$$

Using the Euler formula, $|e^{j\theta}|^2 = 1$ and assuming, $C_1 = \frac{4\pi^2}{\alpha}$ and $C_2 = j2\pi\Delta t$, we have

$$P_{DME} = A^2 \left(\frac{8\pi}{\alpha}\right) \left[2\int_{f1}^{f2} e^{-C_1 f^2} df + \int_{f1}^{f2} e^{-C_1 f^2 + C_2 f} df + \int_{f1}^{f2} e^{-C_1 f^2 - C_2 f} df\right] \quad (3.28)$$

After further algebraic simplification, we get

$$\begin{aligned} P_{DME} =& A^2 \left(\frac{8\pi}{\alpha}\right) \sqrt{\frac{\pi}{C_1}} \left[\left\{(erf(\sqrt{C_1} f_2) - erf(\sqrt{C_1} f_1))\right\}\right. \\ &+ \frac{1}{2}\left\{e^{\frac{C_2^2}{4C_1}}(erf(\frac{2C_1 f_2 - C_2}{2\sqrt{C_1}}) - erf(\frac{2C_1 f_1 - C_2}{2\sqrt{C_1}})\right\} \\ &+ \left.\frac{1}{2}\left\{e^{\frac{C_2^2}{4C_1}}(erf(\frac{2C_1 f_2 + C_2}{2\sqrt{C_1}}) - erf(\frac{2C_1 f_1 + C_2}{2\sqrt{C_1}})\right\}\right] \end{aligned} \quad (3.29)$$

Using Eq. (3.21), the BER of the k^{th} received symbol for M-QAM can be expressed as,

$$P_{e_{MQAM}}^{\lambda,\lambda_d}(k) \cong \frac{4}{log_2 M}\left(1 - \frac{1}{\sqrt{M}}\right) \sum_{i=1}^{\sqrt{M}/2} Q(2i-1) \times \sqrt{\frac{3log_2 M F_k^2 \lambda_k P}{(M-1)\left(P_{\tilde{N}_0} + \lambda_{d_k} P_{DME}\right)}} \quad (3.30)$$

where erf(.) is a error function [79]. Therefore, BER averaged across the fading channel can be expressed as,

$$P_{e_{MQAM}}(k) = E[P^{\lambda,\lambda_d}_{e_{MQAM}}(k)] \cong \int_0^{\infty}\int_0^{\infty} P^{\lambda_1,\lambda_2}_{e_{MQAM}}(k) \times p_{\lambda}(\lambda)d\lambda \, p_{\lambda_d}(\lambda_d)d\lambda_d$$

The average BER across all the subcarriers is given by

$$P_{e_{MQAM}} = \frac{1}{K}\sum_{k=0}^{K-1} P_{e_{MQAM}}(k) \tag{3.31}$$

The analytical expression in Eq. (3.31) can be evaluated by numerical methods. This completes the BER analysis of the proposed Ref-OFDM based LDACS in presence of the DME interference and multipath Rayleigh fading channel. Furthermore, the size of the DFT can be changed on-the-fly as per the desired center frequency of the transmission. Such flexibility is not possible in case of OFDM, FBMC and GFDM based LDACS. In addition, Ref-OFDM can be easily extended to a multi-antenna system, unlike FBMC based LDACS. Also, the Ref-OFDM and FBMC waveforms have much better-localized frequency spectrum than OFDM because of the sub-band filtering.

Here, we also present the Ref-OFDM based LDACS transceiver testbed setup using USRPs to analyze the performance in real time.

3.4 Testbed of the Proposed Ref-OFDM Based LDACS Transceiver

In this section, we present the experimental testbed using Universal Software Radio Peripheral (USRP) for the deployment of the LDACS. USRP is a tunable transceiver from NI and is widely used for prototyping wireless communication systems.

The Proposed testbed consists of three National Instrument (NI) USRP-2922 and VERT900 antennas as shown in Figure 3.10. One USRP is used for DME transmission as well as reception while other two USRPs are used as LDACS transmitter and receiver, respectively. Several baseband signal processing blocks of the transceiver are realized using the LabView environment from NI. The whole setup is configured for the parameters mentioned in Table 3.3

Parameters	Transmitter	Receiver
Carrier Frequency	985 MHz	985 MHz
IQ Sampling Rate	1 MHz	1 MHz
LDACS antenna gain	2dB	2dB
DME antenna gain	2dB/10dB	-
Acquisition Duration	NA	1s

Table 3.3: Parameters of transmitter and receiver USRP

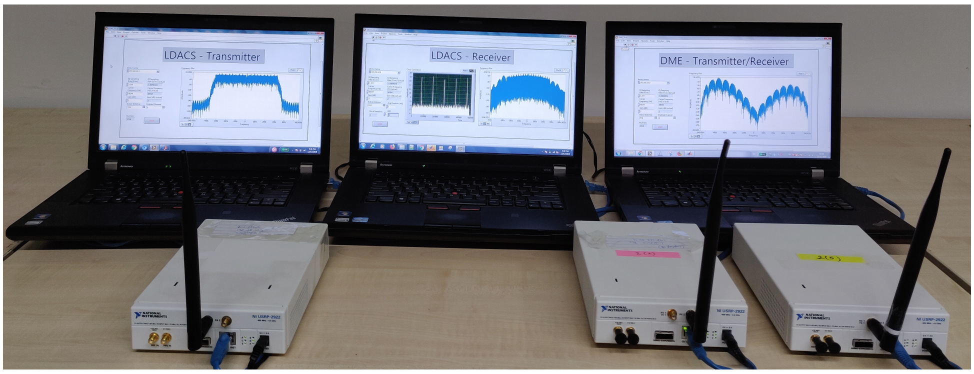

Figure 3.10: USRP based testbed for LDACS.

3.4.1 LDACS Transmitter

To implement the inlay approach of deployment, the proposed Ref-OFDM based LDACS signal is transmitted at the carrier frequency of 985 MHz with the IQ sampling rate of 1 MHz. The transmission has been performed for the variable bandwidths ranging from 186-732 kHz using 128 points IFFT with 9.76 kHz sub-carrier spacing.

The LDACS transmitter realization is shown in Figure 3.11, consists of three subsystems: (a) the first subsystem sets the transmission parameters such as carrier frequency, antenna gain, IQ sampling rate, and transmission antenna port, (b) the second subsystem is the LDACS transmitter which first generates the random bits and then modulates them by selecting an appropriate modulation scheme. The “OFDM Block.vi ” performs all the LDACS transmitter operations as discussed in subsection 3.3.1. The synchronization symbols are added to the LDACS frame for the synchronization at the receiver followed by the filtering operation subsection 3.3.1.1 performed using the “Reconfigurable Multiband Filter.vi ”, (c) The Third subsystem continuously transmits the filtered data over the desired carrier frequency via LDACS USRP transmitter.

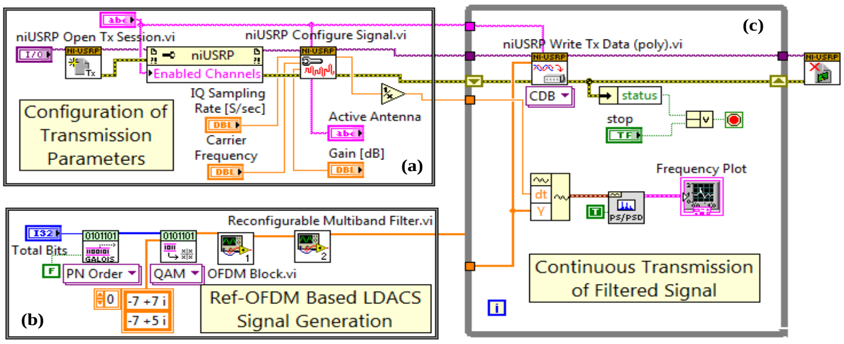

Figure 3.11: Implementation of Ref-OFDM based LDACS transmitter in the LabView environment.

3.4.2 DME Transmitter

Similar to the LDACS transmitter, the DME transmitter model as shown in Fig 3.12 comprises three sub-blocks (a) the first sub-block configures the USRP parameters as mentioned in the Table 3.3 for the DME transmission, (b) the second sub-block is dedicated for the DME signal generation. This includes two

Gaussian monopulse generator blocks which generate the Gaussian pulses with the center frequencies of 984.5 MHz and 985.5 MHz. These monopulses are later combined to achieve the DME signal of Gaussian pulse pair, and at every transmission, it transmits 2700 pulse pairs per second, (c) the last sub-block is realized to continuously transmit the DME signal over the air.

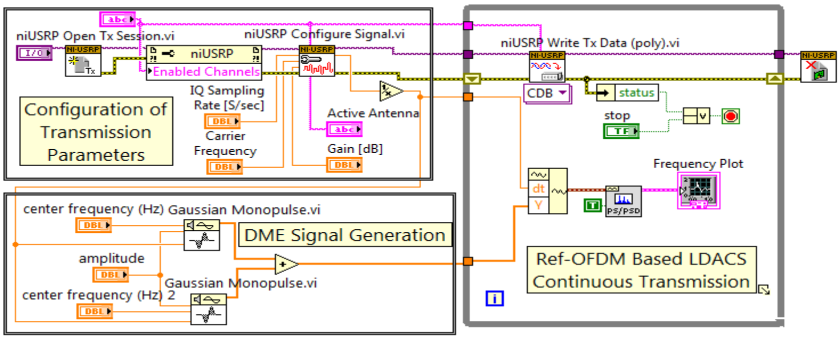

Figure 3.12: Implementation of DME transmitter in the LabView environment.

3.4.3 LDACS Receiver

The LDACS signal is then received by the LDACS receiver USRP, tuned at 985 MHz to receive the transmitted signal at IQ sampling rate of 1 MHz. However, due to a mismatch between the oscillator frequency at the transmitter and receiver USRPs, additional synchronization is needed at the receiver (see details in Figure 3.13). In this work, to identify the beginning of each frame, the received signal is frame synchronized by determining the cross-correlation between the received signal and the known synchronization symbols added in the LDACS frame at the transmitter. The signal is then processed from the maximum correlated value index. The proposed Ref-OFDM uses a matched reconfigurable filter at the receiver followed by fine synchronization to estimate time and frequency offsets. The fine synchronization is based on the correlation of cyclic prefix of each OFDM symbol. After that, the channel is estimated using pilots followed by channel equalization via zero forcing method. In the end, the symbols are demodulated and decoded for subsequent performance analysis. More detailed description about LDACS receiver is provided in subsection 3.3.2.

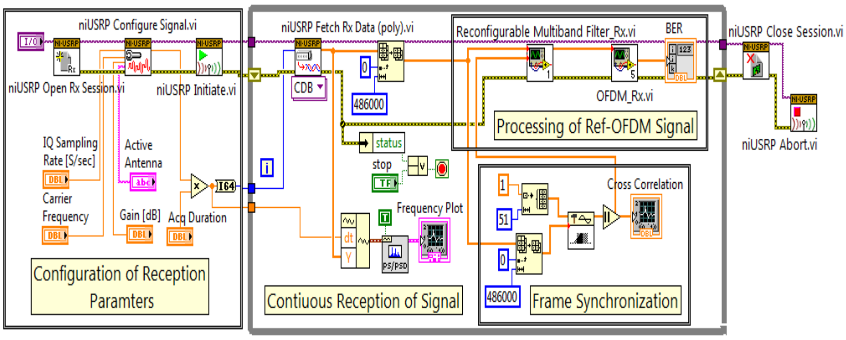

Figure 3.13: Implementation of Ref-OFDM based LDACS receiver in the LabView environment.

Next, we present the performance analysis of various waveforms via simulation and experimental results.

3.5 Performance Analysis via Simulation and Experimental Results

In this section, we discuss the simulation and hardware experimental results to compare the performance of the proposed Ref-OFDM based LDACS protocol with the existing protocol and FBMC based LDACS in [12] in realistic LDACS environment.

3.5.1 Simulation Results

Here, we present extensive simulation results to compare various waveforms in terms of PSD, BER, and complexity. Note that we consider the revised OFDM based LDACS which employs time domain windowing at the transmitter to improve the out-of-band attenuation. In addition, we also consider the LDACS protocol using GFDM waveform which has not been studied in the literature yet. The results include the comparison of these variants with respect to their out-of-band emission using the power spectral density (PSD) plots for various bandwidths, interference at the adjacent DME signal for these bandwidths, BER in the presence of DME interference, and implementation complexity. The simulation parameters are chosen as per the LDACS specifications and are given in Table 3.4.

Parameters	Value
Total Bandwidth	1.25MHz
Transmitted Bandwidth	Any of the supported bandwidths
Length of FFT	128
Used sub-carriers	18-74
Sub-carrier spacing	9.76kHz
Total Symbol duration	120μs
Modulation	QPSK
Channel	ENR, APT, TMA
CC encoder rate	0.5
RS encoder rate	0.9
Constraint lengths	4,7,9

Table 3.4: Simulation parameters

For LDACS environment, three channels are modeled: Airport (APT), Terminal Manoeuvring Area (TMA), En-routing (ENR). They are modeled as wide sense stationary uncorrelated scattering channels and characterized using three properties: fading, delay paths, and Doppler frequency [74].

The channel parameters are given in Table 3.5 [8, 10, 74, 80]. Note that the Doppler frequency is obtained as $F_D = F_c \times \frac{v}{c}$ where F_c is the carrier frequency and is at most 1215 MHz, v is the velocity of the aircraft in m/s (1 Knots True

Airspeed (KTAS)= 0.5144 m/s) and $c = 299792458 m/s$.

Scenario	Fading	Max Delay (μs)	Acceleration (m/s^2)	Velocity (KTAS)	Doppler Frequency (Hz)
APT	Rayleigh	3	5	200	$(1215e6) \times \frac{200 \times .5144}{299792458}$ = 413
TMA	Rician	20	50	300	$(1215e6) \times \frac{300 \times .5144}{299792458}$ = 624
ENR	Rician	15	50	600	$(1215e6) \times \frac{600 \times .5144}{299792458}$ = 1250

Table 3.5: Channel parameters

3.5.1.1 Single Band Transmission

To begin with, we consider single user transmitting in the frequency band between adjacent DME signals. For illustration, we consider two bandwidths, 1) 732 kHz which incurs maximum interference to the DME, and 2) 498 kHz which is maximum bandwidth allowed in existing OFDM based LDACS. The corresponding PSD plots of LDACS signal after transmission over the ENR channel are shown in Figure 4.16. For clarity of the plots, we are only showing the main lobes of the DME signals. It can be observed that the interference at the DME signal is quite high in case of OFDM and GFDM based LDACS (For actual values, please refer to discussion related to Table 3.6 at the end of this subsection). The proposed Ref-OFDM and FBMC based LDACS can achieve the transmission bandwidths of up to 732 kHz due to high out-of-band attenuation leading to 50% improvement in spectrum utilization. The PSD plots corresponding to the other two channels are not shown to avoid repetitive plots. However, we have considered them for BER analysis.

Next, we compare the BER of these waveforms for three different channel conditions in the presence of DME interference only. We do not include BER

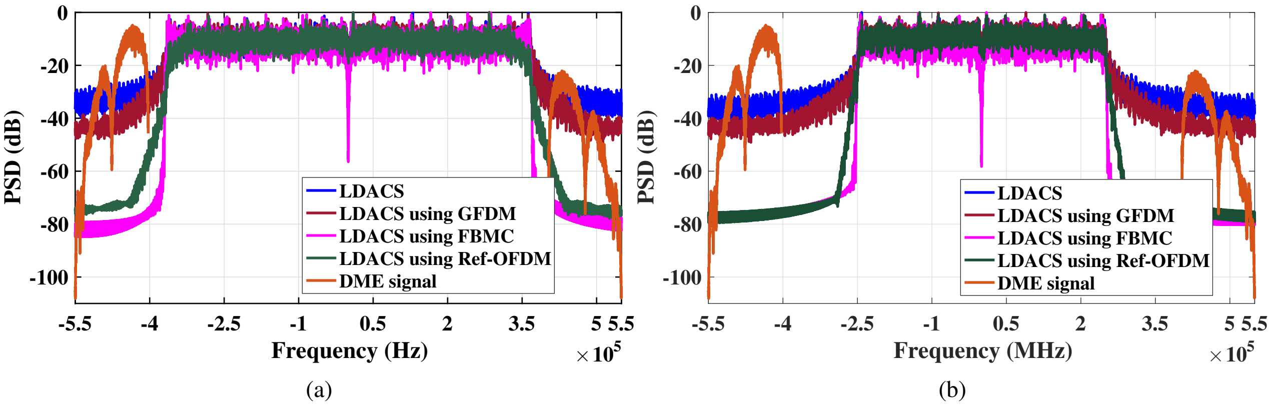

Figure 3.14: The PSD comparison of various waveforms for ENR channel and two different transmission bandwidths, (a) 732kHz, and (b) 498kHz.

plots for FBMC as they are overlapping with OFDM BER plots. We again consider 732 kHz, and 498 kHz bandwidth and corresponding plots are shown in Figure 5.6 (a) and (b) respectively. It can be observed that Ref-OFDM has better BER performance in both the cases. The Figure 5.6 (b) shows that for higher transmission bandwidth OFDM and GFDM has very bad ber performance while Ref-OFDM performs much better than other two as there is less DME interference in case of Ref-OFDM. As expected, the performance is better in case of ENR channel due to strong LOS path. The PSD and BER plots show that the Ref-OFDM has better out-of-band attenuation than OFDM and GFDM without compromising on the BER performance.

Next, we compare the BER of these waveforms in the presence of DME interference for ENR channel. Here, we consider the transmission bandwidth of 342 kHz and three center frequency with a deviation of 0, 100 and 400 kHz from the baseband. As shown in Figure 3.16, the BER of the proposed Ref-OFDM is significantly better than existing LDACS for all the center frequencies considered here. The proposed Ref-OFDM based LDACS exhibited SNR saving in

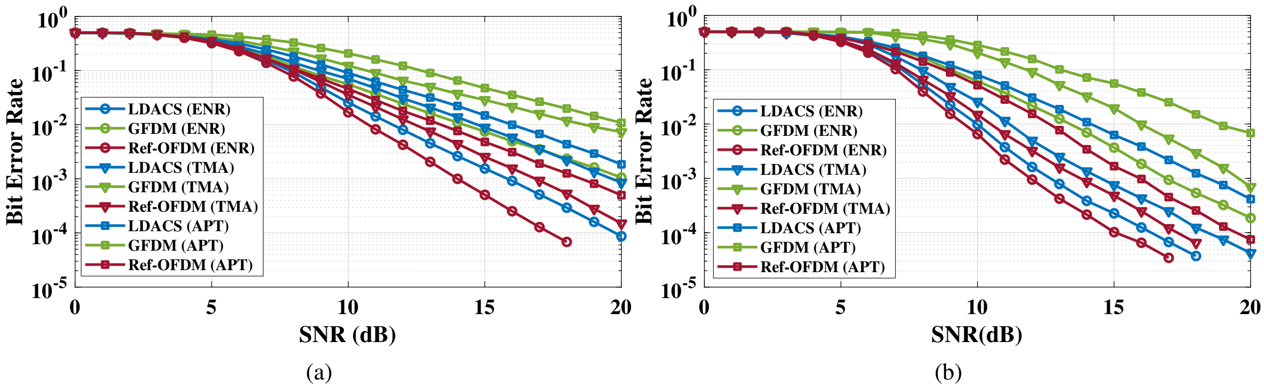

(a) (b)

Figure 3.15: The BER comparison of various waveforms for two different transmission bandwidths, (a) 732kHz, and (b) 498kHz and three different channels.

the range of 1 to 1.5 dB at a bit error rate of 10^{-2}. We also observed that the difference between the BER performance of the Ref-OFDM and OFDM increases with the increase in the transmission bandwidth. The BER of GFDM is worse than that of OFDM while the BER of the FBMC is nearly identical to that of the Ref-OFDM. Similar behavior has also been observed for other channels. These results are not included here for clarity of the plots.

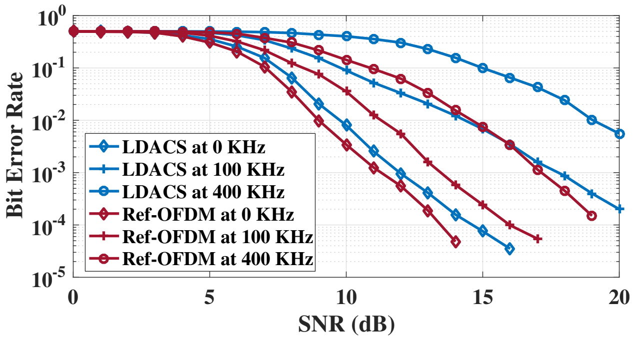

Figure 3.16: The BER comparison of Ref-OFDM and OFDM based LDACS in presence of DME interference for ENR channel with 342 kHz transmission bandwidth and three different center frequencies.

Next, we study the interference at the DME signals due to LDACS transmission with the transmission bandwidth of 732 kHz and 498 kHz. The interference (I) is calculated by the sum of PSD ($\phi(f)$) between two frequencies (f_1 and f_2)

and can be represented by:

$$I = \int_{f_1}^{f_2} \phi(f)df \tag{3.32}$$

Here, we consider LDACS signal at different center frequencies located at an interval of 50 kHz with the DME signal located at the fixed center frequency. The corresponding interference values are shown in Table 3.6 where NA refers to not applicable since corresponding center frequencies are not allowed for the requested bandwidth due to overlap with the main lobe of the DME signals. It can be observed that the proposed Ref-OFDM and FBMC based LDACS offer the lowest interference to the incumbent DME signals. In most of the cases, the interference is lower than 40 dBm which is the desired threshold as per the LDACS requirement and approximately 35 dBm better than existing LDACS. These results not only validate the superiority of the proposed waveform but also indicates the feasibility of multi-band multi-user deployment in case of Ref-OFDM and FBMC based LDACS.

c

Bandwidth (BW)	**Waveform**	**Transmission Center frequency w.r.t the DME center frequency (r = 50 kHz)**				
		$\frac{BW}{2}+r$	$\frac{BW}{2}+2r$	$\frac{BW}{2}+3r$	$\frac{BW}{2}+4r$	$\frac{BW}{2}+5r$
498 kHz	OFDM	7.1745	2.7038	0.9269	-0.1658	-0.8701
	GFDM	5.9571	-3.1187	-7.3229	-8.7974	-9.3662
	Ref-OFDM	0.3596	-38.7566	-40.7823	-42.1427	-43.1139
	FBMC	-2.0064	-37.8831	-39.8368	-40.9379	-41.6017
732 kHz	OFDM	6.4676	1.8911	NA	NA	NA
	GFDM	5.2885	-5.6320	NA	NA	NA
	Ref-OFDM	-27.1217	-41.6051	NA	NA	NA
	FBMC	-31.5356	-45.7056	NA	NA	NA

Table 3.6: Interference at DME in dBm due to various waveforms for transmission bandwidths of 498 kHz and 732 kHz

3.5.1.2 Multi-band Transmission

Here, we consider one user is transmitting in two non-contiguous bands of 186 kHz bandwidth with baseband center frequencies of -200 kHz and 200 kHz. It can be observed from the PSD plots in Figure 3.17 that the performance of windowed OFDM and GFDM based LDACS have degraded further compared to single band transmission. For instance, the interference at DME signal for existing LDACS is -4.7 dB compared to -5.5 dB in case single-band transmission for a given center frequency. As expected, it is much higher than -41.5 dB interference at DME due to the proposed Ref-OFDM based LDACS.

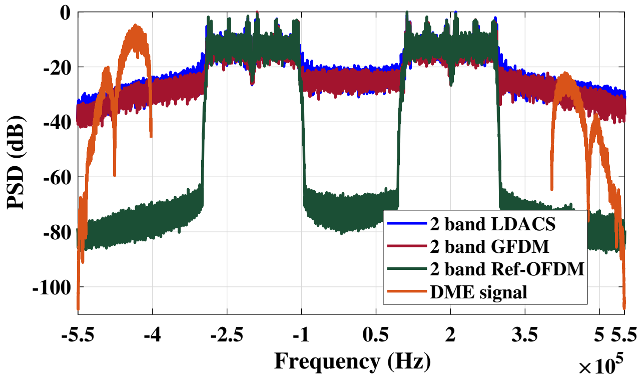

Figure 3.17: The PSD comparison for 2-band transmission for ENR channel with bandwidth of 186 kHz.

For this case, we compared the BER performance of existing and proposed Ref-OFDM based LDACS for three different channel conditions. As shown in Figure 3.18, the performance of the Ref-OFDM based LDACS is significantly better than existing LDACS. Poor BER performance for narrow transmission bandwidth of 186 kHz confirms the non-feasibility of existing LDACS for multi-band deployment.

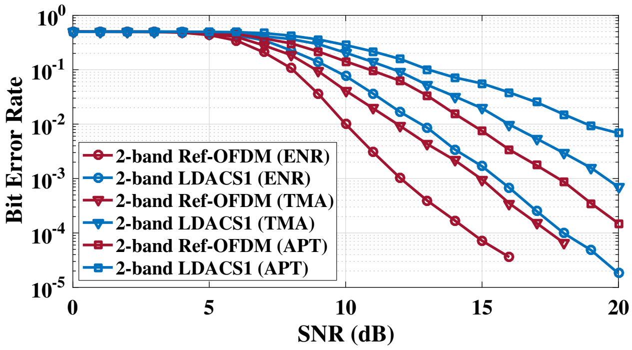

Figure 3.18: The BER comparison of Ref-OFDM and OFDM based LDACS for three channels in presence of DME interference for 2-band transmission with 186 kHz bandwidth.

3.5.1.3 Multi-user Transmission

Next, we consider the scenario where two users share the frequency band where the transmission bandwidth of one user is 342 kHz, and another user is 186 kHz. The center frequencies are the same as that of 2-band transmission considered before. The corresponding PSD plots shown in Figure 3.17 indicates very high interference to the DME signal from existing LDACS. For instance, the DME interference due to existing LDACS is 4 dB compared to -40 dB due to Ref-OFDM based LDACS.

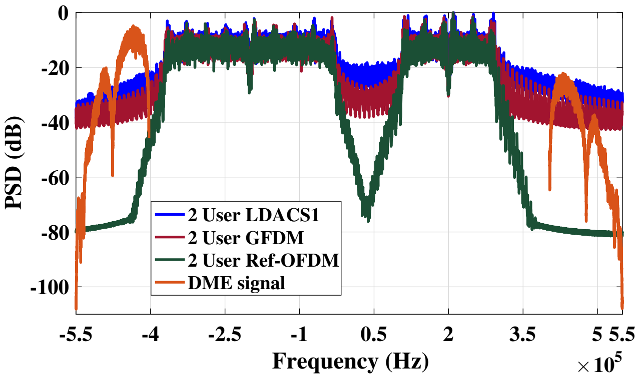

Figure 3.19: The PSD comparison for 2-user transmission for ENR channel with bandwidth of 186 kHz and 342 kHz.

For the above scenario, Figure 3.20 shows the BER performance of 2-user case for all three channel scenarios. It can be observed that the proposed Ref-

OFDM based LDACS is significantly better than existing LDACS. These results also confirm the feasibility of multi-user transmission using Ref-OFDM based LDACS.

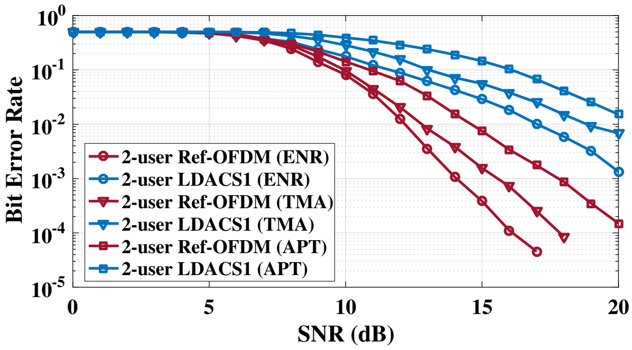

Figure 3.20: The BER comparison of Ref-OFDM and existing based LDACS for three channels in presence of DME interference for 2-user transmission with 186 kHz and 342 kHz bandwidth.

3.5.1.4 Complexity Comparison

In this section, the complexity comparison of various waveforms regarding the number of real multiplications for different numbers of sub-carriers is done. Here, we consider K-band transmissions in non-continuous bands where $K \in \{2, 4\}$. For such transmissions, Ref-OFDM uses a single reconfigurable filter capable of offering 16-band response. We also consider OFDM with conventional filter design and referred to as filtered OFDM (FOFDM). As shown in Figure 5.2, as K increases, the complexity of FOFDM increases while that of Ref-OFDM remains the same. The complexity of GFDM and FBMC with polyphase filter implementation for single band transmission is much higher than 16-band Ref-OFDM waveform. Also, the complexity of Ref-OFDM waveform is close to that of OFDM for 128 sub-carrier case making the proposed protocol and waveform a good alternative to next generation LDACS.

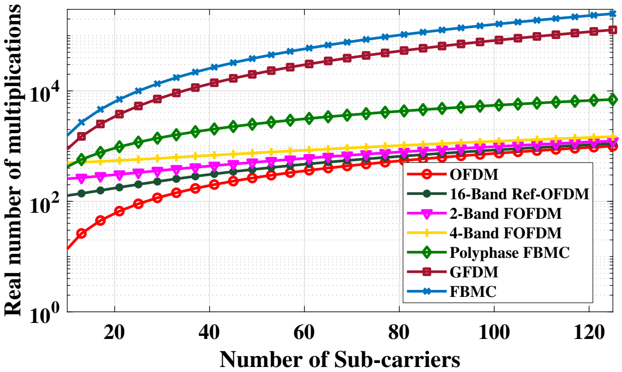

Figure 3.21: Computational complexity comparison of various waveforms for different number of sub-carriers.

We have verified the throughput and effect of ADC quantization on the PSD of the Ref-OFDM in [81]. Next, we present the experimental results to support our claims in the real radio environment.

3.5.2 Hardware Experimental Results

For experimental results and analysis, the parameters are considered as per LDACS specifications. We have done the comparison in terms of the PSD, BER and throughput for two different transmission bandwidths: 1) 498 kHz and 2) 732 kHz. The results are taken for different channel conditions such as Rayleigh channel (non-LOS considered) and Rician channel (LOS considered). The Ref-OFDM based LDACS has similar PSD performance in both the simulation and experimental setup. So, here we present the BER and throughput analysis considering three scenarios (1) variable distance, (2) variable altitude, and (3) variable DME antenna gain.

3.5.2.1 Variable Distance

Here, the BER performance is analyzed by varying the distance (D) between the LDACS/DME transmitter and the LDACS receiver considering 498 kHz and 732 kHz as the transmission bandwidths. We assume that DME and LDACS transmitter are located close to each other resulting in the strong interference. For all the distances, line of sight (LOS) and non-line of sight (NLOS) communications are examined. As shown in Figure 3.22, the BER degraded with an increase in D and proposed LDACS offers better performance than existing LDACS. It can be observed that BER gets worse for NLOS scenario as well as for higher transmission bandwidth.

3.5.2.2 Variable Altitude and DME Antenna Gain

In the realistic air to ground scenario, LDACS transmitter and DME transmitter are present at the ground level and LDACS receiver is present at the aircraft. Therefore, a similar possible scenario is build up by varying the altitude of the LDACS receiver and keeping the LDACS/DME transmitter at the same fixed

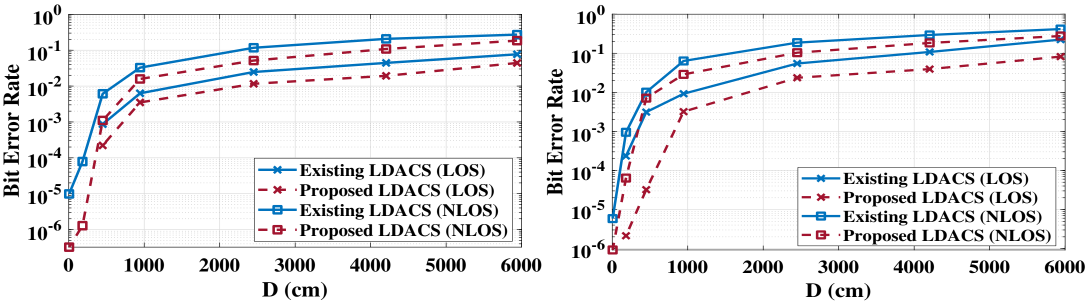

(a)

(b)

Figure 3.22: The BER comparison for the variable distance between LDACS/DME transmitter and LDACS receiver (D) for two different transmission bandwidths, (a) 498 kHz, and (b) 732 kHz.

level. The BER performance is analyzed by varying the heights of LDACS receiver and two values of the DME antenna gain (1) 2dB and (2) 10dB. When the LDACS receiver is placed at a higher altitude, the received LDACS signal power reduces while the interference power remains the same. Thus the BER performance degrades as shown in Figure 3.23. At the same time, with the increase in DME antenna gain (from 2dB to 10dB) the DME interference power dominates the LDACS transmitted signal power which causes in higher BER.

The proposed LDACS has better BER performance than the existing one for all the considered scenarios makes it a very enticing replacement to the existing W-OFDM based LDACS.

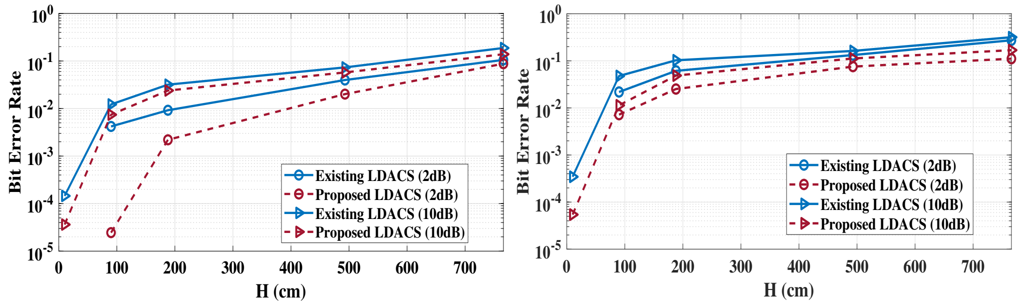

(a) (b)

Figure 3.23: The BER comparison for the variable altitude of the LDACS receiver and LDACS / DME transmitter (H) with DME antenna gain of 2dB and 10dB for two different transmission bandwidths, (a) 498 kHz, and (b) 732kHz.

3.5.3 Throughput Analysis

In this subsection, the achieved throughput by the proposed LDACS with the existing LDACS is compared and analyzed in the presence of the DME interference. The throughput results in Table 3.7 are achieved by transmitting the QPSK modulated LDACS signal in 732 kHz transmission bandwidth over the air via USRP implementation. We have considered two adjacent DME signals 3600 and 2700 pulse pairs per second and with frequency offsets from LDACS as -0.5 MHz and 0.5 MHz, respectively. As it can be observed from the PSD results (Figure 4.16), that the proposed LDACS has very less interference with the adjacent DME channel, hence it does not require any guard bands for interference reduction. This helps to achieve higher throughput for the proposed Ref-OFDM based LDACS over the variable distances and altitudes considered above. The achieved throughput values are presented in Table 3.7. When the distance and altitude are higher, we get less throughput because of the lower signal power. High throughput performance also supports a higher data rate, which is an essential requirement for future A2GC.

Distances (cm)	Throughput (Mbps) (existing)	Throughput (Mbps) (proposed)	Height (cm)	Throughput (Mbps) (existing)	Throughput (Mbps) (proposed)
5	4.2123	5.0125	10	4.9247	5.5475
182	3.7215	4.8245	90	1.5894	2.3245
450	2.2171	4.0548	188	0.5734	0.7581
945	0.7818	2.9002	493	0.1995	0.3883
2450	0.0567	1.7951	766	0	0
4205	0	0	-	-	-
5940	0	0	-	-	-

Table 3.7: Throughput achieved for variable distance and altitude

In addition, the proposed Ref-OFDM based LDACS offers additional benefits. It provides flexibility via reconfigurable filters to enable transmission in non-contiguous bands, and lower OOB emission allows multiple transceivers share the vacant spectrum. Such sharing enables low data rate services which in turn can potentially eliminate the need for LDACS2. The proposed architecture can be efficiently realized on the FPGA via a dynamic partial reconfiguration approach. For instance, in the case of narrowband or single user transmission, the Ref-OFDM can switch to OFDM by bypassing the filter thereby saving the dynamic power. The dynamic partial reconfiguration can also be exploited to change between the single band and multi-band transmissions. For instance, in case of single band transmission, the DFT block can be reconfigured with the adder block. Such flexibility is difficult in case of OFDM, FBMC and GFDM based LDACS. Similar to OFDM, Ref-OFDM can be extended to a multi-antenna system, unlike FBMC based LDACS.

3.6 Summary

In this chapter, the need of new waveform for LDACS-DME coexistence scenario is explained briefly. For better understanding of LDACS inlay deployment, the coexistence environment is discussed first along with the brief description of considered real time wireless channels for A2GC. For efficient coexistence, a revised LDACS protocol with a new frame structure is proposed. It is compatible to the existing one. To dynamically adapt the various transmission bandwidths (186-732 kHz) a Ref-OFDM waveform is proposed for the LDACS transceivers. The reconfigurable filter is designed using combination of CDM and MCDM approach. A single prototype filter can serve all the transmission bandwidths by choosing an appropriate decimation factor.

Simulation results show significant improvement over the BER and at least 32 dB lower interference to incumbent L-band users than existing LDACS. Furthermore, proposed work allows multi-band and multi-user transmission with adaptable bandwidth due to the proposed reconfigurable filter. Such transmission is not feasible in existing LDACS due to significant interference to incumbent L-band users. In addition, the computational complexity of Ref-OFDM is lower than other waveforms except OFDM making the proposed work an attractive solution for next-generation LDACS.

We also support our claims via experimental results in the real radio environment. we have developed an experimental testbed for the proposed Ref-OFDM based LDACS and compared the PSD, BER and throughput performance with the existing LDACS. For the performance analysis, different scenarios related to LDACS transmitter/receiver and DME transmitter are considered such as variable distance, variable altitude, LOS, NLOS, and variable DME antenna gain. The proposed Ref-OFDM based LDACS provides nearly 35 dB less OOB emission and offer better BER/Throughput in all the above-considered scenarios which makes it an alluring substitute to the existing LDACS.

To provide the flexibility and validate the performance of the transceivers in real time, there is a need of the prototyping of LDACS transceivers on hardware. The next chapter discusses the design and implementation details of OFDM, WOLA-OFDM and FOFDM on the Zynq System on Chip.

Chapter 4

Spectral Coexistence of LDACS and DME: Analysis via Hardware-Software co-design in Presence of Real Channels and RF Impairments

The increased demand has led to introduction of various new standards and protocols for LDACS transceivers as discussed in Chapter 3. Most of the existing works focused on the theoretical analysis and simulations of LDACS PHY along with an extension to multi-antenna systems. However, to understand the performance of LDACS PHY on fixed-point hardware in the presence of various RF impairments and wireless channels/interference, mapping of PHY on SoC is must.

In this chapter, we design and implement the existing as well as proposed LDACS PHY on heterogeneous Zynq SoC (ZSoC) platform , consisting of field programmable gate array (FPGA) as programming logic (PL) and Advanced RISC Machines (ARM) as processing system (PS). The PHY is also integrated with the programmable analog front-end to validate its functionality in the presence of various RF impairments and wireless channels and interference specific to the LDACS environment. We propose a novel hardware-software co-design approach and explore various PHY configurations by dividing it into PL and PS. Such co-design approach gives the flexibility to choose which part of the system to implement on PL and which on PS to meet the given area, delay and power constraints. It also allows users to modify both the software and hardware according to their requirement. Based on the part implemented on PS and PL the design has ten configurations. The work presented here is the extension of the thesis [82].

Currently, the various configuration variants of basic OFDM transceiver is designed and implemented on ZSoC. These variants are realized by dividing the architecture into two sections, one for PL and other for PS. The work is also extended for WOLA-OFDM and FOFDM transceivers. In this chapter, first we will discuss the required Hardware-Software setup followed by the transceiver architecture. The Implementation using Hardware-Software co-design approach on ZSoC is discussed in the latter part of the chapter. Finally the experimental results are presented.

4.1 Hardware - Software Setup

In this section, the design details of ZSoC ZC706 hardware along with the software requirements to implement the transceiver design are given.

4.1.1 Hardware Design Details

The hardware required to validate the transceiver models, consists of Xilinx Zynq System on Chip ZC706 evaluation board along. A JTAG cable and an ethernet cable is used to make the connection between the host computer and the evaluation board.

4.1.1.1 Zynq System on Chip Architecture

Xilinx ZSoC is a single chip platform which comes with higher degrees of flexibility, scalability and reconfigurability. The architecture of this is presented in Figure 4.1. It provides the flexibility to design low end and high end applications on a single platform along with the flexibility of programming the processor system (PS) and programming logic (PL) separately according to the exact needs of corresponding application [83]. ZSoc integrates the processor and FPGA with input output peripherals therefore, leading to lesser on board components. Due to this, it achieves better performance and leads to low power consumption compared to two chip platforms. ZC706 evaluation board is used to do all the analysis in our work. It consists of a dual core cortex A9 Advanced RISC Machines (ARM) as the software component (PS) and a Xilinx

Device	ZC706
FPGA	Kintex-7
Registers	4,37,200
LUTs	2,18,600
DSP slices	900
BRAM blocks	545
Processor	ARM Cortex 9

Table 4.1: Specifications of Zynq board

28nm Kintex 7-series FPGA as the hardware component (PL) [61]. Both PS and PL communicate with each other via Advanced eXtensible Interface (AXI) protocol. The specifications of the Zynq board are given in the Table 4.1.

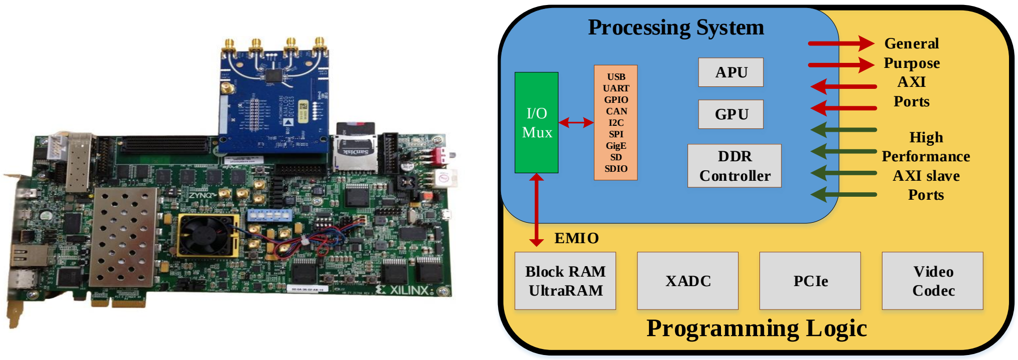

Figure 4.1: Snapshot of Xilinx ZC706 evaluation board along with its important architectural features [61].

Processing System in ZSoC consists of the input/output peripherals, Application processor unit (APU), memory interfaces and interconnect. The APU has the dual core ARM Cortex-A9. the PS has a dual ported 256 KB on-chip RAM. The on-chip memory is accessible by both the CPU and the PL. Using on chip memory allows low latency access of data from the CPU, thereby increasing the speed of operation. Along with that it has 1GB of dynamic memory. dynamic memory controller allows 16 bit and 32 bit wide access to this 1 GB dynamic memory. It also allows PS and PL to share this memory. It has four 64-bit AXI slave ports, out of which two ports are dedicated to the PL, one to PS and one is shared by all the other AXI masters. In ZSoC, PS always boots first and thus making the architecture fully autonomous to PL. Along with memory, PS also has a total 130 IO port out of which 54 ports are used for multiplexed IO (MIO) which are shared by static/ flash memory interfaces and peripherals. The remaining 76 ports are dedicated for double data rate (DDR).

Programming Logic is similar to conventional FPGA which consists of flip flops, adders, look up tables, configurable logic blocks (CLBs) etc. There are 8 LUTs, 16 flip flops and two 4-bit cascadeable adders per CLB. Along with CLBs, PL also consists of digital signal processing (DSP) blocks, 36 Kb Block RAM, PCI interface etc. ZC706 supports a wide range of voltage from 1.2V to 3.3V. It also has on-chip temperature and power supply sensors. The measurements are stored in dedicated registers and can be accessed using JTAG connection.

In ZSoC, PS and PL are independent of each other and perform the task separately. Thus there is a need of proper communication standard or protocol for efficient implementation. For that Xilinx adopted AXI interface for zynq architecture. This AXI interface is based on Advanced Micro-controller Bus Architecture (AMBA) and synchronizes the data transfer between PS and PL. It has two parts : AXI master and AXI slave. The AXI master always initiates the read/write operation and AXI slave responds to that request as shown in Figure 4.2. In ZSoC, on 7 out of 9 ports PS acts as master and on the remaining 2 ports PL acts ass master. Three modes are used to configure these ports : AXI lite, AXI stream and AXI memory mapped. The experimental results analysis done in this thesis uses AXI lite interface for low throughput requirements between PS and PL on LDACS transceiver.

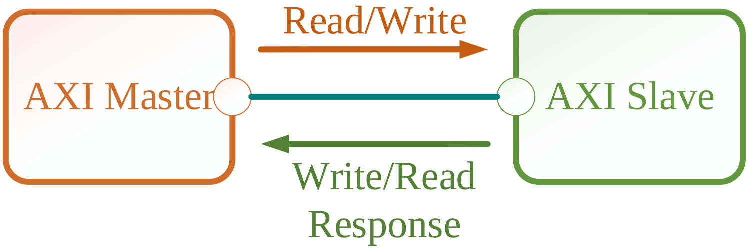

Figure 4.2: AXI master and slave link.

4.1.2 Software Requirement

To meet the hardware setup, tools from Mathworks and Xilinx are used to design and simulate the models. In this chapter, the analysis is done using MATLAB 2016a and Vivado 2015.2.1. Embedded coder and HDL coder are the specialized tools from Mathworks to target the implementation on PS and PL respectively.

Hardware-Software co-design Workflow

To design and simulate the transceiver models Hardware-Software co-design approach is being used. It is an important approach to implement any algorithm on ZSoC as it utilizes the heterogeneity of PS and PL. This approach also gives the flexibility to choose which part of the system is best suited to be implemented on PL and which on PS. PS makes easy and faster decision-making operations on the other hand PL reduces power consumption and increases speed. The steps for hardware-software co-design approach are as follows:

A1. Designing a Simulink model for transceivers and set the parameters like number of samples per frame, sampling frequency, total FFT size, Active subcarriers, and subcarrier spacing. All the blocks present in the Simulink library are not hardware synthesizable. So, while designing the Simulink model these blocks need to be avoided.

A2. Differentiate the subsystem of the model which is going to implement on the PL believing that all the other subsystems will target to implement on PS. PL works in sample mode, and PS works in frame mode, which requires an appropriate sample to frame and frame to sample conversion at the boundary of PS-PL interface. Figure 4.3 shows the design have N functional blocks. Transmitter subsystem consisting of blocks $1_T, 2_T, 3_T...i_T$ are implemented on PS, and remaining blocks are implemented on PL. Similar process is used for the receiver operations. Note that, the output to the host computer will come back through the PS.

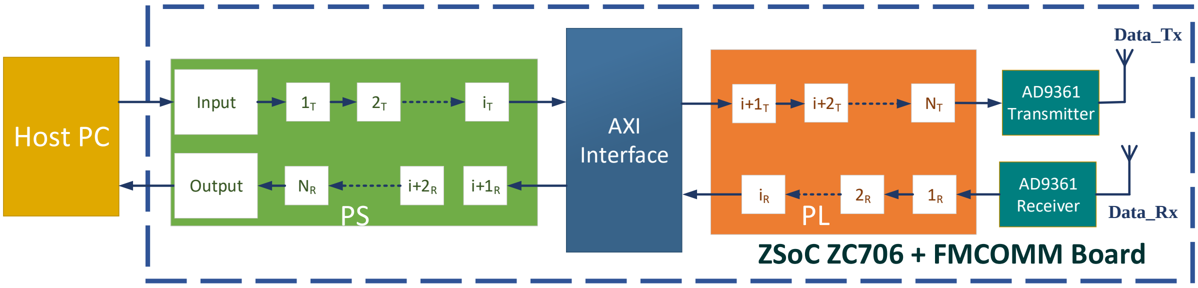

Figure 4.3: Hardware-Software co-design approach for algorithm implementation.

A3. Then, run the HDL Workflow Advisor to auto-generate an IP Core block for the transceiver design as shown in Figure 4.4. It automatically generates a Vivado block diagram to combine the DUT with all the AXI interface components and creates an interface model to interact with the PL. It then uses the HDL coder and Xilinx Vivado for synthesis, implementation and bitstream generation. This bitstream is then used to program the PL.

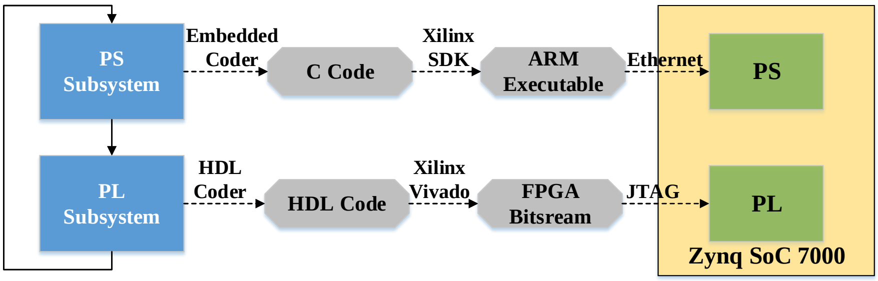

Figure 4.4: Hardware-Software workflow for ZSoC using HDL and embedded coders of Matlab/Simulink and Xilinx Vivado.

A4. Finally, by setting the generated interface model to run in external mode, Simulink uses Embedded Coder to generate C code for all the processing blocks. Xilinx Vivado SDK then converts this C code to ARM executable code. When we run the simulation, it launches the executable on PS via Ethernet.

In the next section, we will explain each block of the transceiver models.

4.2 Transceiver Architecture

In this section, we present the detailed architecture of the proposed transceiver and extensions via windowing and filtering. We also discuss the design of AFE along with various LDACS specific channels as well as interference. The detailed block diagram of the transceiver is shown in Figure 4.5.

4.2.1 Stimulus and Verification Blocks

The stimulus block at the transmitter reads the input data bits to be transmitted. They are either stored on on-board ZSoC memory or they can be transmitted from the laptop over Ethernet (ENET). For illustration, we consider the total 864 data bits divided into 36 distinct frames of 24 bits each. Frame formation is done using simple counters and multiplexers. The verification block receives the frame and reads the corresponding data bits for subsequent performance analysis. Both blocks are implemented on the PS.

4.2.2 Digital Baseband Processing Blocks of Transceiver

Various baseband signal processing blocks of the transceiver are shown in Figure 4.5. The blocks such as scrambler, inter-leaver, data encoder, data modulator, frame generation, IFFT followed by CP addition, and preamble addition are desired signal processing blocks for the OFDM transmitter. The receiver consists of similar blocks that perform the operations in the reverse direction. The OOB emission performance of the transceiver can be improved further using windowing or filtering or both. For windowing operation, two new blocks, 1) Cyclic suffix addition, and 2) Windowing, are added before preamble addition. Similarly, at the receiver, we need overlap and add block. For filtering operation, new filtering blocks are added at the transmitter as well as the receiver. The detailed explanation of various blocks in Figure 4.5 is given later in 4.2.2.1. Each transceiver block can be realized on the PS or PL. In Figure 4.5, we consider

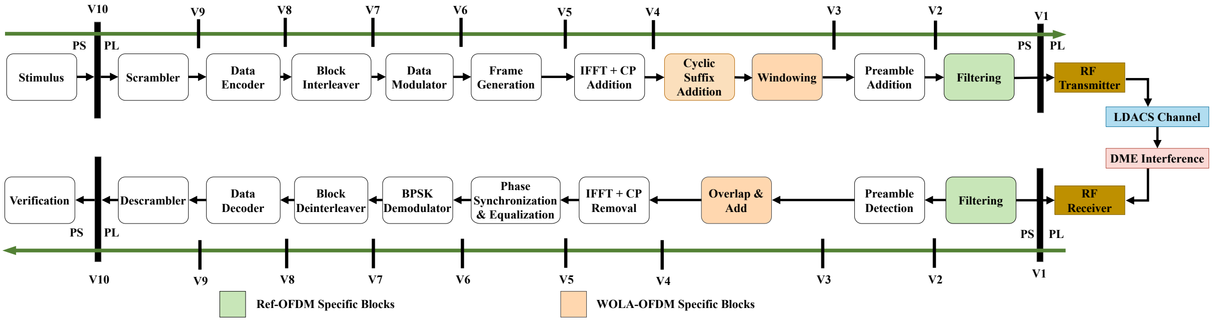

Figure 4.5: Block diagram showing different configurations of the LDACS transceiver along with windowing and filtering blocks.

10 possible configurations, $V1, V2, .., V10$. Each configuration offers a unique boundary between PS and PL. We discuss these configurations in detail later in Section 4.3. Here, we focus on the functionality and architecture of each block for the serial implementation on the PS as well as parallel implementation on the PL.

4.2.2.1 Orthogonal Frequency Division Multiplexing (OFDM)

The OFDM based transmitter consists of blocks such as scrambler, convolutional encoder, interleaver, binary phase-shift keying (BPSK) modulator, Inverse Fast Fourier Transform (IFFT) and cyclic prefix adder. The scrambler does the bitwise XOR operation on the incoming input data and a random scrambling sequence generated by the linear feedback shift register (LFSR). The same sequence is used to descramble the data at the receiver. This is followed by a convolutional encoder which uses the generator polynomial of $g_0 = 133$ and $g_1 = 171$. These correspond to a rate 1/2 code with a maximum free distance of 7. Thus, the output of the convolution encoder is twice the length of the input. The interleaver performs two-step permutation on coded data and used to handle burst errors. The interleaved data is then converted to complex samples using the BPSK modulator to obtain 48 samples. Note that any other modulation scheme such as QPSK, 16 QAM, or 64 QAM can also be used. These samples are then mapped to 128 points IFFT, as shown in Figure 4.6. As per the LDACS specifications, 64 subcarriers are used, out of which 50 are active subcarriers carrying data and pilot symbols. The number of subcarriers carrying pilots and data in each symbol is not fixed and depends on the symbol index. For example, the number of data subcarriers in the symbol with index 0 and 1 are 36 and 48, respectively, while the number of pilot subcarriers are 14 and 2, respectively. One LDACS frame comprises 54 symbols, as shown in Figure 4.6 and the pilots at each symbol follow specific patterns except symbols with indices 0, 51, 52, and 53. Please refer to [84] for more details on the architecture which performs such a symbol to subcarrier mapping in SoC. For the simplicity of representation, we discuss the architecture of various blocks of the transceiver assuming the transmission of OFDM symbol with index 1 (or 6, 11, . . . , 46) of LDACS frame consisting of 48 data, two pilots, 1 DC, and 13 Null subcarriers. Note that depending on the symbol index, appropriate control signals are generated to meet the symbol mapping requirements of the LDACS frame, as shown in Figure 4.6. The corresponding details are omitted to maintain the brevity of and avoid repetitive description. Here, we mainly focus on the forward link transmission of LDACS.

To avoid inter-symbol interference, a cyclic prefix (CP) of length 11 is added to the OFDM symbol. In the end, preambles are added, which aim the receiver

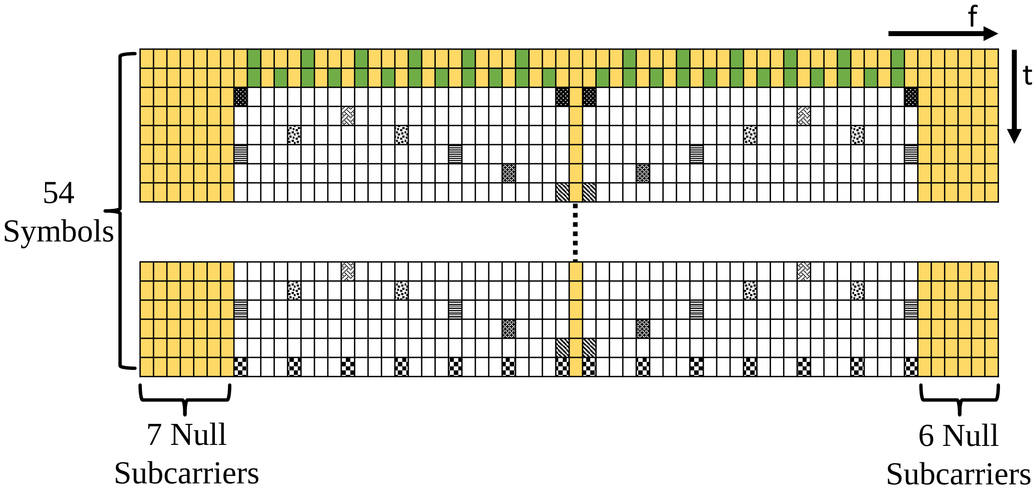

Figure 4.6: LDACS frame with 54 symbols and corresponding symbol-to-subcarrier mapping.

for synchronization.

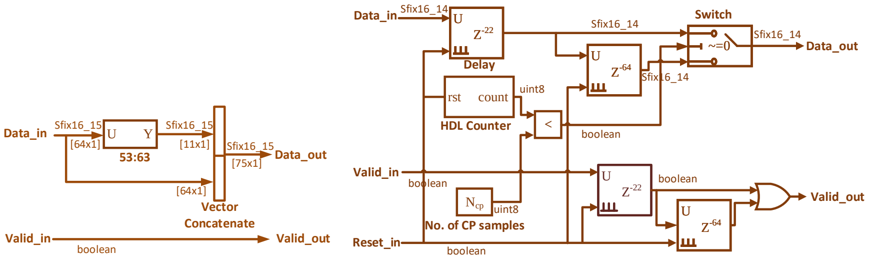

(a) (b)

Figure 4.7: (a) PS and (b) PL implementation of OFDM cyclic prefix addition.

The difference in processing modes of PL (Sample mode) and PS (frame mode) leads to a difference in the implementation of each block of the transceiver in the two modes. Due to limited space constraints, we discuss the architecture of a few blocks here while remaining blocks are discussed in detail in Supplementary [84]. The PS implementation of the CP addition involves only vector concatenation due to frame-based processing. As shown in Figure 4.7(a), the last 11 samples of the IFFT output are appended in the beginning as CP. On the other hand, PL implementation of the same involves additional counter and registers to store the samples to be added as CP. As shown in Figure 4.7(b), we need two registers of length 2CP (22) and N (128) along with Mod-N counter.

For easier understanding, we consider the illustrative example of a frame consisting of 4 samples with 1 CP sample. In this case, we need the first register of size 2 and the second register of size 4. In the first clock cycle, input sample, a_0, is loaded into the first register, and hence the content of two registers are $\{a_0, 0\}$ and $\{0, 0, 0, 0\}$. At the fifth clock cycle, content of two registers will be $\{a_4, a_3\}$ and $\{a_2, a_1, a_0, 0\}$. In the next clock cycle, frame reset (reset_in) happens since we have received all samples of a frame, and hence the content of two registers will be $\{0, a_3\}$ and $\{a_2, a_1, a_0, 0\}$. From the next cycle onward, output valid is always 1 and we get the first output which is a_3 from the first register and content of register becomes $\{b_0, 0\}$ and $\{a_3, a_2, a_1, a_0\}$. Here, b_0 is the first sample of a new frame. Subsequently, the next four outputs are taken from the second registers. In this way, we get the output as a_3, a_0, a_1, a_2, a_3. Similarly, in next four clock cycles, the output will be b_3, b_0, b_1, b_2, b_3. As discussed before, valid and reset signals are used to synchronize the transfer of data between any two adjacent blocks and needs to be handled carefully in each block. For instance, as shown in Figure 4.7(b), a valid signal involves 22 and 64 tapped delays, similar to the ones used in the data signal.

4.2.2.2 WOLA-OFDM

In WOLA-OFDM, the conventional rectangular window is replaced by a windowing pulse with soft edges to improve the out-of-band emission of CP-OFDM [29]. This soft edge windowing is applied in the time domain via point-to-point multiplication between the output of the CP block and window function. The additional sequence of operations at the transmitter are as follows:

A1. Cyclic Extention: The CP addition is slightly different in WOLA-OFDM than CP-OFDM. As shown in Figure 4.8, the CP is formed by appending the last $CP + W$ samples of a given symbol (output of IFFT) to its beginning, and the cyclic suffix (CS) is formed by appending the first W samples of a given symbol in its end. Therefore, the length of the WOLA-OFDM time domain symbol is extended from N to $N + CP + 2W$, as shown in Figure 4.8.

A2. Windowing: After the cyclic extension, a Root Raised Cosine (RRC) window of length $L = N + CP + 2W$ is applied in the time domain. For LDACS, we have $N = 64$, $CP = 11$ and $W = 8$, and corresponding window length is $L = 91$ with the taper region of length W.

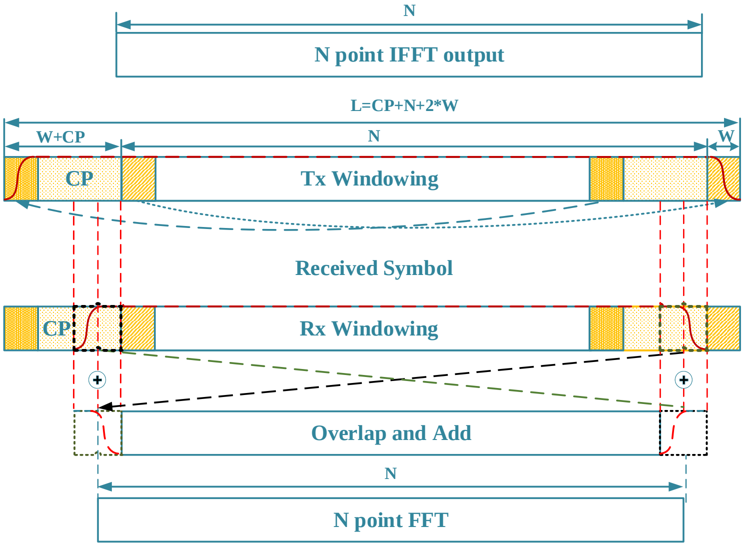

Figure 4.8: Cyclic prefix and cyclic suffix processing along with windowing for WOLA-OFDM.

Such windowing at the transmitter demands additional signal processing at the receiver to suppress the asynchronous inter-user interference. As shown in

Figure 4.8, the additional steps at the receiver are as follows:

A1. The starting and ending samples of length $W + \left\lfloor \frac{CP}{2} \right\rfloor = 13$ and $W = 8$ respectively are discarded, and the RRC windowing is applied at the retrieved data. The window length at the receiver is not same as the transmitter and the receiver window length is taken as $N + \left\lceil \frac{CP}{2} \right\rceil = 70$.

A2. Two adjacent received WOLA-OFDM symbols are overlapped with each other and then added to the next symbol to retrieve the 64 main samples. The overlap and add process is applied to minimize the effects of windowing on the useful data, as shown in Figure 4.8.

The PS and PL implementation of windowing is shown in Figure 4.9 (a) and Figure 4.9 (b), respectively. The PS implementation at the transmitter is straightforward due to a frame-based approach in which a time domain multiplication of the input data with the windowing coefficients is performed, as shown in Figure 4.9 (a).

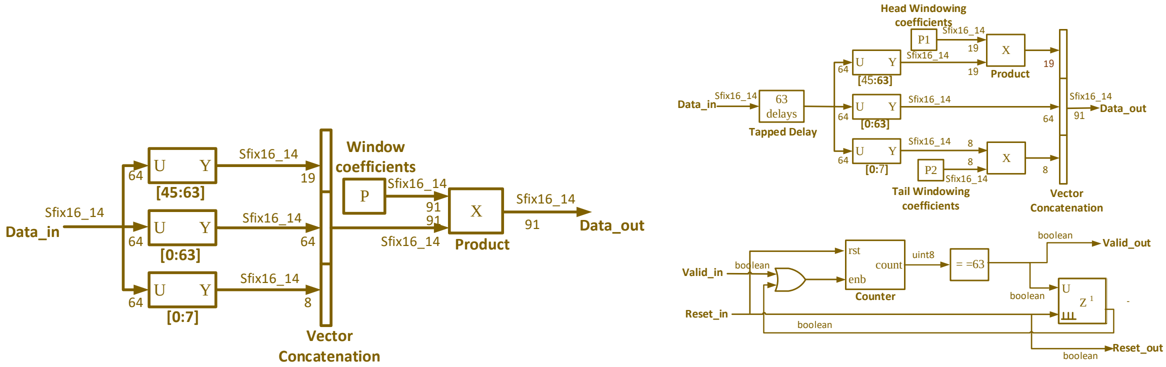

(a) (b)

Figure 4.9: (a) PS and (b) PL implementation of time-domain windowing.

In PL implementation, the data is coming in the form of samples, therefore to add the cyclic prefix, suffix, and windowing samples, all 64 samples (1 frame) are collected with the help of 63 tapped delays. For PL implementation of windowing, we exploit the parallel operation by dividing the windowing into head and tail sections. Consider $P1$, and $P2$ denote the windowing coefficients for head and tail sections, respectively. The $P1$ is of length $W + CP$ in which the first W samples corresponds to the first W RRC windowing coefficients (P) while remaining samples are fixed to 1. The $P2$ is of length W, and it corresponds to the last W RRC windowing coefficients, (P). In the end, the cyclic prefix, cyclic suffix, and the data are concatenated, and total 91 samples are selected for transmission over the air.

The input valid signal increments the counter value, and the counter counts till 63 i.e., a total of 64 samples. Once we have received the whole frame of 64 samples (without adding cyclic prefix and suffix), the output valid signal will become one. The output valid signal is generated for one clock cycle for the output frame of size 91 (similar to the size of the transmitted data (91 samples)).

At the receiver, windowing is implemented in the same manner as the transmitter. Additionally, the overlap and add processing is performed on the $N + \lceil \frac{CP}{2} \rceil = 70$ windowed samples by directly extracting the desired samples from the received frame and then concatenate it to the beginning and ending of the symbol. The PS and PL implementation is the same for overlap and add processing, as presented in Figure 4.10 (a) and (b).

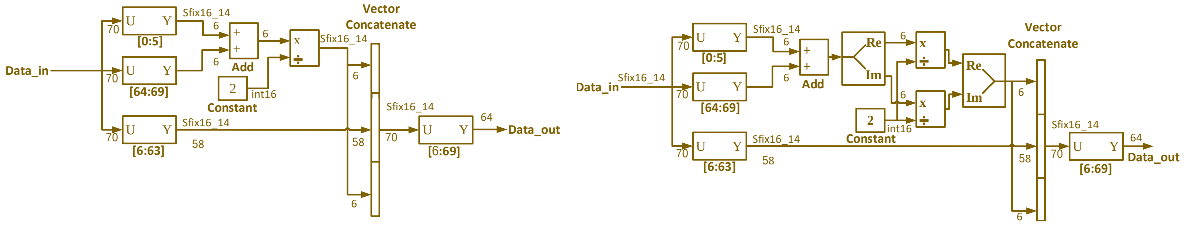

(a) (b)

Figure 4.10: (a) PS and (b) PL implementation of overlap and add processing.

4.2.2.3 Filtered OFDM

The FOFDM uses a linear phase finite impulse response filter instead of time-domain windowing for further improvement in out-of-band emission. In Chapter 3, we have shown that FOFDM enables higher transmission bandwidth compared to bandwidth limitation to 498 kHz in the OFDM system. It also enables the transmission in non-contiguous bands and the sharing of adjacent frequency bands among asynchronous users. However, the filter needs to be carefully designed and implemented as it may lead to higher inter-symbol and inter-carrier interference. In the proposed FOFDM transceiver, we consider LDACS with 480 kHz of bandwidth with a sampling frequency of 1.1 MHz and hence, we designed a linear phase low-pass filter of order 150 with a normalized cut-off frequency of 0.86 and the transition bandwidth of 0.02 generated using park McClellan approach [85, 86]. The PS and PL implementation of the FIR filter is shown in Figure 4.11 (a) and 4.11 (b) respectively.

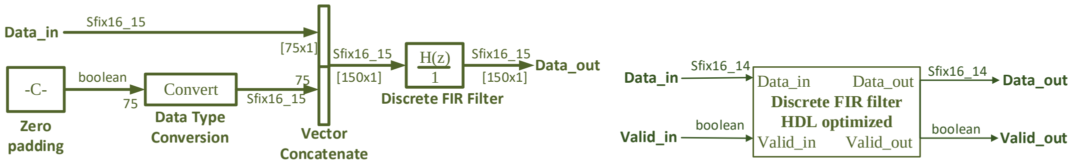

(a) (b)

Figure 4.11: (a) PS and (b) PL implementation of the filter.

The filter specifications and implementation are identical at the transmitter and receiver. For the implementation of the filter, we have directly used the HDL optimized model provided by Xilinx. In case of PS implementation, we need additional zero-padding to handle delay balancing and selector to choose the desired filtered data. For PL implementation of the filter, we have studied the effect of word-length on the performance of the transceiver. Please refer to Section 4.4 for more details.

4.2.3 Analog Front End: RF Transmitter and Receiver

The output of the transmitter is passed to the AFE for over-the-air transmission in L-band. The AFE is designed using the RF models provided by Analog Devices for use in MATLAB/Simulink. The transmitter consists of Digital up-conversion (DUC) filters, analog filters and RF front-end as shown in Figure 4.12. The digital up-conversion filter is a series of digital FIR filters that convert the baseband signal to an intermediate frequency (IF) signal. The sample rate of the DUC filter should be the same as the input signal. The digital filter also introduces the noise floor. The analog filters are used to shape this noise floor and provide a continuous-time signal processed by the RF front-end. The RF front-end up-converts the IF signal to RF carrier frequency using the local oscillator, followed by amplification using a power amplifier.

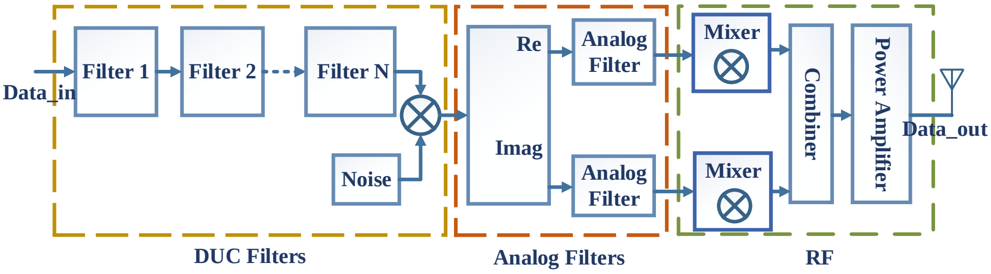

Figure 4.12: AFE: RF transmitter.

At the receiver side, the RF front-end down-converts the signal centered on the same LO frequency to IF using a quadrature demodulator, as shown in the Figure 4.13. The RF front-end has mainly three components: low noise amplifier (LNA), quadrature demodulator (Mixer), and trans-impedance amplifier (TIA), and the chain is indicated as LMT. The gains of each component are tunable and controlled by the AGC. The analog filters provide a continuous-time signal to the ADC. The ADC models a high-sampling rate third-order delta-sigma modulator. The low-pass digital down conversion filters convert the highly sampled signal at the output of the ADC to the baseband. The output of the AFE is passed to the OFDM receiver in Zynq. The integration of the AFE with the transceiver in Figure 4.5 and its parameters as per the LDACS specification are discussed in Section 4.4.1.

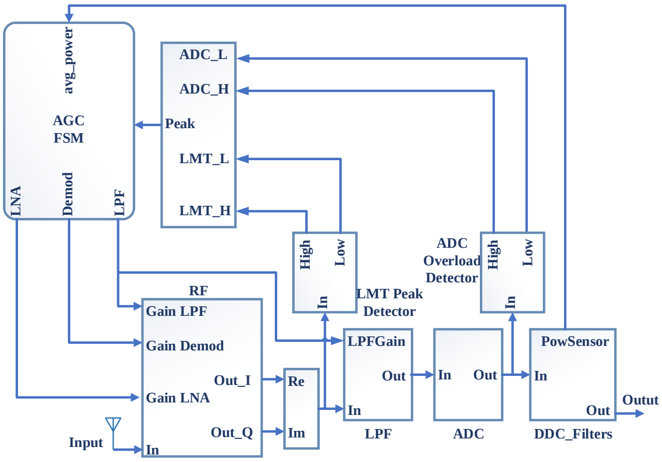

Figure 4.13: AFE: RF receiver.

The Wireless Channels for different flight modes Airport (APT), Terminal Maneuvering Area (TMA), En-routing (ENR) and DME Interference are considered for the implementation. This has been discussed in Chapter 3 in more details.

4.2.4 Receiver

At the receiver, the preamble detection block detects the beginning of the data frames using auto-correlation and extract it for subsequent processing. For cyclic prefix removal, the starting 11 samples are discarded out of the 75 incoming samples. The remaining 64 samples are given as input to the 64 point FFT block. Out of 64 symbols at the output of the FFT block, 48 data symbols are extracted by a selector. The output data symbols are demodulated using the BPSK demodulator. The deinterleaver then deinterleaves the bits using the predefined sequence followed by decoding using a Viterbi decoder using the same generator polynomial as a convolutional encoder in the transmitter. The descrambler uses the corresponding descrambling sequence to retrieve the 24 bits of a frame. A similar process is repeated for each frame. The next section presents the HW-SW co-design approach used for transceiver design and implementation.

4.3 Hardware-Software co-design Approach

The HW-SW co-design approach gives the flexibility to choose which part of the transceiver is best suited to be implemented on PL and PS of the ZSoC. In this section, we present design details of various transceiver configurations (V1-V10), shown in Figure 4.5 realized using the HW-SW co-design approach. The data transfer between PS and PL plays an important role in this approach, and corresponding details are summarized in Table 4.2.

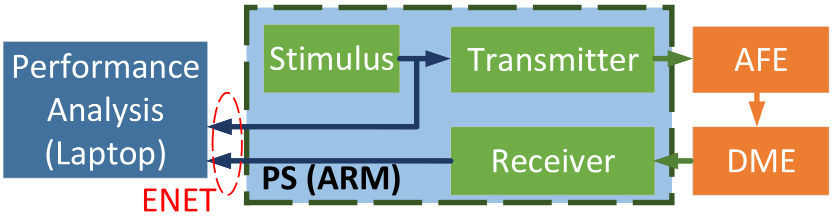

Figure 4.14: Configuration V1 of the transceiver.

We begin with the configuration V1 in which the complete transceiver is implemented on the PS, as shown in Figure 4.14, and hence, there is no data transfer between PS to PL as shown in Table 4.2. The stimulus model generates 32-bit unsigned integers out of which 24 are data bits (single frame), 2 are valid and reset signals, and remaining are zero-padded bits. Each data bit is modulated and processed to obtain an OFDM symbol with 75 samples (64 subcarriers + 11 samples as CP). Each sample can be represented in the form of an 8/16/32-

bit fixed-point data type. Each OFDM symbol in a frame comprises 75 samples (64 + 11 CP) and corresponding symbol period is $120\mu s$ assuming 1 sample takes $1.6\mu s$. We refer this as time per frame symbol (tpfs). With 36 data frames, 2 pilot frames, and additional delays due to frame synchronizations, one simulation runs for $43 * tpfs$ duration. The performance analysis model compares the transmitted and received bits for subsequent BER and throughput analysis. The realization of this architecture on ZSoC is done using MATLAB HDL coder and verifier, along with Embedded Coder toolboxes.

Model Variants	Data Type	Size of 1 element	No. of elements
V1	-	-	-
V2 (FOFDM)	Signed Fixed Point	8/16/32 bits	150
V3	Signed Fixed Point	8/16/32 bits	75
V4 (WOLA-OFDM)	Signed Fixed Point	8/16/32 bits	91
V5	Signed Fixed Point	8/16/32 bits	48
V6	Signed Fixed Point	8/16/32 bits	48
V7	Boolean	1 bit	48
V8	Boolean	1 bit	24
V9	Boolean	1 bit	24
V10	Boolean	1 bit	24

Table 4.2: Data transfer between PS and PL (transmitter side)

In configuration V2, the filtering operation is moved to PL, and hence, it is applicable only for FOFDM. As shown in Figure 4.15, the transmitter and receivers are divided into two sections, one for PS and other for PL. For V2, the output of transmitter_1 is the frame consisting of 150 complex filtered OFDM samples, each of which can be represented in 8/16/32-bit fixed-point format. One such frame, along with valid and reset signals are interfaced with AXI-compatible buffer realized in PL. The buffering is necessary for subsequent sample-based processing in PL. Similarly, unbuffering is needed while passing the data from PL to PS after the filtering operation of the receiver in PL (Receiver_1). Note that the sampling time of the blocks in PS is $120\mu s$ while the sampling time of the blocks in PL is $1.6\mu s$.

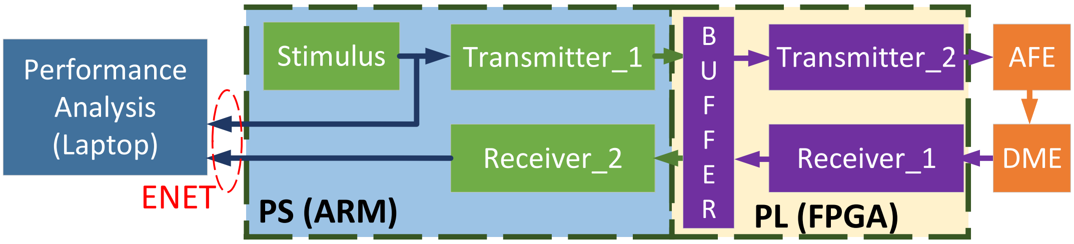

Figure 4.15: Configurations V2-V9 of the transceiver.

Configurations V3-V9 are similar to V2, where few more blocks are moved from PS to PL. For instance, in V3, preamble addition and detection blocks are realizing in PL along with filtering (in FOFDM). The configuration V4 realizes the windowing, overlap and add block along with the preamble addition and detection in PL, and the rest of the blocks are implemented on PS. This configuration is only applicable in WOLA-OFDM. In configuration V5-V6, IFFT and CP addition operations are also moved to PL, and hence, frame size is reduced from 75 to 48, as shown in Table 4.2. Similarly, in configuration V7, data modulation and demodulator blocks are moved to PL, which means Boolean data being transferred between PL and PS. For configurations V8-10, the number of data elements are reduced from 48 to 24 since channel encoder and decoders with a coding rate of $\frac{1}{2}$ are moved to PL. In final configuration V10, an entire transceiver is realized on PL except for stimulus block. It can be observed that each configuration needs to be designed carefully to synchronize the data transfer between PS and PL. Furthermore, the architecture of the block changes when it is moved between PS and PL due to frame and sample-based processing. For

PL implementation of each block, we have added pipelining inside the block as well as between the blocks. This demands additional synchronization efforts between PS and PL due to the change in latency. The next section presents the experimental setup done for taking the PSD, BER and complexity results.

4.4 Experimental Setup and Result Analysis

In this section, we present the details of the experimental setup and analyze different results to compare the performance and complexity of the proposed transceivers.

4.4.1 Testbed Setup and Configuration

In this work, we have used the Xilinx ZSoC ZC706 evaluation board for implementation of the proposed transceivers. It consists of dual-core cortex A9 Advanced RISC Machines (ARM) as the software component (PS) and Xilinx 28nm Kintex 7-series as the hardware component (PL) [61]. It is a processor centered device in which PS always boots first and is fully autonomous to PL. Both PS and PL communicate with each other using the Advanced eXtensible Interface (AXI) protocol. There are 9 AXI ports between PS and PL, and in this project, we use four ports for communication between PS and PL. Among various AXI protocols, we use AXI-stream for communication between PS and PL and AXI-Lite for communication between various signal processing blocks realized in the PL.

For the design and implementation of the transceivers, we have used MATLAB 2017b and Vivado 2016.4. These are augmented with various MATLAB toolboxes such as Embedded coder and HDL coder/verifier to target the implementation on the PS and PL, respectively. To design and configure the AFE, we have used RF Toolbox along with communication and signal processing toolboxes, hardware support packages provided by Mathworks.

The AFE is programmed to meet the desired sampling and carrier frequency requirements of the LDACS. The custom digital and analog filters are designed and configured with the help of the RF Toolbox of the Matlab/Simulink. For the LDACS transceiver, the passband and stopband normalized frequencies are 0.33 and 0.41, respectively. The stopband attenuation is 80 dB, and the desired baseband sampling rate is 1.1 MHz. The filter at the receiver is identical to the transmitter. The local oscillator frequency is set to 985 MHz as the LDACS is deployed in the range of 960-1164 MHz, and for such up-conversion, various rate changer blocks are added in the design. The output of the AFE receiver is scaled by an appropriate factor (0.00019 to be exact) so that the power level of the signal at AFE receiver output closely matches the signal at AFE transmitter input. The AFE transceiver also introduces the phase noise due to transmission at RF frequency, and hence, it demands phase error estimation and correction at the receiver. For the proposed transceiver, we have used pilot signals in LDACS for phase estimation, and accordingly, correction is applied to all received samples. Next, we present the experimental results demonstrating the PSD and BER performance of the proposed transceivers using the discussed ZSoC based testbed.

4.4.2 Power Spectral Density (PSD) Comparison

We begin with the PSD comparison for OFDM, WOLA-OFDM, and FOFDM transceivers and analyzed their OOB emission. Since higher OOB emission leads to higher interference to the legacy DME users, the transceivers should have lower OOB emission, and it should not exceed the desired interference constraints of the DME. Here, we assume that single LDACS transmitter is active in 1 MHz of the spectral gap between adjacent DME channels.

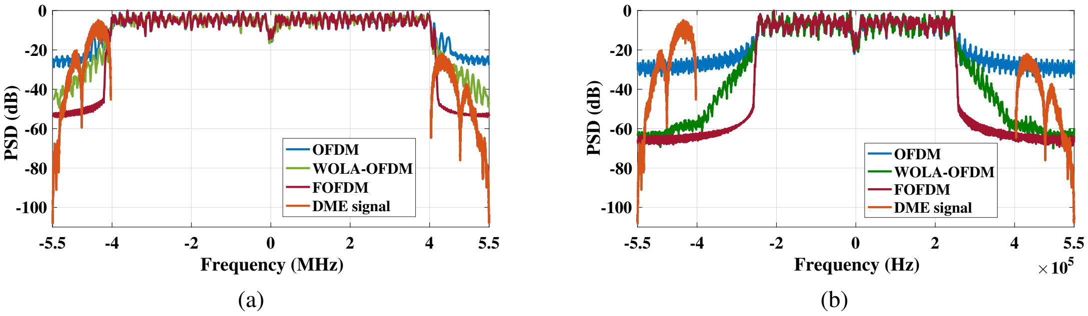

Figure 4.16: The PSD comparison of various waveforms for two different transmission bandwidths, (a) 732kHz, and (b) 498kHz.

The PSD comparisons of OFDM, FOFDM, and WOLA-OFDM for 2 transmission bandwidths 1) 732 kHz and 2) 498 kHz are presented in Figure 4.16 (a) and (b) respectively. The legacy DME transmission is shown using orange color. Note that 498 kHz is the maximum possible bandwidth of existing OFDM which gives a good trade-off between bandwidth and mutual interference protection. Though FOFDM can achieve 800 kHz bandwidth, we have chosen 732 kHz because it can be achieved using the frame structure same as that of 498 kHz, making it compatible with legacy LDACS. For all the transceivers, word-length (WL) is fixed and equal to 32 bits. It can be observed that the FOFDM has approximately 40 dB lower OOB emission and hence, much lower interference to the legacy DME signals. This allows FOFDM to increase the transmission bandwidth from the suggested 498 kHz (maximum possible in OFDM) to 732 kHz leading to significant improvement of approximately 50% in the spectral utilization over existing OFDM.

Next, we compare the performance of all transceivers by varying the WL. First, we change the WL of windowing and filtering blocks of the transceiver to 8/16 while keeping the WL of the rest of the transceiver to 32. As expected, there will be no change in the performance of OFDM as it does not involve windowing and filtering. The PSD of FOFDM and WOLA-OFDM for different WLs are shown in Figure 4.17 (a) and (b). It can be observed that the PSD for WLs of 16 and 32 are almost identical, while there is significant degradation when WL is 8. Thus, it is possible to reduce the WL to 16 without compromising on the PSD performance.

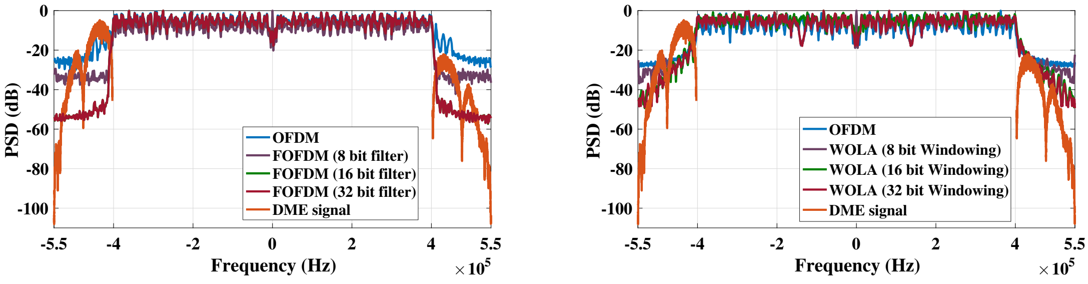

(a) (b)

Figure 4.17: The PSD comparison of different fixed length implementation of (a) Filter and (b) Windowing.

Next, we also analyzed the PSD performance when WL of the complete transceiver is reduced to 8 and 16 from 32. For illustration, we have shown the

PSD of the OFDM in Figure 4.18. Due to limited space constraints and to avoid repetitive results, we omitted the FOFDM and WOLA-OFDM transceivers. For all the transceivers, we observed that the PSD is almost identical for WL of 16 and 32, but there is significant degradation when WL is reduced to 8.

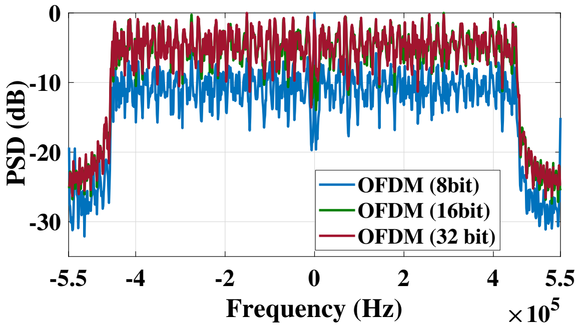

Figure 4.18: The PSD comparison of various waveforms for different WL.

To summarize, we observed that the FOFDM offers superior PSD and hence, lower interference to legacy DME when compared to other transceivers. This allows FOFDM to have wider transmission bandwidth, which is desired for the future air to ground communication. However, better PSD at the cost of poor BER performance is not acceptable for wireless transceivers. Hence, we study the BER performance of various transceivers in the next subsection.

4.4.3 Bit Error Rate Comparison

For BER analysis, we consider end-to-end transceiver with LDACS channels (ENR, APT and TMA), DME interference, and RF impairments due to the AFE. We consider two transmission bandwidths: 1) 732 kHz and 2) 498 kHz. All BER results are obtained from hardware with at least 1000 frames of data.

As shown in Figure 5.6, FOFDM offers better BER performance than OFDM and WOLA-OFDM for a wide range of SNRs. This is mainly due to the ability of FOFDM to reduce the effect of DME interference due to inherent filtering operation at the transmitter and receiver. Note that though BER performance of WOLA-OFDM and OFDM is acceptable for 732 kHz, they cannot be deployed due to severe interference to DME.

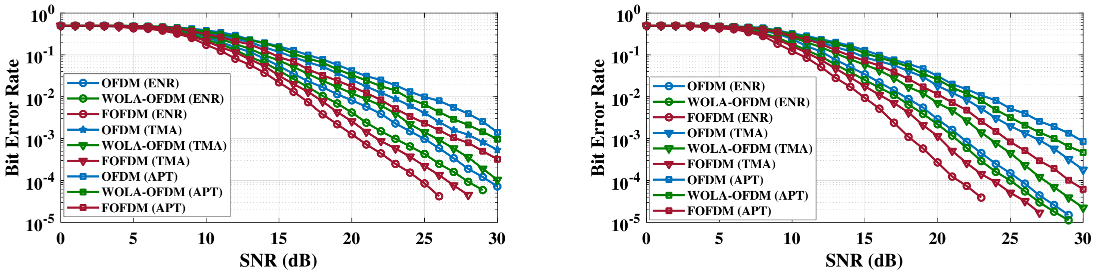

(a) (b)

Figure 4.19: The BER comparison of various waveforms for two transmission bandwidths, (a) 732kHz, and (b) 498kHz and three different channels.

Similar to PSD analysis, we compare the BER performance for three different WLs, 32, 16, and 8. As shown in Figure 4.20, BER performance degrades with the decrease in WL for all the transceivers. However, FOFDM offers significantly better performance than others. In fact, the BER of FOFDM with WL of 16 is significantly better than that of WOLA-OFDM with WL of 32. Similarly, the BER of FOFDM with WL of 8 is significantly better than that of OFDM and WOLA-OFDM with WL of 32 and 16, respectively.

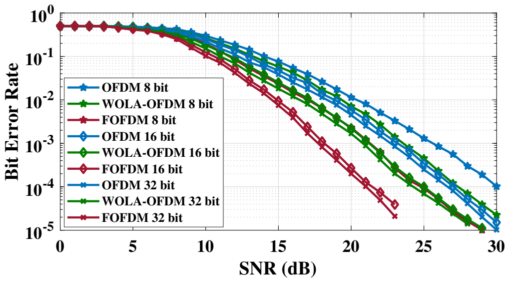

Figure 4.20: The BER comparison of various waveforms for different fixed lengths.

Next, we study the effect of WL of windowing and filtering blocks on the BER. Since the PSD and BER performance of transceivers with the WL of 16 and 32 are comparable, we have used the transceiver with WL of 16 for the results shown in Figure 4.21. It can be observed that the FOFDM with filtering operation using WL of 16 and 32 offers similar performance while its performance degrades when the WL is reduced to 8. The same trend is also observed for WOLA-OFDM. Thus, the selection of WL is an important criterion for transceiver, and higher WL may not guarantee a higher gain in performance.

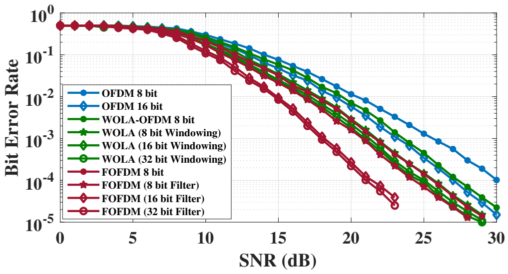

Figure 4.21: The BER comparison of various waveforms for different fixed lengths of filter and windowing operation.

In terms of BER and PSD, FOFDM not only offers better performance but also leads to higher transmission bandwidth. However, this gain in performance should not come at a high cost in terms of complexity. To analyze this, we present the area and power complexity of these transceivers in the next subsection.

4.4.4 Resource Utilization and Power Consumption

In this subsection, we compare the resource utilization and power consumption of the proposed OFDM, WOLA-OFDM, and FOFDM architectures for ten dif-

Parameter	**Waveform**	**V2**	**V3**	**V4**	**V5**	**V6**	**V7**	**V8**	**V9**	**V10**
No. of Flip-Flops	OFDM	N/A	14200 (3.25%)	N/A	31617 (7.21%)	31945 (7.29%)	32628 (7.45%)	33982 (7.75%)	37738 (8.61%)	38193 (8.72%)
	WOLA-OFDM	N/A	14200 (3.25%)	23018 (5.26%)	33015 (7.54%)	34785 (7.93%)	38254 (8.75%)	41945 (9.58%)	43015 (9.83%)	44971 (10.02%)
	FOFDM	10100 (2.31%)	29954 (6.84%)	N/A	37285 (8.51%)	39120 (8.92%)	40015 (9.13%)	41184 (9.40%)	44015 (10.04%)	46253 (10.56%)
No. of DSP48	OFDM	N/A	534 (59.33%)	N/A	570 (63.33%)	570 (63.33%)	570 (63.33%)	570 (63.33%)	570 (63.33%)	570 (63.33)
	WOLA-OFDM	N/A	534 (59.33%)	554 (61.56%)	570 (63.33%)	570 (63.33%)	570 (63.33%)	570 (63.33%)	570 (63.33%)	570 (63.33%)
	FOFDM	296 (32.89%)	785 (87.22%)	N/A	812 (90.22%)	812 (90.22%)	812 (90.22%)	812 (90.22%)	812 (90.22%)	812 (90.22%)
No. of LUT as Memory	OFDM	N/A	396 (0.56%)	N/A	865 (1.23%)	881 (1.25%)	918 (1.30%)	922 (1.31%)	941 (1.34%)	994 (1.35%)
	WOLA-OFDM	N/A	396 (0.56%)	685 (0.972%)	940 (1.34%)	945 (1.35%)	972 (1.38%)	982 (1.39%)	1050 (1.48%)	1102 (1.56%)
	FOFDM	64 (0.09%)	411 (0.583%)	N/A	894 (1.27%)	913 (1.29%)	936 (1.32%)	943 (1.34%)	964 (1.37%)	1021 (1.44%)
No. of LUT as Logic	OFDM	N/A	22083 (10.10%)	N/A	31687 (14.50%)	31985 (14.63%)	32555 (14.89%)	33509 (15.328%)	35509 (16.24)	36657 (16.77%)
	WOLA-OFDM	N/A	22083 (10.10%)	30513 (13.96%)	33218 (15.195%)	34824 (15.96%)	36156 (16.54%)	37599 (17.20%)	41621 (19.04%)	44376 (20.30%)
	FOFDM	5350 (2.45%)	25361 (11.61%)	N/A	32811 (15.01%)	34495 (15.78%)	35391 (16.19%)	37052 (16.95%)	40660 (18.60%)	42539 (19.46%)
No. of MUXes	OFDM	N/A	35	N/A	683	745	1144	1217	1882	1930
	WOLA-OFDM	N/A	35	872	1254	1501	1784	1835	2575	2725
	FOFDM	25	57	N/A	835	1152	1401	1523	1985	2102
Dynamic Power in Watt	OFDM	N/A	0.045	N/A	0.285	0.295	0.297	0.299	0.301	0.304
	WOLA-OFDM	N/A	0.073	0.161	0.294	0.296	0.299	0.301	0.302	0.306
	FOFDM	0.112	0.205	N/A	0.434	0.493	0.494	0.496	0.500	0.509

Table 4.3: Resource utilization and power consumption of transceiver on ZSoC.

ferent configurations. Since the bandwidth of the transceiver is tunable, the results are shown in Table 4.3 corresponds to 732 kHz bandwidth, which has higher complexity than 498 kHz bandwidth. To begin with, we consider the WL of 16 in Table 4.3. All results are obtained after realizing the transceiver on

ZC706.

As shown in Table 4.3, the comparison is made in terms of the number of flip-flops, DSP48 (embedded multipliers), look-up-table (LUT) for memory, LUT for logical and arithmetic operations, multiplexers and dynamic power consumption of the PL. The static power consumption of PS (1.566 W) and PL (0.247W) is, as expected, identical for all configurations and hence, not shown in the table.

Since V1 configuration is realized completely in PS, PL resource utilization results are omitted. In V2, FOFDM resource utilization is due to the filtering block realized in PL. As expected, multiply-accumulate operations in the filter are mapped to DSP48 to get the best possible performance. In V3, preamble addition and detection block is moved to PL, and due to in-built auto-correlation operations, it is one of the most complicated block as evident from the increase in the resource utilization compared to V2. Similarly, a significant increase in resource utilization and power consumption is observed in V5, where FFT/IFFT is moved from PS to PL.

To summarize, FOFDM incurs 27% higher DSP48 than others due to MAC-based filtering, which can be shifted to LUT if needed. For example, windowing operation in WOLA-OFDM is realized using a combination of DSP48 and LUTs. The utilization of the rest of the resources is almost identical in all three waveforms. The IFFT/FFT block consumes the highest power, followed by filtering in the FOFDM. Due to limited space constraints, we have skipped some results. For completeness of the discussion, we briefly mention the observations: 1) The power consumption of the FOFDM increases slightly if we reduce the number of DSP48 at the cost of LUT as logic, 2) Resource utilization and power consumption increases with the rise in the WL, 3) The process of pipelining the transceiver architecture involves addition of registers at the appropriate locations so as to reduce the critical path delay. The reduction in critical path delay allows the transceiver to be clocked at higher frequency. Thus, pipelining offers trade-off between resource (number of FFs) utilization and clock period. For instance, the critical path delay with and without pipelining for OFDM, WOLA-OFDM and FOFDM transceivers are {9.75 ns, 10.25 ns, 12.5 ns}and {259 ns, 265.83 ns, 271.23 ns}, respectively. Furthermore, pipelining incurs additional latency due to newly added registers [87].

In Figure 4.21, we discussed the effect of WL of filter coefficients in the filtering block of FOFDM on BER. In the case of resource utilization, we observed the increase in the utilization with WL, as shown in Figure 4.22. For WOLA-OFDM, different WL of windowing coefficients is not feasible for air to ground communications due to poor PSD and BER performance.

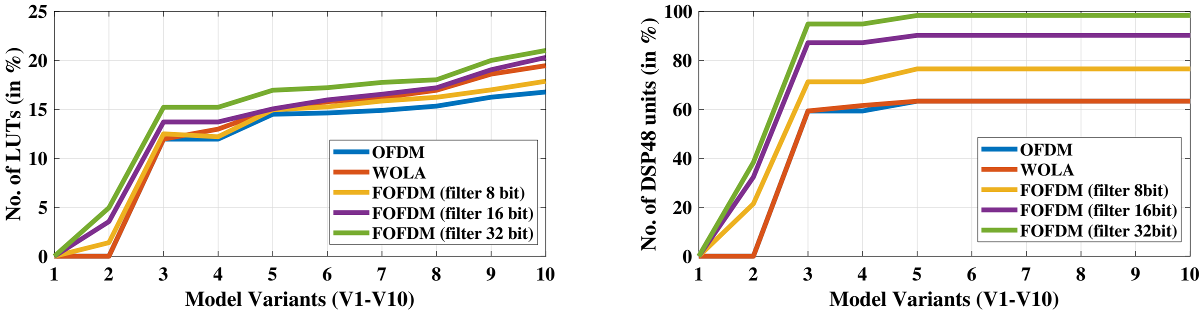

(a) (b)

Figure 4.22: Analysis of resource utilization on ZC706 for different model variants and fixed lengths, (a) Number of LUTs and (b) Number of DSP'48 units.

The above-discussed results show that the FOFDM offers better sidelobe attenuation and better BER performance in trade-off to resource utilization. Filter designed by considering 8 bit fixed WL performs worse than 16/32 bit filter in terms of PSD and BER but better in terms of resource utilization. The FOFDM has a higher usage of resources compared to OFDM and WOLA-OFDM but still uses less than 50% of the Zynq ZC702 resources except for DSP48. This makes the FOFDM as an appealing substitute to the future air to ground communication.

4.5 Summary

In this chapter the detailed performance and complexity analysis of various candidate waveforms for LDACS on Zynq System on Chip (ZSoC) platform is presented. The evaluation board ZC706 Zynq-7000 XC7Z045 of programmable logic (PL) such as FPGA and processing system (PS) such as ARM is used for prototyping. The requirement of hardware and tools to implement the models on ZSoc along with the thorough details on the OFDM, FOFDM and WOLA-OFDM transceiver architecture is discussed in Section 4.1. Apart from this, Seven configuration of of the architecture are realized by dividing it into two sections, one for PL and other for PS.

The Hardware-Software co-design approach is explained in detail which provides the flexibility to choose which part of the transceiver to implement on programmable logic (PL) such as FPGA and which on processing system (PS) such as ARM to meet the given area, delay and power constraints. Detailed experimental results demonstrate the trade-off between these waveforms with respect to parameters such as, area, delay and power requirements. The PSD and BER results in presence of DME interference shows that FOFDM perform better than OFDM and WOLA-OFDM.

The use of filtering leads to increase in area, power and delay complexity. To solve the complexity aspect of FOFDM transceivers especially for deployment onboard aircrafts, as onboard aircraft systems are battery-powered, reducing the LDACS PHY complexity is an essential step towards extending the battery life. We present an in-depth performance analysis of end-to-end low complexity reconfigurable filtered- OFDM (LRef-OFDM) transceiver on heterogeneous Zynq System on Chip (ZSoC) platform in the next chapter. The implementation and analysis is done considering the proposed LDACS PHY specifications and frame structure discussed in Chapter 3.

Chapter 5

Design and Implementation of Low Complexity Reconfigurable Filtered-OFDM

In this chapter, we focus on the complexity aspect of FOFDM transceivers especially for deployment onboard aircrafts, along with in-depth performance analysis of end-to-end LDACS transceiver on heterogeneous ZSoC platform consisting of FPGA and ARM processor. As onboard aircraft systems are battery-powered, reducing the LDACS PHY complexity is an essential step towards extending the battery life. Specifically, we propose a novel interpolation and masking based multi-stage digital FIR filter that when integrated with LDACS transceiver, not only meets the stringent non-uniform spectral attenuation requirements of LDACS but also allows variable transmission BWs up to 732 kHz.

5.1 Proposed Filter Design

In this section, we focus on the design of the low complexity BW-reconfigurable digital FIR filter in Figure 5.1 and the aim is to meet the OOB attenuation specifications of LDACS for a wide range of transmission BWs. Please refer to the Chapter 3 and 4 for the LDACS specifications and the design details of other baseband blocks of the transceiver implementation on the ZSoC testbed, respectively.

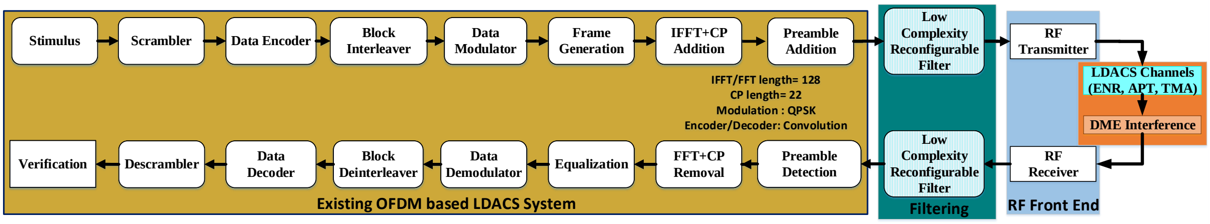

Figure 5.1: Building blocks of the proposed LRef-OFDM transceiver along with end-to-end testbed.

The proposed filter employs the interpolation operation [38, 43, 88] to reduce the complexity. In this operation, if the coefficients of a lowpass prototype filter are interpolated by a factor M, every unit delay in the filter is replaced by M delays. This results in a multi-band frequency response with sub-bands located at even multiples of $\frac{\pi}{M}$, each having its passband and transition BW $\frac{1}{M}$ times that of the prototype filter. The interpolated frequency response can be given by:

$$H_{Ip}(z) = \sum_{n=0}^{\frac{N}{2}-1} h_n[z^{-Mn} + z^{-M(N-n)}] + h_{\frac{N}{2}} z^{\frac{-Mn}{2}} \tag{5.1}$$

where, $h_0, h_1 \ldots h_{\frac{N}{2}}$ are the unique filter coefficients of an N^{th} order FIR filter. In proposed filter design approach [25], three sub-filters denoted as Filter I, Filter II, and Filter III are cascaded and illustrative frequency responses are shown in Figure 5.2. If $H_I(z)$, $H_{II}(z)$, $H_{III}(z)$ denote the z-domain representations of sub-filters, the resultant filter is given as,

$$H(z) = H_I(z).H_{II}(z).H_{III}(z) \tag{5.2}$$

The LDACS signal is over-sampled by a factor of four to assist in interference reduction [15]. Therefore, as the LDACS BW is approximately 500 kHz, the sampling frequency for our filter is chosen as 4 MHz. Figure 5.2 shows the frequency responses of three sub-filters designed for a transmission bandwidth of 498 kHz on the frequency scale normalized with respect to Nyquist frequency, i.e., half of sampling frequency. The sub-filter design is explained below:

A1. *Filter I:* The stage I filter is designed with minimum order $(N = 26)$ satisfying the stringent spectral mask, and has passband edge (Fp_1) as $M(= 4)$ times of the passband edge of the LDACS signal (Fp_s) based on its transmission BW, i.e, $Fp_1 = 4 * Fp_s$. Similarly the stopband edge (Fs_1) is $4 * Fs_s$, where Fs_s is the stopband edge of the LDACS signal. As the most relaxed required attenuation level is adjacent to the passband, this sub-filter is designed with the most relaxed attenuation specification. The filter response for this stage I filter $H_I(z)$ is obtained by substituting the value of I and N in (5.1),

$$H_I(z) = \sum_{n=0}^{12} h_n[z^{-4n} + z^{-4(26-n)}] + h_{13}z^{-2n} \tag{5.3}$$

A2. *Filter II:* This sub-filter removes the unwanted central subband from the frequency response of interpolated Filter I. This filter is designed with order 26 having interpolation factor (M) of 2, and the filter response $H_{II}(z)$ can be expressed as,

$$H_{II}(z) = \sum_{n=0}^{12} h_n[z^{-2n} + z^{-2(26-n)}] + h_{13}z^{-n} \tag{5.4}$$

The passband and stopband edge frequencies of Filter II are based on the resultant edge frequencies in the interpolated frequency response of Filter I and can be represented as $Fp_2 = \frac{F_m}{2}$ and $Fs_2 = 1 - Fp_2$ respectively, where F_m is a reference frequency whose value is chosen based on the supported transmission BWs.

A3. *Filter III:* This sub-filter has order 14 and removes the unwanted highpass subband from the cascaded frequency response of Filter I and Filter II, i.e., $H_I(z).H_{II}(z)$. The passband and stopband edge frequencies for Filter III are based on the resultant edge frequencies in the cascaded frequency response and can be represented as $Fp_3 = \frac{F_m}{4}$ and $Fs_3 = 1 - Fp_3$ respectively. It has the most relaxed transition BW and the most stringent stopband attenuation specification among the three sub-filters. The frequency response of this filter $H_{III}(z)$ can be represented as,

$$H_{III}(z) = \sum_{n=0}^{6} h_n[z^{-n} + z^{-(14-n)}] + h_7 z^{\frac{-n}{2}} \tag{5.5}$$

Here, we mainly focus on the filter design, and the details regarding the complete transceiver are included in an appendix document as supplementary

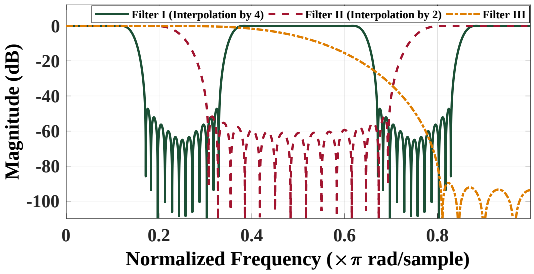

Figure 5.2: Frequency responses of sub-filters $H_I(z)$, $H_{II}(z)$, $H_{III}(z)$ and the resultant filter $H(z)$ for 498 kHz LDACS transmission BW.

material [89].

In Chapter 3 and 4, we showed that LDACS can have additional bandwidths of 342 kHz, 654 kHz, 732 kHz by maintaining compatibility with the existing frame structure of 498 kHz. To realize a BW reconfigurable transceiver, we store the unique filter coefficients corresponding to all four BWs in memory. We can thus support different transmission BWs on the fly by just selecting appropriate filter coefficients from memory at run-time. This would require a memory component with storage capacity of 144 coefficients: 14*4 (Filter I with order 26) + 14*4 (masking Filter II with order 26) + 8*4 (masking Filter III with order 14). However, to reduce this requirement, we design and use the same masking filters (Filter II and III) for all the BWs, and they are designed as halfband FIR filters to minimize the number of distinct non-zero coefficients. Based on the design of Filter I, a reference frequency F_m is computed and the passband and stopband edge frequencies of Filter II and Filter III are chosen based on F_m. The reference frequency F_m is selected based on the supported transmission BWs and is chosen to be the stopband edge frequency of Filter I corresponding to the widest supported transmission BW. As a result, we can use the same masking filters II and III for all BWs and the total required memory storage capacity is just 67 coefficients: 14*4 (Filter I with order 26) + 7 (halfband masking Filter II with order 26) + 4 (halfband masking Filter III with order 14). The overall filter responses for all four transmission BWs satisfying the corresponding LDACS spectral masks are shown in Figure 5.3. Note that the LDACS spectral mask in [90] is considered for BWs 342 kHz and 498 kHz, and an appropriately modified version is considered for other BWs.

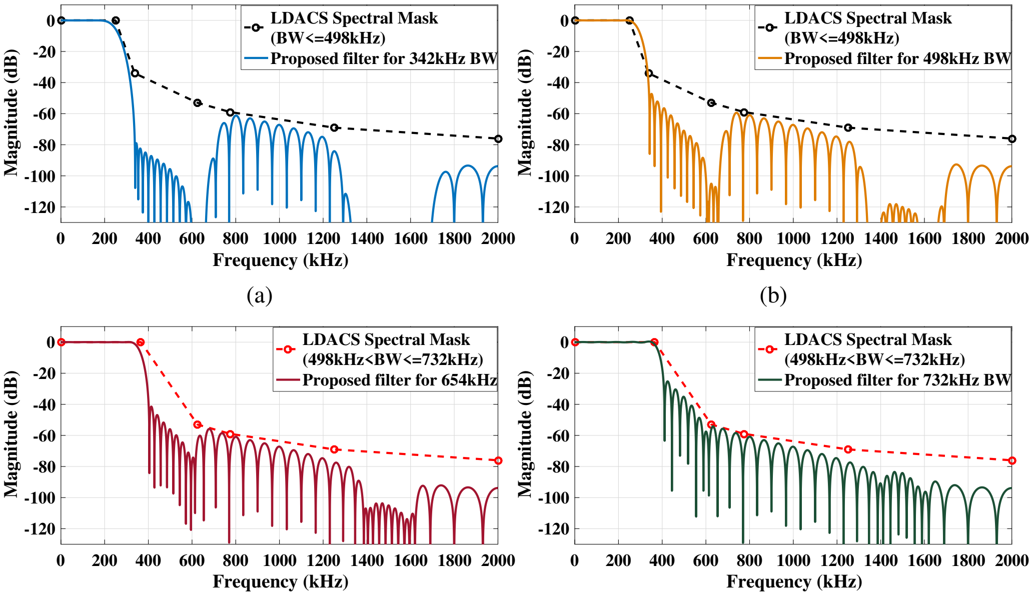

(a) (b)

(c) (d)

Figure 5.3: Overall frequency response characteristics of the proposed filter for the bandwidths: (a) 342 kHz (b) 498 kHz (c) 654 kHz (d) 732 kHz.

It is empirically computed that among the different possible combinations of interpolation factors, the lowest overall filter complexity (in terms of total number of unique multipliers) is obtained using the interpolation factors 4, 2, 1 respectively for the three sub-filters [89]. The design parameters of the three sub-filters for the different transmission BWs are listed in Table 5.1 (normalized with respect to Nyquist frequency). Except for Fp_1 and Fs_1, which are set according to the transmission BW, all other filter design specifications are identical for all the BWs. MATLAB is used to obtain coefficients of the three sub-filters corresponding to the design parameters listed in Table 5.1.

Parameters	**Filter I**				**Filter II**	**Filter III**
	342 kHz	**498 kHz**	**654 kHz**	**732 kHz**		
Order (N)	26	26	26	26	26	14
Passband Freq.	0.3418	0.498	0.6543	0.7324	0.3975	0.1988
Stopband Freq.	0.6724	0.6724	0.795	0.795	0.6025	0.8013
Attenuation (dB)	-70.5	-37.9	-31.5	-14.5	-43.1	-81.8
Interpolation M	4	4	4	4	2	1

Table 5.1: Filter design specifications for different LDACS transmission BWs

From Table 5.1, Figure 5.2, and Figure 5.3, it can be noted that although the attenuation specifications of the different sub-filters are relaxed, the overall cascaded non-uniform frequency responses satisfy the stringent LDACS spectral masks for each transmission BW. This idea of using sub-filters with different relaxed attenuation specifications and thus, lower complexity is a unique feature of this work.

Satisfying the stringent spectral mask specifications [25] should not come at the cost of large delay and high implementation complexity that will also affect the overall power consumption. To understand the filtering complexity, we compare the multiplication complexity (total number of unique multipliers) and group delay of the proposed filter with the FIR filters designed for 498 kHz BW using various state-of-the-art approaches: 1) Parks-McClellan (PM) algorithm (Chapter 4), 2) Least squares (LS) technique [91], 3) Traditional interpolated FIR (IFIR) technique (wherein two sub-filters are cascaded with only the first subject to interpolation) [88], and 4) Generalized IFIR technique (wherein more than two sub-filters can be cascaded with multiple out of those subject to interpolation) [92].

The total number of multipliers involved in the proposed filter is the sum of the multipliers required to implement the three sub-filters. It can be noted that while implementing the FIR sub-filters, the symmetry of their coefficients can be exploited such that only half of the coefficients need to be implemented, using the transposed direct-form FIR filter architecture [93]. Also, for halfband FIR filters (sub-filters II and III in our case), every alternate coefficient is zero, and the central coefficient is always 0.5, which can be implemented simply with a logical shift operation. Exploiting these properties, sub-filters I, II, and III in the proposed LRef-OFDM can be implemented using 14, 7, and 4 multipliers respectively and the total number of multipliers required is thus 25. As the three sub-filters are cascaded, the group delay of the proposed filter is the sum of the group delays of sub-filters I, II, and III. The total group delay of the proposed filter is thus (13x4) + (13x2) + (7x1) = 85 samples. In units of time, this corresponds to 21.25 μs as the sampling frequency is 4 MHz. The group delay in units of time can be calculated as $totalgroupdelay(samples)/samplingfrequency$. The total number of required multipliers and group delays are similarly calculated for different state-of-the-art filters that can be used in the FOFDM, and the comparative analysis is presented in the Table 5.2.

We can observe from Table 5.2, that the proposed filter offers 75.25%, 45.65%, 34.21% and 66.67% reductions in multiplication complexity and 15%, 23.08%, 35.11% lower and 14.87% higher group delay when compared to the filters designed using the PM algorithm, traditional IFIR technique, generalized IFIR

Filters based on	Number of Multipliers	Group Delay	
		In samples	In μs
PM algorithm (Chapter 4)	101	100	25
LS technique [91]	75	74	18.5
Traditional IFIR [88]	46	110.5	27.625
Generalized IFIR [92]	38	131	32.75
Proposed Filter	25	85	21.25

Table 5.2: Complexity and group delay comparison

technique, and LS technique respectively.

A detailed comparison analysis of end-to-end LDACS transceivers in terms of PSD, BER, and hardware resource utilization is presented in the next section.

5.2 Performance Analysis on ZSoC Testbed

For performance analysis, the proposed filter is integrated with our end-to-end LDACS transceiver realized on the Xilinx Zynq ZSoC ZC706 platform, and the sample rate is set to 4 MHz. This is accomplished using MATLAB hardware description language (HDL) Coder and Verifier Toolboxes. Please refer to Chapter 4 for additional implementation details. Next, the transceiver is integrated with RF front-end for performance analysis in a real radio environment. The RF front-end is designed using building blocks of the MATLAB RF Toolbox. At the transmitter, RF front-end consists of digital up-converter, analog filtering, power amplifier, followed by the RF transmission. The transmission frequency can be set to anywhere in the L-band (960-1164 MHz) and it is set to 985 MHZ for the results discussed here. At the receiver, we need low-noise amplifier, analog filtering, and digital down-converter to get the desired baseband signal. Since RF front-end introduces phase noise, additional pilot reference signal based phase correction is added. The output of the phase correction block is passed to the proposed filter followed by baseband signal processing, as shown in Figure 5.1.

5.2.1 Power Spectral Density (PSD) Comparison

In Figure 5.4, we present the PSD comparison of OFDM, FOFDM, and LRef-OFDM transceivers implemented using 16 bit WL. The LRef-OFDM and FOFDM offer higher OOB attenuation than OFDM. Higher OOB attenuation leads to lower interference to legacy DME signals as well as enables wider transmission BW of up to 732 kHz compared to only 498 kHz in existing LDACS. This results in around 50% improvement in the spectrum utilization.

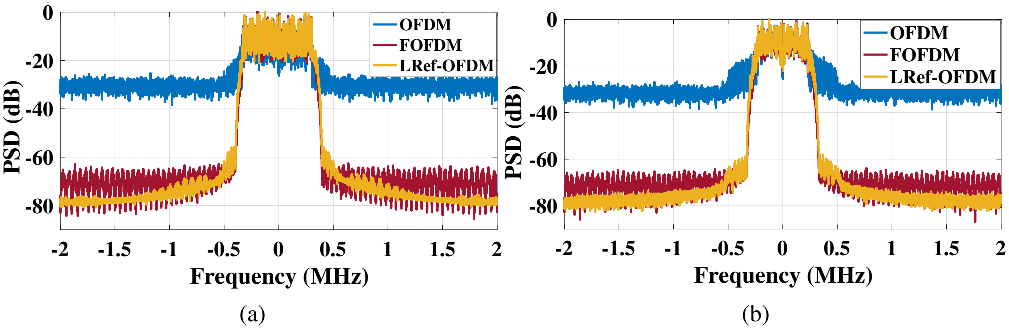

Figure 5.4: The PSD comparison of various waveforms for two different signal BWs, (a) 732 kHz, and (b) 498 kHz and three different channels.

Next, we study the effect of WL on the PSD. To understand the impact of varying WL settings for the filter as well as the complete transceiver, we consider two scenarios: (1) Proposed filter with WL of {8,16,32} bits and rest of the transceiver blocks with WL of 16 bits, and (2) Complete transceiver with the WL of {8,16,32} bits. Due to space constraints and to avoid repetitive results, we consider only LRef-OFDM in Figure 5.5a and Figure 5.5b. In both scenarios, it can be observed that the PSD is almost identical for WL of 16 and 32 bits. However, the PSD degrades substantially when the WL of the entire transceiver is reduced to 8 bits, as shown in Figure 5.5b. The interpretation of these results can be stated as the LRef-OFDM system can even be implemented with lower filter WL to meet the application-specific complexity constraints. Similar results are also observed for FOFDM, while the OFDM needs minimum WL of 16 bits for a complete transceiver.

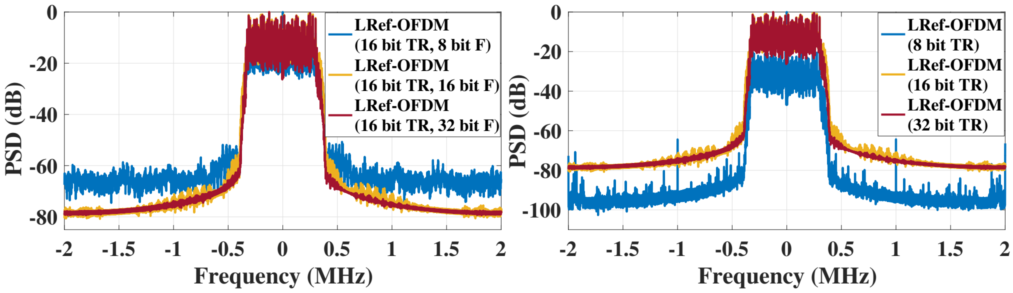

(a) (b)

Figure 5.5: PSD comparison of different WLs in LRef-OFDM. Note: TR and F in the legends refer to transceiver and filter respectively.

5.2.2 Bit Error Rate (BER) Comparison

Next, we analyze the BER performance in the presence of three wireless channels: enrouting (ENR), airport/taxi (APT), and terminal maneuvering area (TMA). Compared to simulation-based BER discussed in Chapter 3, our analysis considers the effect of interference from legacy DME signals, impairments due to RF front-end, and different WLs. The BER analysis is done for two different signals BWs, 732 kHz and 498 kHz, and corresponding plots are shown in Figure 5.6a and Figure 5.6b respectively. It can be observed that LRef-OFDM does not have any significant degradation in BER when compared with FOFDM as both employ filtering to improve OOB attenuation and to reduce the interference from DME. The errors due to RF front-end are mitigated via a phase correction block. As expected, BER of OFDM suffers due to severe interference from DME, and its transmission BW has thus been limited to 498 kHz.

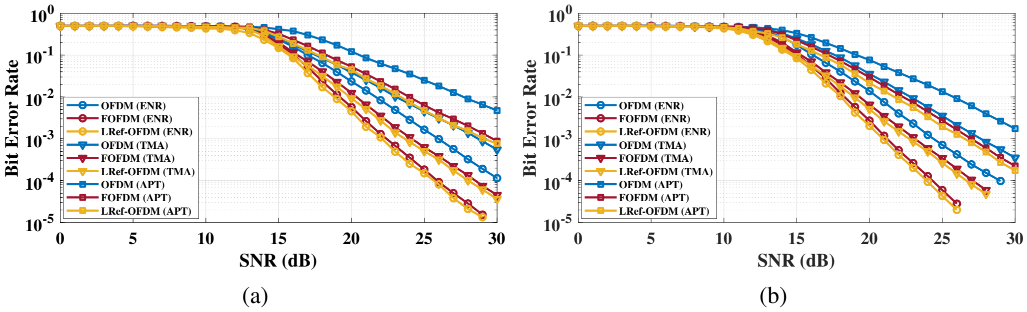

Figure 5.6: The BER comparison of transceivers for three different LDACS channels and two different signal BWs, (a) 732 kHz, and (b) 498 kHz.

In Figure 5.7, we study the effect of WL on the BER performance of the LDACS transceiver. Similar to the PSD analysis, we consider two scenarios. With the decrease in WL of the filter and transceiver, the BER degrades. It can be observed that the WL of 8-bit may not be a good choice for the transceiver. However, we can have 16-bit transceiver with 8-bit filter, which also offers acceptable PSD performance. A similar analysis can be performed for each transceiver block, thereby reducing the complexity significantly without compromising on the BER and PSD. Thus, experimental BER analysis on ZSoC offers insights on the performance in real radio environment, which is otherwise not possible in simulation-based analysis.

The LRef-OFDM thus offers better PSD and BER performance than OFDM. It provides higher spectrum utilization due to wider transmission BW, and support for various BWs can enable LDACS to offer multiple services ranging from

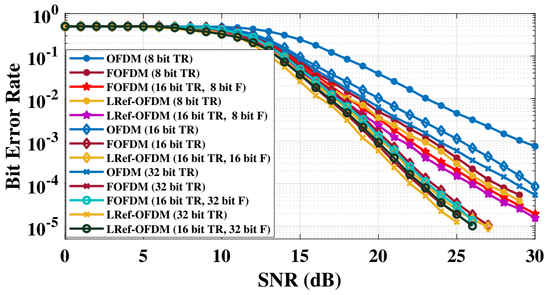

Figure 5.7: The BER comparison of various LDACS transceiver implementations for different fixed-point word lengths.

text, audio, to multimedia. When compared to FOFDM, proposed LRef-OFDM offers identical performance. Next, we compare the complexity of the LDACS transceivers.

5.2.3 Resource Utilization and Power Consumption Comparison

In this subsection, we compare the resource utilization and power consumption of the proposed filter and the PM algorithm based filter implemented on the ZC706. We also compare the same for one variant of the OFDM, FOFDM, and LRef-OFDM transceiver corresponding to 128 point FFT. For a detailed comparison of all the nine transceiver configurations one can refer to [89]. The resource utilization comparison is presented in the Table 5.3.

LDACS Transceiver Type	Resources utilized			
	No. of Flip - Flops	No. of DSP48	No. of LUT as memory	No. of LUT as logic
PM filter	10100 (2.31 %)	296 (32.89 %)	64 (0.09 %)	5350 (2.45 %)
Proposed filter	8921 (2.04 %)	181 (20.11 %)	50 (0.073 %)	4114 (1.89 %)
OFDM transceiver	39501 (9.03 %)	570 (63.33 %)	994 (1.35 %)	37541 (17.23 %)
FOFDM transceiver	47653 (10.89 %)	812 (90.22 %)	1021 (1.44 %)	43439 (19.93 %)
LRef-OFDM transceiver	46394 (9.82 %)	697 (77.44 %)	1009 (1.42 %)	41552 (19.07 %)

Table 5.3: Resource utilization comparison on ZC706

We can observe from the Table 5.3 that the proposed filter utilizes fewer resources than the PM based filter of WL 16 bit, and hence the proposed LRef-OFDM transceiver has lower area requirement than FOFDM transceiver. Also, as expected, the OFDM transceiver shows the least resource utilization due to lack of an extra filtering module.

We also compare the dynamic power for all the transceivers. While LRef-OFDM (0.437 W) consumes 30.43% more power than OFDM (0.304 W), it consumes 14.14 % less power than FOFDM (0.509 W) due to proposed filter design. Additionally, we compare the complexity for different WLs of OFDM and LRef-OFDM transceiver in Table. 5.4.

Resources Utilized	OFDM LDACS		LRef-OFDM LDACS	
	8-bit WL	32-bit WL	8-bit WL	32-bit WL
No. of Flip-Flops	33514 (7.66 %)	51254 (11.72 %)	38421 (8.79 %)	58624 (13.40 %)
No. of LUT as logic	31421 (14.42 %)	47264 (21.69 %)	36283 (16.65 %)	53234 (24.43 %)

Table 5.4: Resource utilization comparison for transceiver's different word lengths on ZSoC ZC706

We observed that resource utilization and power consumption increase with the increase in the WL. To summarize, LRef-OFDM offers better OOB attenuation and BER performance than OFDM, along with lower implementation complexity and power consumption than FOFDM. This makes it an attractive alternative for future air-ground communications.

5.3 Summary

Here, we presented LRef-OFDM using a novel interpolation and masking based filter design approach. The proposed filter is a multi-stage filter designed to meet the stringent non-uniform spectral attenuation requirements of LDACS. The proposed filter is also integrated in our end-to-end LDACS testbed realized using Zynq System on Chip and the performance analysis is done in the presence of L-band legacy user interference as well as wireless channels. With extensive experimental results on a hardware testbed, we validated its superiority over OFDM and FOFDM in terms of PSD and BER performance along with tunable bandwidth. It also offers a lower area and power complexity than FOFDM.

The spectrum is a scarce resource and, thus spectrum sensing is important for future communication systems. Hence, for the systematic use of the spectrum we propose a SNS sensing based L-band spectrum characterization in the next chapter.

Chapter 6

L-Band Spectrum Sensing via Sub-Nyquist Sampling

The proposed LDACS transceiver enables tunable transmission bandwidth and multi-band transmission. For effective deployment of such transceiver, occupancy status of L-band is desired so as to meet the application-specific spectrum resource requirements of all active users. In this chapter, we explore SNS based $L-$band spectrum sensing (LSS) to identify the occupancy status of all legacy users in the L-band. The SNS-based LSS exploits the sparsity of L-band, making the LSS feasible with multiple low-rate and narrowband ADCs compared to expensive Nyquist-rate ADC. We begin with the assumed signal model in the next section.

6.1 Signal Model

We consider L-band (960-1164) as a wideband spectrum. The spectrum is further divided into N number of non overlapping narrowbands of equal bandwidth (B). In time domain, the wideband spectrum can be represented as $x(t)$. The signal $x(t)$ can be represented as,

$$x(t) = \sum_{i=1}^{M} s_i(t) e^{j2\pi f_i t} + n(t) \tag{6.1}$$

Where, M denotes the unknown number of active transmissions at time t such that $M << N$, $s_i(t)$ is the amplitude of the i^{th} active transmission of a carrier frequency f_i and $n(t)$ is the additive white Gaussian noise. It is assumed that each active transmission lies in a freqency band of center frequency f_i.

To perform WSS on $x(t)$, we employed SNS for the digitization. By exploiting the sparse nature of the wideband spectrum, the SNS uses the low rate ADCs to achieve the minimum sampling rate that is less than the Nyquist sampling rate of the sparse wideband spectrum. In wideband spectrum sensing (WSS), we used MWC and FRI sub-Nyquist sampling techniques which do not require prior knowledge of the band locations. However, to reconstruct the wideband signal from the sub-Nyquist samples, WSS should meet the following criteria:

- Sampling rate of low rate ADCs, $f_s ns$ should be higher than the bandwidth of a narrowband, i.e. $f_{sns} \geq B$

- Number of ADCs should be higher than the number of occupied narrowbands. Note that the number of $ADC << N$.

Here, we consider the wideband spectrum as L-band. The spectrum occupancy of L-band is sacrce due to the presence of licensed existing communication and navigation systems as shown in Figure 1.3. While designing the system model for the L-band spectrum to be sensed, the following necessary conditions are considered:

- We consider the wideband signal $x(t)$ to be a band-limited signal and has the lowest and highest band frequency as $960MHz$ and $f_{max} = 1164MHz$ respectively. The band is further divided into $N = 204$ frequency bands. These N frequency bands have uniformly distributed bandwidth $B = \frac{f_{max}}{N} = 1MHz$.
- Each active DME transmission $s_i(t)$ occupies orthogonal frequency bands having $1MHz$ of maximum bandwidth.
- The sparse occupancy status of N frequency bands is generated randomly.

Next, we discuss the SNS techniques applied to sense the vacant bands, followed by the reconstruction method used in this work.

6.2 Sub-Nyquist Sampling

In the last decade, various SNS based wideband spectrum sensing (SNS-WSS) methods [51] have been proposed to overcome the need for high-speed ADCs.

Here, we discuss the two recent SNS techniques: 1) MWC [54], and 2) FRI [55].

6.2.1 Modulated Wideband Converter

The MWC allows a wideband signal to be sampled at a sub-Nyquist rate. In order to reduce the sampling rate by p times, p parallel channels are used in the MWC scheme, as shown in Figure 6.1. Each branch of MWC has a pseudo-random sequence generator, a mixer, an accumulator, and an ADC, as shown in Figure 6.1. In MWC, the pseudo-random sequences (or mixing functions), $m_i(t) \forall i \in [1, p]$, of every branch are uncorrelated periodic sequences of time period $T_p = LT$, where, L is the number of frequency sub-bands into which a wideband spectrum is divided and T is the Nyquist period of $x(t)$. Because of the periodic nature, $m_i(t)$ contains harmonics at rate of $f_p = \frac{1}{LT}$.

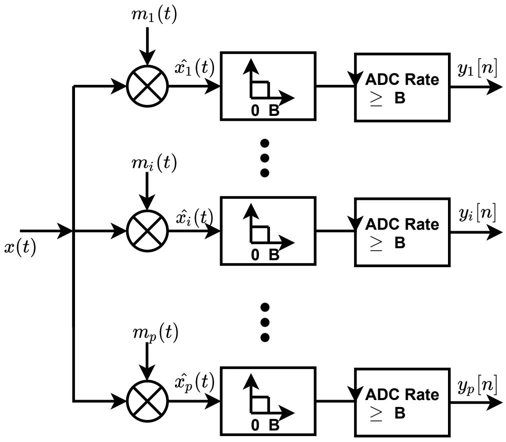

Figure 6.1: Basic architecture of MWC sampler.

The mixing function $m_i(t)$ can be represented mathematically as follows:

$$m_i(t) = \alpha_{ik}, k\frac{T_p}{P} \leqslant t \leqslant (k+1)\frac{T_p}{P}, 0 \leqslant k \leqslant P-1 \tag{6.2}$$

where, $\alpha_{ik} \in +1, -1$ and P is number of ± 1 intervals in each period of $m_i(t)$.

Since, $m_i(t)$ is a periodic function, the fourier expansion can be expressed as:

$$m_i(t) \sum_{l=-\infty}^{\infty} c_{il} e^{j2\pi l f_p t} \tag{6.3}$$

where, $c_{il} = \frac{1}{T_p} \int_0^{T_p} m_i(t) e^{j2\pi l f_p t}$. After mixing, the output signal $\hat{x}(t)$ and it's Fourier transform can be represented as:

$$\hat{x}(t) = x_i(t).m_i(t) \tag{6.4}$$

$$\hat{X}_i(f) = \int_{-\infty}^{\infty} x_i(t) (\sum_{l=-\infty}^{\infty} c_{il} e^{j2\pi l f t}) e^{-j2\pi l f t} dt = \sum_{l=-\infty}^{\infty} c_{il} X_i(f - l f_p) \tag{6.5}$$

The DTFT of mixed demodulated samples generated at the output of MWC ($Y(f)$) is a linear combination of lF_p shifted versions of all L frequency sub-bands and mathematically represented as:

$$Y(f) = A_{mwc} X(f), f \in [-\frac{F_p}{2}, +\frac{F_p}{2}] \tag{6.6}$$

where, A_{mwc} is a $p \times L$ sampling matrix, $X(f)$ is the vector of Fourier transform of L frequency sub-bands. The MWC approach requires lower analog bandwidth ADCs to perform digitization at Sub-Nyquist rate as it uses the mixing function which brings all the frequency bands of a wideband signal spectrum in the baseband. It is suitable only for contiguous wideband spectrum digitization however, in case of $L-$band spectrum, some of the frequency bands are always occupied which means there is no need to digitize such parts of the spectrum. Such non-contiguous SNS can also lead to further reduction in the number of ADCs and their sampling rate. One such technique, namely finite rate of innovation (FRI) is presented next.

6.2.2 Finite Rate of Innovation

The FRI is a non-contiguous WSS approach. The architecture of FRI is similar to the MWC architecture presented in Figure 6.1. The FRI approach digitizes a set of desired frequency sub-bands β, instead of digitizing all L frequency sub-bands. In the L-band scenario, 49 bands are allocated to the legacy users such as DME, JTIDS, MIDS, ACAS, SSR, UAT, etc., as shown in Figure 1.3. The FRI approach significantly reduces the number of ADCs by not using them to sense the 49 bands allocated to legacy users. FRI uses a unique mixing function $m_{if}(t)$, which can be represented as:

$$m_{if}(t) = \sum_{n \in \beta} \alpha_{i,n} e^{-j2\pi f_n t} \tag{6.7}$$

where $\alpha_{i,n}$ is a unique scaling coefficient of the n^{th} band in β. The DTFT of the samples generated at the output of every analog branch is a linear combination of shifted copies of all frequency sub-bands present in β. The output of the FRI $Y(f)$ can be shown as follows:

$$Y(f) = A_{fri} X_{\beta}(f) \tag{6.8}$$

Where, $X_{\beta}(f)$ represents $|\beta| \times 1$ vector which contains Fourier transform of β frequency sub-bands and A_{fri} is a $p \times |\beta|$ matrix containing $\alpha_{i,n}$ as its $(i,n)^{th}$

entry.

The main difference between MWC and FRI approach is that the MWC senses the entire wideband spectrum while FRI only senses the bands which are not allocated to the legacy users which reduces the sensing failure rate. To support this, FRI has a different and unique mixing function.

6.2.3 Reconstruction

SNS is followed by spectrum reconstruction. There are two assumptions to reconstruct the sampled signal. Firstly, the input signal must be sparse, and it means that there are only a few narrow sub-bands, which contain information inside the wide-input signal. Secondly, all components of the SNS system, such as mixers and filters, are assumed to be ideal.

Fulfilling the second assumption is impossible as there is neither ideal output of the analog components nor a very high order of filter to be deployed to approximate the ideal output. A reconstruction algorithm is applied to the SNS system output to recover the signal corrupted by noise fully.

Here, we use compressive sensing-based OMP [58, 59] algorithm for sparse recovery of the original signal. OMP is an iterative greedy algorithm that uses the band selection criterion in the matching pursuit algorithm and processes the selected band orthogonally using the Gram-Schmidt orthogonalization method. Then it projects the signal formed by these orthogonal bands on the space to obtain the original signal. The OMP received significant attention due to its low complexity and simple geometric interpretation.

OMP finds the support (S) of n-sparse signal u. A vector u is called n-sparse if u contains upto n non zero entries. The OMP implementation steps are as follows:

- Step1: Take the input to the OMP as compressive sensing matrix A and measurement vector y.
- Step2: Initialize the approximation of the signal vector $\hat{u}$ equivalent to 0 and residual $r = y$.
- Step3: Normalize the rows of the sensing matrix A, calculate the residual $r_i = y - A\hat{u}_i$ and update the residual in each iteration i.
- Step4: Find the updating vector V from the residual $V_i = A^T r_{i-1}$.
- Step5: Find the index k_{max} of the column in A which is maximal correlated with the residual r using the updating vector V.
- Step6: Update the support vector S_i by using k_{max}.

OMP recovers the one index of support vector S at a time in n steps. Once the support vector S is found correctly, the approximation of the signal vector $\hat{u}$ is updated to minimize $||y - Au||_2$, The updating is done in each iteration using $\hat{u}_i|_{S_i} = A^{\dagger}y$. Once the stopping criteria is fulfilled, the $\hat{u}$ stops updating.

Next, we present the simulation results considering the L-band scenario.

6.3 Results

Here, we compare the performance of MWC and FRI sub nyqist sampling techniques to sense the presence of the DME signals. The performance analysis is done by comparing the probability of detection of occupied bands along with the sensing failure and throughput. All the results are taken considering the above explained L-band scenario.

6.3.1 Probability of Detection Comparison

The probability of detection of occupied bands is calculated on the basis of number of correctly sensed bands. Here, the probability of detection for MWC sampling is shown in Figure 6.2 and analyzed for different values of ADCs and four SNR levels. The plot in Figure 6.2 shows that the number of correctly sensed bands is directly proportional to the number of ADCs and after a particular value of ADCs, the probability of detection saturates to 1. This means we sense all the occupied bands correctly. Additionally, as we increase the SNR level, we will need lesser ADCs to sense all the bands correctly.

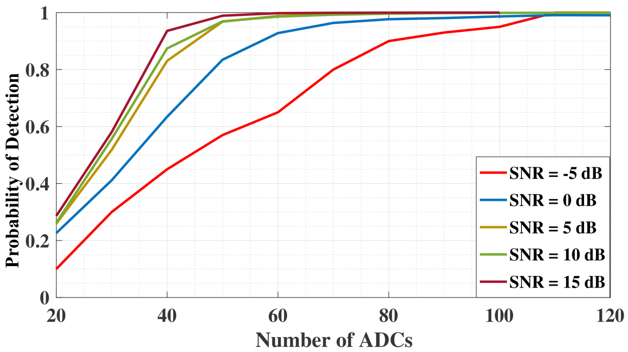

Figure 6.2: Probability of detection for MWC sensing technique with different SNR values.

We also compare the probability of detection of the two sampling techniques : 1. MWC and 2. FRI while using OMP as a sensing technique to sense the occupied DME bands. As shown in Figure 6.3, the FRI reports better recovery success than MWC as FRI does not sense the bands which are pre-occupied by the other legacy users such as SSR, UAT, JTIDS, MIDS etc. in L-band.

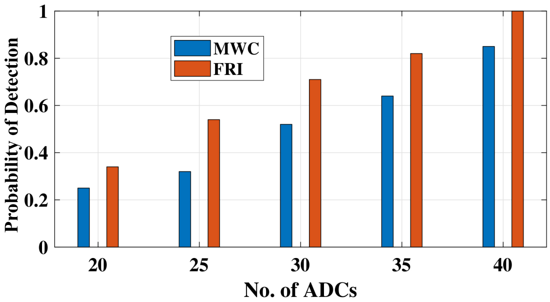

Figure 6.3: Comparison for probability of detection of MWC and FRI with different no of ADCs.

Next, we compare the sensing failure and throughput for the two sensing techniques.

6.3.2 Sensing Failure

Here, we compare the sensing failure and average throughput for MWC and FRI sampling techniques. The sensing failure occurs when the number of occupied bands N is greater than the number of ADCs(M_{adc}) ($N > M_{adc}$). Figure 6.4 (a) and (b) shows the occurrence of sensing failure at different number of ADCs for SNR=10dB and 20dB respectively. The results also consider that the number of occupied bands are chosen randomly. We can observe from the figures that MWC has higher sensing failure than FRI in both the cases. Also, while increasing the SNR value, the overall sensing failure decreases.

Figure 6.5 shows the normalized throughput comparison for MWC and FRI

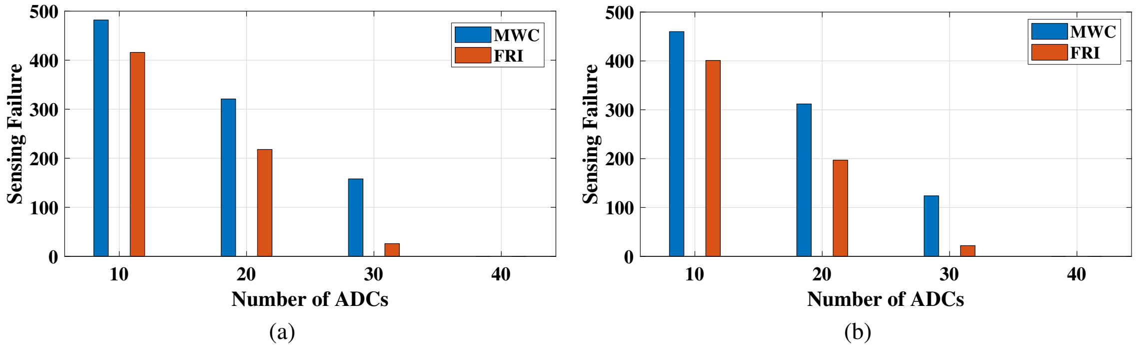

Figure 6.4: Sensing failure comparison of MWC and FRI for two SNR levels (a) SNR=10dB (b) SNR=20dB.

sampling techniques. Here, the throughput is defined as the number of vacant bands available in the sensed spectrum and it is normalized with the total number of narrowbands ($N = 204$). The simulation results show that the throughput value increases with the increase in SNR. FRI offers higher throughput than MWC as MWC has more number of sensing failures at the lower number of ADCs (M_{adc} = 20) while MWC has higher throughput at a higher number of ADCs (M_{adc} = 40), as the sensing failure in MWC is negligible in that case.

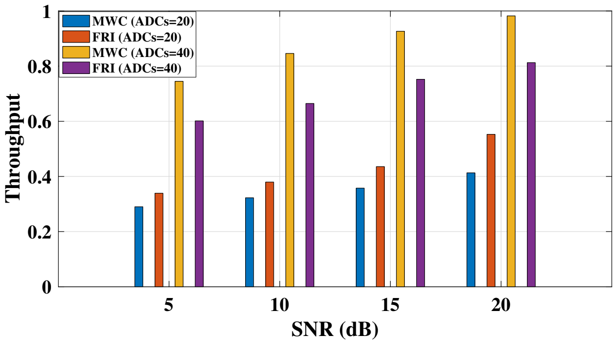

Figure 6.5: Comparison for throughput of MWC and FRI with variable SNR for number of ADCs= 20 and 40.

To summarize, We can say that the FRI offers better probability of detection, higher throughput (at lower number of ADCs) and fewer number of sensing failures than MWC and requires lower number of ADCs due to non-contiguous sensing.

6.4 Summary

In this chapter, a SNS based L-band spectrum characterization for future air to ground communication is presented. Here, we considered two SNS approaches: 1) MWC and 2) FRI followed by spectrum reconstruction via OMP. The performance analysis for both the approaches is done considering the L-band scenario. The performance comparison of MWC and FRI shows that the FRI approach offers better probability of detection, higher throughput (at lower number of ADCs) and fewer number of sensing failures than MWC and requires lower number of ADCs due to non-contiguous sensing.

Chapter 7

Conclusions and Future Works

This chapter concludes the thesis work and presents some directions for future work in this research area.

7.1 Conclusions

This thesis studied the existing LDACS and modified it to support a new frame structure to enable tunable transmission bandwidth without compromising on backward architectural compatibility. We have designed the prototype of a reconfigurable and low complexity LDACS PHY based on filtered OFDM. The proposed LDACS PHY is augmented with computationally efficient wideband sensing to identify vacant spectrum opportunities in the 204 MHz L-band. We also explored Hardware-Software co-design to map the proposed LDACS PHY on heterogeneous Zynq SoC from Xilinx consisting of PS, i.e., ARM processor, PL, i.e., FPGA and RF front end, AD9361 from Analog Devices and analyzed the in-depth performance of LDACS PHY on the fixed-point hardware in the presence of RF impairments and wireless channels/interference. Various low complexity tunable digital filters are further explored to optimize the hardware complexity without compromising PHY performance.

The first work of the thesis presents the proposed LDACS PHY protocol that enables transceivers to dynamically adapt the transmission bandwidth over a wide range to meet the desired quality of service. High out-of-band attenuation leads to significant improvement in the vacant spectrum utilization. Simulation results show significant improvement over the BER and at least 32 dB lower interference to incumbent L-band users than existing LDACS in the various realistic channel conditions. The computational complexity of Ref-OFDM is lower than other waveforms except for OFDM, making the proposed work an attractive solution for the next-generation A2GC. In addition to mathematical and performance analysis using synthetic data, we demonstrated the functionality of the proposed Ref-OFDM PHY in a real radio environment on USRPs based testbed. The experimental results show that the proposed Ref-OFDM based LDACS provides nearly 35 dB less OOB emission and offers better BER/Throughput in different scenarios such as variable distance, variable altitude, LOS, NLOS, and variable DME antenna gain.

Next, we have done an in-depth performance analysis of the proposed LDACS PHY on fixed-point hardware in the presence of various RF impairments and wireless channels/interference by mapping the end-to-end LDACS PHY on Xilinx SoC ZC706 FPGA. The detailed experimental results are presented to analyze the area, power, PSD, and BER performance for OFDM, WOLA-OFDM, and FOFDM, having three-word lengths of 8/16/32 bit. The results show that the transceivers with the WL of 16 and 32 bit offer similar performance while the performance degrades for 8 bit WL. Though Ref-OFDM PHY offers superior BER and OOB emission (approximately 40 dB) performance with tunable bandwidth, it incurs significant penalties in resource utilization (27 % higher DSP48 based embedded multiplier) and power consumption compared to OFDM and Windowed-OFDM based LDACS. A novel LRef-OFDM based LDACS PHY is proposed. A similar performance analysis is performed on ZSoC hardware to reduce the hardware complexity further. The LRef-OFDM based LDACS offers identical OOB and BER performance to Ref-OFDM with 14.14 % less power and fewer resources (12.78 % DSP48). The performance-complexity trade-off of the proposed LDACS is shown in Figure 7.1.

The LDACS PHY is further augmented with the SNS-based compressive

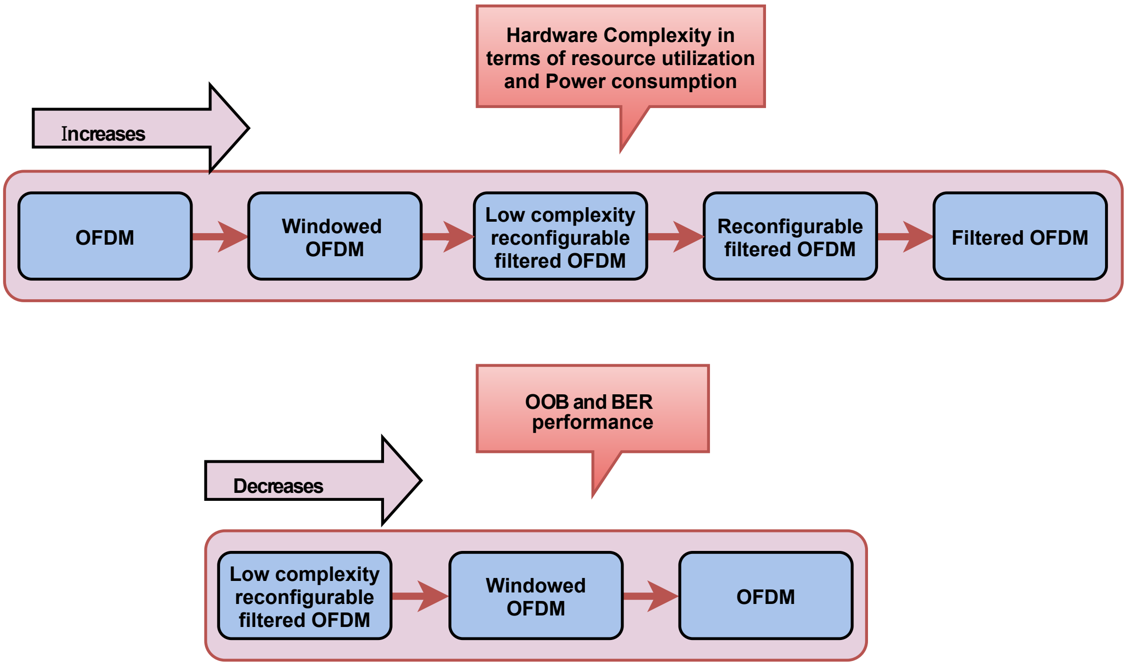

Figure 7.1: The performance-complexity comparison of different LDACS PHY.

sensing to efficiently utilize the non-contiguous L-band spectrum. The performance analysis is done to compare the MWC, and FRI approaches considering the L-band scenario. The performance comparison of MWC and FRI shows that the FRI approach offers a better recovery rate, higher throughput (at a lower number of ADCs), and fewer number of sensing failures than MWC and requires a lower number of ADCs due to non-contiguous sensing.

An in-depth performance analysis, feasibility on SoC, and backward compatibility with existing LDACS makes the proposed LRef-OFDM LDACS PHY, an attractive alternative for next-generation air to ground communication system.

7.1.1 Future Work

In this thesis, the LDACS PHY is redesigned to improve the vacant spectrum utilization. A spectrum efficient, reconfigurable, and low complexity LDACS PHY is developed and analyzed its performance in a real-radio environment and feasibility on a system-on-chip (SoC) platform. The proposed LDACS PHY and its architecture is suitable for single antenna air to ground communication systems. Some directions to pursue further research in this area have been identified and discussed below.

7.1.2 Orthogonal Time Frequency Space (OTFS) Based LDACS PHY

Current studies show that the A2G communication channel characterizes the channel model with large-scale fading, small-scale fading, shadowing, multipath, and Doppler effect [94]. These properties are determined by the environment and relative speed of aircraft. Changes in the environment make the channels time-variant. Recently, OTFS and windowed OTFS modulation is proposed in [95, 96], as an alternative to OFDM in high mobility time-variant scenarios. Several recent works on OTFS have emerged in the literature, determining the suitability of OTFS waveform for next-generation wireless systems. It converts the time-invariant channels into the time-independent channels in the delay-doppler domain. The OTFS modulator multiplexes each information symbol over 2D orthogonal basis functions (IFFT along with Doppler and FFT along with delay), spanning the entire time-frequency domain required to transmit a frame contrary to OFDM, where the basis waveform is highly localized. Therefore, OTFS performs well, specially in the high doppler spreads channel situation. The concept of the OTFS is shown in Figure 7.2.

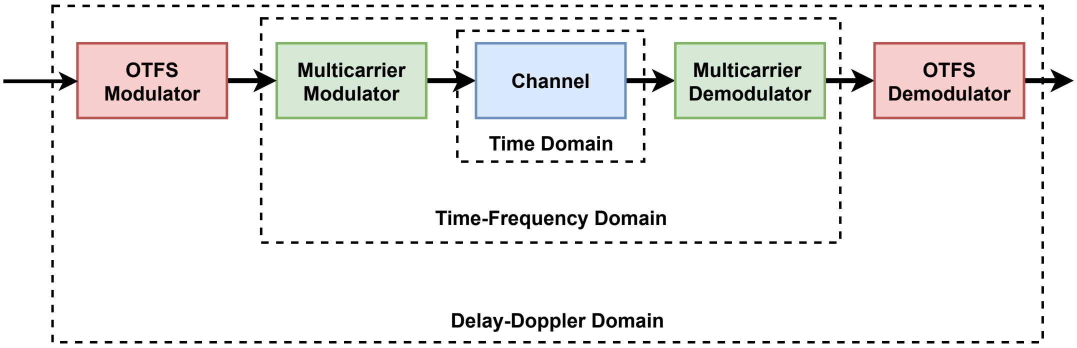

Figure 7.2: The concept of OTFS modulation and demodulation [96].

OTFS exhibits significantly lower block error rates compared to OFDM over a wide range of Doppler shifts (for vehicle speeds ranging from 30 km/h to 500 km/h in 4 GHz band). The robustness to high-Doppler channels (500 km/h vehicle speeds) is especially notable, as OFDM performance breaks down in such high-Doppler scenarios [95]. This shows that the OTFS based LDACS

PHY for next-generation A2GC can be explored in the future.

7.1.3 LDACS PHY A2A Mode

The A2A component of the FCI is currently in the initial stages of its development [97, 98]. The LDACS works in A2A mode and the A2G mode. There are some challenges to the design of the LDACS A2A mode. First, the scarcity of free spectrum in the L-band significantly limits the use of the available spectrum. Second, the LDACS A2A mode must operate without any ground or satellite support which imposes a great challenge for the design of the physical and data link (medium-access control [97]). The LDACS A2A will also operate in 960-1164 MHz aeronautical frequency band similar to A2G communication. To communicate with the other aircraft, the LDACS A2A will require at least one frequency channel. However, the 960-1164 MHz frequency band is already occupied with the other legacy users such as DME, TACAN, JTIDS, etc., as shown in Figure 1.3. These systems engage the frequency spectrum with a 1 MHz spectral gap. According to the studies, LDACS A2A will most likely share the spectrum with DME and TACAN and have similar frequency planning as A2G communication [98]. The low complexity reconfigurable filter for LDACS A2G proposed in this thesis can be modified according to the LDACS PHY A2A mode. Similar in-depth performance analysis of the candidate waveforms for LDACS A2A can be performed in the future.

7.1.4 MIMO Enhancement for LDACS PHY

An LRef-OFDM based LDACS PHY is proposed in this thesis for the broadband air to ground aeronautical communication system, which has some significant advantages over the existing OFDM-based LDACS. To further increase the transmission rate, reliability and system capacity of the A2G link, the adaptive Multiple-Input and Multiple-Output (MIMO) system is a sore subject for the researchers. A virtual MIMO A2G link is proposed in [99], in which the aircraft can be assigned multiple frequency points and achieves diversity gain in transmission. Different diversity and multiple antenna techniques for L-DACS1 and FBMC A2G communication systems for MIMO are investigated in the [14]. A multi-user MIMO scenario ([100]) for air to ground communication is shown in Figure 7.3.

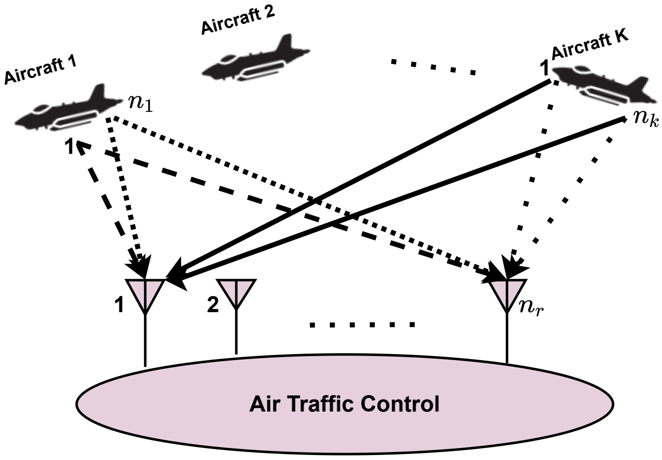

Figure 7.3: A MIMO communication scenario for A2GC. ATC has n_r antennas whereas each of K airplanes has n_k antennas [100].

The FBMC based LDACS has subcarrier filtering, which leads to very high system complexity. Due to the low complexity of LRef-OFDM LDACS can be easily extended to a multi-user multi-antenna system, unlike FBMC based LDACS. For this extension, we will explore several diversity and multiple antenna techniques for LDACS and LRef A2GC systems to increase the transmission rate and system capacity. The results can be simulated to show the advantages of using multiple antenna techniques. The work will realize the performance comparison of LDACS and LRef-OFDM based LDACS for MIMO system with the single antenna system. For the simulation we are going to use the air to ground channel models developed from NASA Glenn Research Center AG channel measurements.

7.1.5 LDACS PHY Architecture Implementation on RFSoC Hardware

In this thesis, the LDACS PHY is deployed on the fixed-point hardware Xilinx Zynq SoC integrated with the AD9361 RF front end. The performance analysis is done in the presence of various RF impairments and wireless channels/interference. The AD9361 is an analog front end that uses the IF approach and generates RF impairments such as passband ripple, group delay variation, matching, LO leakage issues etc.. The Xilinx zynq ultrascale+ RFSoC hardware is a solution to address this issue. It allows the analog/RF signal processing to be moved into the digital domain that enormously reduces or eliminates the RF impairments increases the flexibility to support wider bandwidths and multiple operating RF bands. In RFSoC, the analog processing block is replaced by an integrated direct-RF system, as shown in Figure 7.4.

This reduces the associated cost and increases adaptability and programmability. For implementing the LDACS PHY on RFSoC, the architectures need to be redesigned using the RFSoC blocks. Similar in-depth experimental analysis can be done for different candidate waveforms for LDACS A2GC in future.

7.1.6 Learning Based L-band Spectrum Sensing

Two SNS-based approaches to identify the spectrum holes of the LDACS spectrum are discussed in this thesis. Future generation aeronautical systems are expected much advanced spectrum management, including the detection of spectrum holes, spectrum sharing, spectrum mobility, and decision to select the most suitable transmission channel, etc.. The machine learning-based sensing algorithm for spectrum management is a potential candidate for research these days.

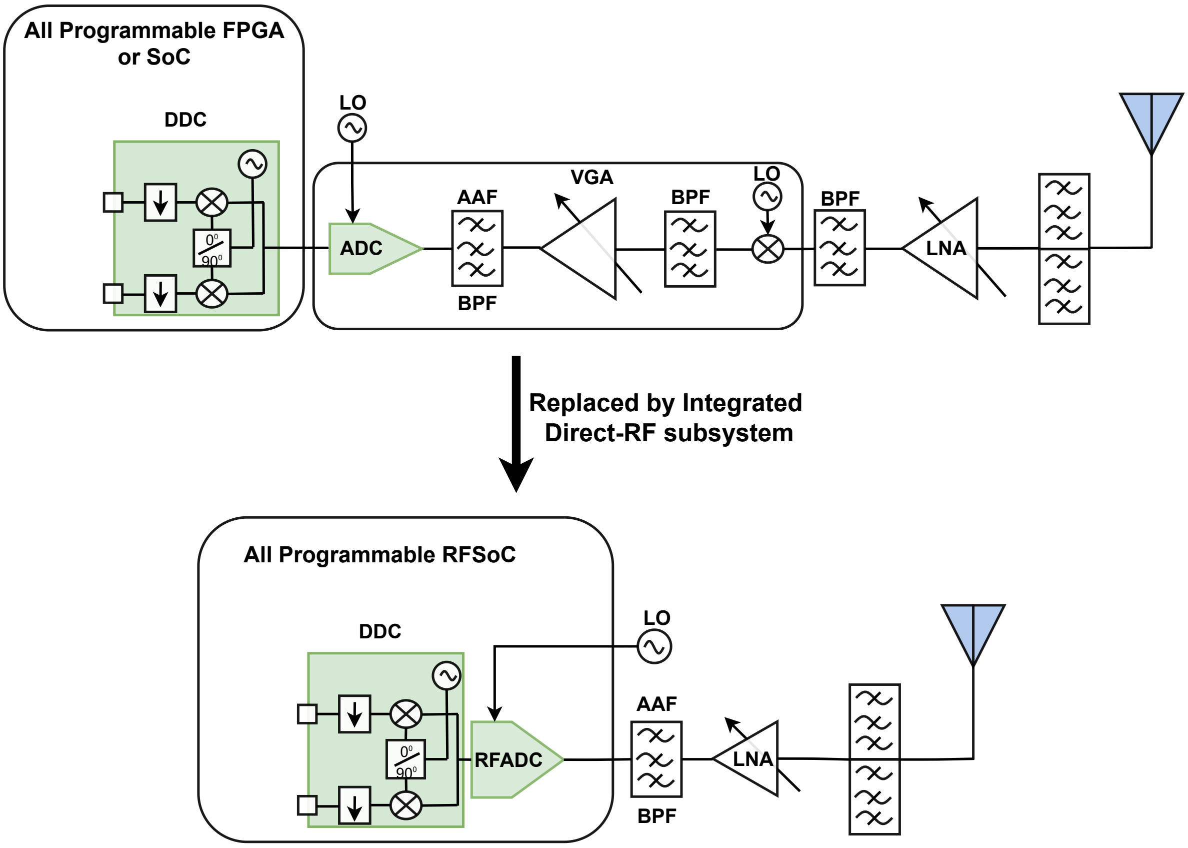

Figure 7.4: Comparison of RFSoC with other FPGA or SoC.

The ability to depict the data patterns of machine learning algorithms is gaining interest in spectrum sensing. Some machine learning-based works [101, 102] are used for compressive wideband sensing. A machine learning-based fusion center algorithm is proposed in [101]. The algorithm is based on training a machine learning classifier over a data set consisting of frame energy test statistics along with their corresponding decisions about the presence or absence of the primary user (PU) transmission. Different learning techniques enable the proper decision-making and channel switching, which increases the system's throughput and utilizes the resources effectively. Learning-based sensing techniques use complex techniques in an easy way but require massive data set for the training. The real-time performance is limited and highly depends on the feature selection for making any decision. A low-dimensional probability vector is proposed as the feature vector for machine learning-based classification in [102]. This probability feature vector provides a smaller training duration and a shorter classification time for testing vectors. The spectrum sensing performance highly depends on the primary user's interference. In another direction, a deep analysis on the interference in the aeronautical system can be performed in the future to ensure flight safety.

References

[1] T. Gräupl, N. Schneckenburger, T. Jost, M. Schnell, A. Filip, M. A. Bellido-Manganell, D. M. Mielke, N. Mäurer, R. Kumar, O. Osechas, and G. Battista, "L-band Digital Aeronautical Communications System (LDACS) flight trials in the national German project MICONAV," in *2018 Integrated Communications, Navigation, Surveillance Conference (ICNS)*, 2018, pp. 4A2–1–4A2–7.

[2] C. Rihacek, M. Sajatovic, J. Meser, and T. Gräupl, "L-band Digital Aeronautical Communications System (LDACS) - Technical Validations in SESAR2020," in *2019 IEEE/AIAA 38th Digital Avionics Systems Conference (DASC)*, 2019, pp. 1–6.

[3] M. Schnell, U. Epple, D. Shutin, and N. Schneckenburger, "LDACS: Future Aeronautical Communications for Air-Traffic Management," *IEEE Communications Magazine*, vol. 52, no. 5, pp. 104–110, 2014.

[4] M. Standar, "The State of Harmonisation and Key Priorities," in *2015 Integrated Communication, Navigation and Surveillance Conference (ICNS)*. IEEE, 2015, pp. 1–6.

[5] U. Epple and M. Schnell, “Overview of Legacy Systems in L-band and its Influence on the Future Aeronautical Communication System LDACS1 ,” *IEEE Aerospace and Electronic Systems Magazine*, vol. 29, no. 2, pp. 31–37, 2014.

[6] M. Mostafa, M. A. Bellido-Manganell, and T. Gräupl, “Feasibility of Cell Planning for the L-Band Digital Aeronautical Communications System Under the Constraint of Secondary Spectrum Usage,” *IEEE Transactions on Vehicular Technology*, vol. 67, no. 10, pp. 9721–9733, 2018.

[7] T. Graupl, M. Ehammer, and C.-H. Rokitansky, “L-DACS1 Data Link Layer Design and Performance,” in *2009 Integrated Communications, Navigation and Surveillance Conference*. IEEE, 2009, pp. 1–12.

[8] M. Schnell, S. Brandes, S. Gligorevic, C. . Rokitansky, M. Ehammer, T. Graupl, C. Rihacek, and M. Sajatovic, “B-AMC — Broadband Aeronautical Multi-Carrier Communications,” in *2008 Integrated Communications, Navigation and Surveillance Conference*, 2008, pp. 1–12.

[9] C.-H. Rokitansky, M. Ehammer, T. Grdupl, M. Schnell, S. Brandes, S. Gligorevic, C. Rihacek, and M. Sajatovic, “B-AMC A System for Future Broadband Aeronautical Multi-Carrier Communications in the L-Band,” in *2007 IEEE/AIAA 26th Digital Avionics Systems Conference*. IEEE, 2007, pp. 4–D.

[10] M. Sajatovic, B. Haindl, M. Ehammer, T. Gräupl, M. Schnell, U. Epple, and S. Brandes, “L-DACS1 System Definition Proposal: Deliverable D2,”

Eurocontrol Study Report, 2009.

[11] Y. Liu, X. Chen, Z. Zhong, B. Ai, D. Miao, Z. Zhao, J. Sun, Y. Teng, and H. Guan, "Waveform Design for 5G Networks: Analysis and Comparison," *IEEE Access*, vol. 5, pp. 19 282–19 292, 2017.

[12] H. Jamal and D. W. Matolak, "FBMC and L-DACS Performance for Future Air-to-Ground Communication Systems," *IEEE Transactions on Vehicular Technology*, vol. 66, no. 6, pp. 5043–5055, 2016.

[13] C. Zhang, J. Xiao, and Y. Zhang, "Massive MIMO Air-to-Ground communications," in *2014 IEEE/AIAA 33rd Digital Avionics Systems Conference (DASC)*, 2014, pp. 3C4–1–3C4–9.

[14] H. Jamal and D. W. Matolak, "Multicarrier Air to Ground MIMO Communication System Performance," in *2016 IEEE 84th Vehicular Technology Conference (VTC-Fall)*, 2016, pp. 1–5.

[15] S. Gligorevic, U. Epple, and M. Schnell, "The LDACS1 Physical Layer Design," in *Future Aeronautical Communications*. IntechOpen, 2011.

[16] S. Brandes, U. Epple, S. Gligorevic, M. Schnell, B. Haindl, and M. Sajatovic, "Physical Layer Specification of the L-Band Digital Aeronautical Communications System (L-DACS1)," in *2009 Integrated Communications, Navigation and Surveillance Conference*, 2009, pp. 1–12.

[17] U. Epple, F. Hoffmann, and M. Schnell, "Modeling DME Interference Impact on LDACS1," in *2012 Integrated Communications, Navigation and Surveillance Conference*, 2012, pp. G7–1–G7–13.

[18] N. Schneckenburger, N. Franzen, S. Gligorevic, and M. Schnell, in *2011 IEEE/AIAA 30th Digital Avionics Systems Conference, title=L-band Compatibility of LDACS1*, 2011, pp. 4C3–1–4C3–11.

[19] D. Gómez Depoorter and W. Kellerer, “Designing the Air–Ground Data Links for Future Air Traffic Control Communications,” *IEEE Transactions on Aerospace and Electronic Systems*, vol. 55, no. 1, pp. 135–146, 2019.

[20] U. Epple and M. Schnell, “Overview of Interference Situation and Mitigation Techniques for LDACS1,” in *2011 IEEE/AIAA 30th Digital Avionics Systems Conference*, 2011, pp. 4C5–1–4C5–12.

[21] S. Brandes, U. Epple, and M. Schnell, “Compensation of the impact of interference mitigation by pulse blanking in ofdm systems,” in *GLOBECOM 2009 - 2009 IEEE Global Telecommunications Conference*, 2009, pp. 1–6.

[22] E. Kim, “Improving DME Performance for APNT Using Alternative Pulse and Multipath Mitigation,” *IEEE Transactions on Aerospace and Electronic Systems*, vol. 53, no. 2, pp. 877–887, 2017.

[23] M. Schnell, N. Franzen, and S. Gligorevic, “L-DACS1 Laboratory Demonstrator Development and Compatibility Measurement Setup,” in *29th Digital Avionics Systems Conference*, 2010, pp. 3.E.3–1–3.E.3–11.

[24] N. Franzen, A. Arkhipov, and M. Schnell, “L-DACS1 Physical Layer Laboratory Demonstrator,” in *2010 Integrated Communications, Navigation, and Surveillance Conference Proceedings*, 2010, pp. A2–1–A2–11.

[25] A. Ambede, A. P. Vinod, and A. S. Madhukumar, “Design of a Low Complexity Channel Filter Satisfying LDACS1 Spectral Mask Specifications for Air-to-Ground Communication,” in *2016 Integrated Communications Navigation and Surveillance (ICNS)*, 2016, pp. 7E3–1–7E3–7.

[26] S. Dhabu, A. P. Vinod, and A. S. Madhukumar, “Low Complexity Fast Filter Bank Based Channelization in L-DACS1 for Aeronautical Communications,” in *2015 IEEE 13th International New Circuits and Systems Conference (NEWCAS)*, 2015, pp. 1–4.

[27] L. Ma and C. Zhang, “5G Wareforms Design for Aeronautical Communications,” in *2016 IEEE/AIAA 35th Digital Avionics Systems Conference (DASC)*, 2016, pp. 1–7.

[28] G. Fettweis, M. Krondorf, and S. Bittner, “GFDM - Generalized Frequency Division Multiplexing,” in *VTC Spring 2009 - IEEE 69th Vehicular Technology Conference*, 2009, pp. 1–4.

[29] R. Zayani, Y. Medjahdi, H. Shaiek, and D. Roviras, “WOLA-OFDM: A Potential Candidate for Asynchronous 5G,” in *2016 IEEE Globecom Workshops (GC Wkshps)*, 2016, pp. 1–5.

[30] V. Vakilian, T. Wild, F. Schaich, S. ten Brink, and J. Frigon, “Universal-Filtered Multi-Carrier Technique for Wireless Systems Beyond LTE,” in *2013 IEEE Globecom Workshops (GC Wkshps)*, 2013, pp. 223–228.

[31] H. Jamal, D. W. Matolak, and R. Sun, “Comparison of L-DACS and FBMC Performance in Over-Water Air-Ground Channels,” in *2015 IEEE/AIAA 34th Digital Avionics Systems Conference (DASC)*, 2015, pp. 2D6–1–2D6–9.

[32] J. Abdoli, M. Jia, and J. Ma, “Filtered OFDM: A New Waveform for Future Wireless Systems,” in *2015 IEEE 16th International Workshop on Signal Processing Advances in Wireless Communications (SPAWC)*, 2015, pp. 66–70.

[33] X. Cheng, Y. He, B. Ge, and C. He, “A Filtered OFDM Using FIR Filter Based on Window Function Method,” in *2016 IEEE 83rd Vehicular Technology Conference (VTC Spring)*, 2016, pp. 1–5.

[34] A. Farhang, M. Molavi Kakhki, and B. Farhang-Boroujeny, “Wavelet-OFDM versus Filtered-OFDM in Power Line Communication Systems,” in *2010 5th International Symposium on Telecommunications*, 2010, pp. 691–694.

[35] X. Zhang, M. Jia, L. Chen, J. Ma, and J. Qiu, “Filtered-OFDM - Enabler for Flexible Waveform in the 5th Generation Cellular Networks,” in *2015 IEEE Global Communications Conference (GLOBECOM)*, 2015, pp. 1–6.

[36] R. Gerzaguet, N. Bartzoudis, L. G. Baltar, V. Berg, J.-B. Doré, D. Kténas, O. Font-Bach, X. Mestre, M. Payaró, M. Färber *et al.*, "The 5G Candidate Waveform Race: A Comparison of Complexity and Performance," *EURASIP Journal on Wireless Communications and Networking*, vol. 2017, no. 1, pp. 1–14, 2017.

[37] E. Çatak and L. Durak-Ata, "Waveform Design Considerations for 5G Wireless Networks," *Towards 5G Wireless Networks-A Physical Layer Perspective*, pp. 27–48, 2016.

[38] W. Lu and T. Hinamoto, "A Unified Approach to the Design of Interpolated and Frequency-Response-Masking FIR Filters," in *2016 IEEE International Symposium on Circuits and Systems (ISCAS)*, 2016, pp. 2174–2177.

[39] C. W. Farrow, "A Continuously Variable Digital Delay Element," in *1988., IEEE International Symposium on Circuits and Systems*, 1988, pp. 2641–2645 vol.3.

[40] Jianghong Yu and Yong Lian, "Frequency-Response Masking Based Filters With the Even-Length Bandedge Shaping Filter," in *2004 IEEE International Symposium on Circuits and Systems (IEEE Cat. No.04CH37512)*, vol. 5, 2004, pp. V–V.

[41] W. Chen, M. Huang, and X. Lou, "Sparse FIR Filter Design Based on Interpolation Technique," in *2018 IEEE 23rd International Conference on Digital Signal Processing (DSP)*, 2018, pp. 1–5.

[42] T. Devis and M. Manuel, “A 17-Band Non-Uniform Interpolated FIR Filter Bank for Digital Hearing Aid,” in *2018 International Conference on Communication and Signal Processing (ICCSP)*, 2018, pp. 0452–0456.

[43] S. Roy and A. Chandra, “On the Order Minimization of Interpolated Bandpass Method Based Narrow Transition Band FIR Filter Design,” *IEEE Transactions on Circuits and Systems I: Regular Papers*, vol. 66, no. 11, pp. 4287–4295, 2019.

[44] N. Haridas and E. Elias, “Reconfigurable Farrow Structure-Based FRM Filters for Wireless Communication Systems,” *Circuits, Systems, and Signal Processing*, vol. 36, no. 1, pp. 315–338, 2017.

[45] R. Mahesh and A. P. Vinod, “Coefficient Decimation Approach for Realizing Reconfigurable Finite Impulse Response Filters,” in *2008 IEEE International Symposium on Circuits and Systems*, 2008, pp. 81–84.

[46] R. Mahesh and A. P. Vinod, “Low Complexity Flexible Filter Banks for Uniform and Non-Uniform Channelisation in Software Radios using Coefficient Decimation,” *IET Circuits, Devices & Systems*, vol. 5, no. 3, pp. 232–242, 2011.

[47] A. Ambede, K. G. Smitha, and A. P. Vinod, “A Modified Coefficient Decimation Method to Realize Low Complexity FIR Filters with Enhanced Frequency Response Flexibility and Passband Resolution,” in *2012 35th International Conference on Telecommunications and Signal Processing (TSP)*, 2012, pp. 658–661.

[48] A. Ambede, S. Shreejith, A. P. Vinod, and S. A. Fahmy, “Design and Realization of Variable Digital Filters for Software-Defined Radio Channelizers Using an Improved Coefficient Decimation Method,” *IEEE Transactions on Circuits and Systems II: Express Briefs*, vol. 63, no. 1, pp. 59–63, 2016.

[49] M. Raja, “Application of Cognitive Radio and Interference Cancellation in the L-Band Based on Future Air-to-Ground Communication systems,” *Digital Communications and Networks*, vol. 5, no. 2, pp. 111–120, 2019.

[50] S. Shreejith, L. K. Mathew, V. A. Prasad, and S. A. Fahmy, “Efficient Spectrum Sensing for Aeronautical LDACS Using Low-Power Correlators,” *IEEE Transactions on Very Large Scale Integration (VLSI) Systems*, vol. 26, no. 6, pp. 1183–1191, 2018.

[51] L. K. Mathew, “Low Complexity Spectrum Sensing for Cognitive Radio Enabled Aeronautical Communication Systems,” Ph.D. dissertation, Nanyang Technological University, 2020.

[52] J. A. Tropp, J. N. Laska, M. F. Duarte, J. K. Romberg, and R. G. Baraniuk, “Beyond Nyquist: Efficient Sampling of Sparse Bandlimited Signals,” *IEEE Transactions on Information Theory*, vol. 56, no. 1, pp. 520–544, 2010.

[53] M. Mishali and Y. C. Eldar, “Blind Multiband Signal Reconstruction: Compressed Sensing for Analog Signals,” *IEEE Transactions on Signal Processing*, vol. 57, no. 3, pp. 993–1009, 2009.

[54] ——, “From Theory to Practice: Sub-Nyquist Sampling of Sparse Wideband Analog Signals,” *IEEE Journal of Selected Topics in Signal Processing*, vol. 4, no. 2, pp. 375–391, 2010.

[55] K. Gedalyahu, R. Tur, and Y. C. Eldar, “Multichannel Sampling of Pulse Streams at the Rate of Innovation,” *IEEE Transactions on Signal Processing*, vol. 59, no. 4, pp. 1491–1504, 2011.

[56] D. L. Donoho, “Compressed Sensing,” *IEEE Transactions on Information Theory*, vol. 52, no. 4, pp. 1289–1306, 2006.

[57] E. J. Candes and T. Tao, “near-optimal signal recovery from random projections: Universal encoding strategies?” *IEEE Transactions on Information Theory*.

[58] Y. C. Pati, R. Rezaiifar, and P. S. Krishnaprasad, “Orthogonal Matching Pursuit: Recursive Function Approximation with Applications to Wavelet Decomposition,” in *Proceedings of 27th Asilomar Conference on Signals, Systems and Computers*, 1993, pp. 40–44 vol.1.

[59] S. K. Sahoo and A. Makur, “Signal Recovery from Random Measurements via Extended Orthogonal Matching Pursuit,” *IEEE Transactions on Signal Processing*, vol. 63, no. 10, pp. 2572–2581, 2015.

[60] M. Fornasier and H. Rauhut, “Iterative thresholding algorithms,” *Applied and Computational Harmonic Analysis*, vol. 25, no. 2, pp. 187–208, 2008.

[61] P. L. PL, “Zynq-7000 All Programmable SoC Overview,” 2012.

[62] T. H. Pham, V. A. Prasad, and A. S. Madhukumar, "A Hardware-Efficient Synchronization in L-DACS1 for Aeronautical Communications," *IEEE Transactions on Very Large Scale Integration (VLSI) Systems*, vol. 26, no. 5, pp. 924–932, 2018.

[63] T. H. Pham, A. Vinod, and A. Madhukumar, "An Efficient Data-Aided Synchronization in L-DACS1 for Aeronautical Communications," in *Proceedings of the 2017 International Conference on Data Mining, Communications and Information Technology*, 2017, pp. 1–5.

[64] S. Shreejith, A. Ambede, A. P. Vinod, and S. A. Fahmy, "A Power and Time Efficient Radio Architecture for LDACS1 Air-to-Ground Communication," in *2016 IEEE/AIAA 35th Digital Avionics Systems Conference (DASC)*, 2016, pp. 1–6.

[65] M. Brogioli, "The DSP Hardware/Software Continuum," in *DSP for Embedded and Real-Time Systems*. Elsevier, 2012, pp. 103–111.

[66] K. Barr, *ASIC design in the silicon sandbox: a complete guide to building mixed-signal integrated circuits*. McGraw-Hill Education, 2007.

[67] B. Drozdenko, M. Zimmermann, T. Dao, K. Chowdhury, and M. Leeser, "Hardware-Software Co-Design of Wireless Transceivers on Zynq Heterogeneous Systems," *IEEE Transactions on Emerging Topics in Computing*, vol. 6, no. 4, pp. 566–578, 2018.

[68] R. Dobai and L. Sekanina, “Towards Evolvable Systems based on the Xilinx Zynq Platform,” in *2013 IEEE International Conference on Evolvable Systems (ICES)*, 2013, pp. 89–95.

[69] J. Pendlum, M. Leeser, and K. Chowdhury, “Reducing Processing Latency with a Heterogeneous FPGA-Processor Framework,” in *2014 IEEE 22nd Annual International Symposium on Field-Programmable Custom Computing Machines*, 2014, pp. 17–20.

[70] J. van de Belt, P. D. Sutton, and L. E. Doyle, “Accelerating Software Radio: Iris on the Zynq SoC,” in *2013 IFIP/IEEE 21st International Conference on Very Large Scale Integration (VLSI-SoC)*, 2013, pp. 294–295.

[71] R. Marlow, C. Dobson, and P. Athanas, “An Enhanced and Embedded GNU Radio Flow,” in *2014 24th International Conference on Field Programmable Logic and Applications (FPL)*, 2014, pp. 1–4.

[72] B. Özgül, J. Langer, J. Noguera, and K. Visses, “Software-Programmable Digital Pre-Distortion on the Zynq SoC,” in *2013 IFIP/IEEE 21st International Conference on Very Large Scale Integration (VLSI-SoC)*, 2013, pp. 288–289.

[73] S. Shreejith, L. K. Mathew, V. A. Prasad, and S. A. Fahmy, “Efficient Spectrum Sensing for Aeronautical LDACS Using Low-Power Correlators,” *IEEE Transactions on Very Large Scale Integration (VLSI) Systems*, vol. 26, no. 6, pp. 1183–1191, 2018.

[74] F. Eurocontrol, “Communications Operating Concept and Requirements for the Future Radio System,” *COCR V2. 0*, 2002.

[75] G. Stoyanov and M. Kawamata, “Variable Digital Filters,” *J. Signal Processing*, vol. 1, no. 4, pp. 275–289, 1997.

[76] T. Solla and O. Vainio, “Comparison of Programmable FIR Filter Architectures for Low Power,” in *Proceedings of the 28th European Solid-State Circuits Conference*. IEEE, 2002, pp. 759–762.

[77] A. Ambede, S. Shreejith, A. P. Vinod, and S. A. Fahmy, “Design and Realization of Variable Digital Filters for Software-Defined Radio Channelizers Using an Improved Coefficient Decimation Method,” *IEEE Transactions on Circuits and Systems II: Express Briefs*, vol. 63, no. 1, pp. 59–63, 2016.

[78] S. Garg and S. J. Darak, “FPGA Implementation of High Speed Reconfigurable Filter Bank for Multi-Standard Wireless Communication Receivers,” in *2016 20th International Symposium on VLSI Design and Test (VDAT)*, 2016, pp. 1–5.

[79] S. S. Haykin, *Digital communications*. Wiley New York, 1988.

[80] H. Abdulkarim, “Comparison of Proposals for the Future Aeronautical Communication System LDACS,” 2013.

[81] N. Agrawal and S. J. Darak, “Performance Analysis of Reconfigurable Filtered OFDM for LDACS,” in *2019 11th International Conference on Communication Systems Networks (COMSNETS)*, 2019, pp. 500–503.

[82] S. Garg and S. J. Darak, "Candidate waveforms for wireless communications: Analysis via Hardware Software Co-Design on Zynq SoC," Ph.D. dissertation, 2017.

[83] L. H. Crockett, R. Elliot, M. Enderwitz, and R. Stewart, *The Zynq Book: Embedded Processing with the Arm Cortex-A9 on the Xilinx Zynq-7000 All Programmable Soc*. Strathclyde Academic Media, 2014.

[84] N. Agrawal, S. Darak, and F. Bader, "Spectral Coexistence of LDACS and DME: Analysis via Hardware Software Co-Design in Presence of Real Channels and RF Impairments," *arXiv preprint arXiv:1910.04649*, 2019.

[85] S. J. Darak, A. P. Vinod, E. M. . Lai, J. Palicot, and H. Zhang, "Linear-Phase VDF Design With Unabridged Bandwidth Control Over the Nyquist Band," *IEEE Transactions on Circuits and Systems II: Express Briefs*, vol. 61, no. 6, pp. 428–432, 2014.

[86] S. J. Darak, A. P. Vinod, R. Mahesh, and E. M. Lai, "A Reconfigurable Filter Bank for Uniform and Non-Uniform Channelization in Multi-Standard Wireless Communication receivers," in *2010 17th International Conference on Telecommunications*, 2010, pp. 951–956.

[87] V. Marojevic, X. R. Balleste, and A. Gelonch, "A Computing Resource Management Framework for Software-Defined Radios," *IEEE Transactions on Computers*, vol. 57, no. 10, pp. 1399–1412, 2008.

[88] Y. Neuvo, Dong Cheng-Yu, and S. Mitra, “Interpolated Finite Impulse Response Filters,” *IEEE Transactions on Acoustics, Speech, and Signal Processing*, vol. 32, no. 3, pp. 563–570, 1984.

[89] N. Agrawal, A. Ambede, S. Vinod, and A. Madhukumar, “Paper with Appendix: Design and Implementation of Low Complexity Reconfigurable Filtered-OFDM based LDACS,” *arXiv preprint arXiv:2009.10109*, 2020.

[90] T. Gräupl, C. Rihacek, B. Haindl, and Q. Parrod, “LDACS A/G Specification,” *German Aerospace Center (DLR), Germany, SESAR2020 PJ14-02-01 D*, vol. 3, pp. 3–010, 2017.

[91] T. W. Parks and C. S. Burrus, *Digital filter Design*. Wiley-Interscience, 1987.

[92] A. Mehrnia and A. N. Willson, “On Optimal IFIR Filter Design,” in *2004 IEEE International Symposium on Circuits and Systems (IEEE Cat. No.04CH37512)*, vol. 3, 2004, pp. III–133.

[93] J. G. Proakis and D. G. Manolakis, “Digital signal processing,” *PHI Publication: New Delhi, India*, 2004.

[94] D. W. Matolak and R. Sun, “Air–Ground Channel Characterization for Unmanned Aircraft Systems—Part I: Methods, Measurements, and Models for Over-Water Settings,” *IEEE Transactions on Vehicular Technology*, vol. 66, no. 1, pp. 26–44, 2017.

[95] R. Hadani, S. Rakib, M. Tsatsanis, A. Monk, A. J. Goldsmith, A. F. Molisch, and R. Calderbank, “Orthogonal Time Frequency Space Modu-

lation," in *2017 IEEE Wireless Communications and Networking Conference (WCNC)*, 2017, pp. 1–6.

[96] Z. Wei, W. Yuan, S. Li, J. Yuan, and D. W. K. Ng, "Transmitter and Receiver Window Designs for Orthogonal Time-Frequency Space Modulation," *IEEE Transactions on Communications*, vol. 69, no. 4, pp. 2207–2223, 2021.

[97] M. A. Bellido-Manganell and M. Schnell, "Towards Modern Air-to-Air Communications: The LDACS A2A Mode," in *2019 IEEE/AIAA 38th Digital Avionics Systems Conference (DASC)*. IEEE, 2019, pp. 1–10.

[98] ——, "Feasibility of the Frequency Planning for LDACS Air-to-Air Communications in the L-Band," in *2021 Integrated Communications Navigation and Surveillance Conference (ICNS)*. IEEE, 2021, pp. 1–14.

[99] C. Zhang, J. Xiao, and K. Pang, "Aeronautical virtual MIMO Communications with Terrestrial Linear Array Antenna," in *Proceedings 2013 International Conference on Mechatronic Sciences, Electric Engineering and Computer (MEC)*. IEEE, 2013, pp. 3089–3093.

[100] J. Rasool, G. E. Oien, J. E. Hakegard, and T. A. Myrvoll, "On Multiuser MIMO Capacity Benefits in Air-to-Ground Communication for Air Traffic Management," in *2009 6th International Symposium on Wireless Communication Systems*. IEEE, 2009, pp. 458–462.

[101] A. M. Mikaeil, B. Guo, and Z. Wang, "Machine Learning to Data Fusion Approach for Cooperative Spectrum Sensing," in *2014 International Con-*

ference on Cyber-Enabled Distributed Computing and Knowledge Discovery. IEEE, 2014, pp. 429–434.

[102] Y. Lu, P. Zhu, D. Wang, and M. Fattouche, “Machine Learning Techniques with Probability Vector for Cooperative Spectrum Sensing in Cognitive Radio Networks,” in *2016 IEEE wireless communications and networking conference*. IEEE, 2016, pp. 1–6.